BOSTON UNIVERSITY

GRADUATE SCHOOL OF ARTS AND SCIENCES

Dissertation

STUDIES OF TWO-DIMENSIONAL MATERIALS BEYOND GRAPHENE: FROM FIRST-PRINCIPLES TO MACHINE LEARNING APPROACHES

by

PAUL ZAKHARIA FAJAR HANAKATA

B.A, Wesleyan University, 2014

Submitted in partial fulfillment of the

requirements for the degree of

Doctor of Philosophy

2019

Approved by

First Reader

David Campbell, Ph.D.
Professor of Physics
Professor of Electrical and Computer Engineering
Professor of Materials Science and Engineering

Second Reader

Harold Park, Ph.D.
Professor of Mechanical Engineering

Acknowledgments

First and foremost, I wish to express my deepest gratitude to my advisor, Professor David Campbell, for his continual guidance, trust, and inspiration. I feel very fortunate to have had the freedom to explore many areas of physics, from hard and soft condensed matter to machine learning. David has always believed in and encouraged me. I cannot thank him enough for the amount of time he has invested in me in the past five years. Without his mentorship and encouragement, I would not have been able to continue my academic journey. It has truly been a pleasure and an honor to work with him.

Many thanks to Professor Harold Park. I am fortunate to work with him on various projects, which has helped me better understand the scope of the current research. His hard work and willingness to learn new topics beyond his expertise has been a source of encouragement for me to continue working on new and challenging problems. I appreciate his honesty and willingness to share his career advice, and I value his great mentorship throughout my PhD career.

I would like to thank to my collaborators at the National University of Singapore (NUS). Many thanks to Professor Castro Neto, who worked with me on the fundamental studies of 2D materials. His enthusiasm in physics and its application has been an inspiration for me to think 'bigger.' His course on 2D materials beyond graphene inspired me. I am indebted to Dr. Alexandra Carvalho, who taught me density functional theory, and to Dr. Aleksandr Rodin, who taught me tight-

binding. Collaborating with them has made my research career more fruitful. I have always enjoyed our midnight Skype sessions and our discussions on our exciting projects. Thank you so much for your hospitality during my visits at NUS and for your friendships.

I am indebted to Dr. Ekin Dogus Cubuk at Google. Despite of our relatively short encounter, Dogus has been a great collaborator, and most importantly, an amazing friend. His creative ideas in combining machine learning and physics to solve physics problems have inspired me to pursue research in machine learning. Much of his help has led me to a number of exciting opportunities. I am grateful for his advice and help when I applied for postdocs and the Google AI residency program. I would also like to thank Professor Pankaj Mehta, Dr. Edbert Sie, and Dr. Marin Bukov, who helped with my postdoc applications and interviews.

I wish my gratitude to my committee members. I would like to thank Professor So-Young Pi. She has been a great instructor who taught me how to solve physics problems correctly. Her lecture notes have been very helpful whenever I needed to review fundamental concepts. I want to thank Professor Anna Swan, who included me in a collaborative work on strained graphene. Our work has inspired me to develop a strain-induced gauge field theory in lead chalcogenides. I am also grateful to Professor Douglas Holmes for including me in the kirigami actuators project, which motivated me to develop a machine learning approach for topology optimization.

I would like to thank my best friend and labmate at Boston University–Mohit Pandey. He is a great speaker and, surprisingly, also a great listener. His extroverted personality has made me a more outspoken scientist. I am thankful for our seemingly random discussions that led to many new research ideas. I have always admired his hard work, quickness in learning about a new field, openness, honesty, care for his

friends, and great sense of humor. Thank you for making my PhD journey full of laughter. I would also like to thank Dr. Zenan Qi who worked with me in my first year of PhD. I am also grateful to all my friends at the BU physics department for their continual support and encouragement.

I am grateful to the physics department at BU, especially for the invaluable lessons I have learned from the faculties and for the support I have received from staff. I would like to thank Mirtha Cabello, who has offered much help since my first day. I am grateful for the financial support I have received throughout my PhD career. I would like to thank the Hariri Incubation grant and the Hariri Graduate fellowship, which supported me in my final year.

I cannot thank my family enough for their encouragement and prayers for my pursuit in scientific work. Many thanks to my wife Angela for her love and support. She has sacrificed so much for me as I pursue my PhD. To my friends, thank you for sharing my ups and downs in these years. Above all, praise and honor to my Heavenly Father, who has provided me a wonderful community and a world full of mysteries to explore.

STUDIES OF TWO-DIMENSIONAL MATERIALS BEYOND GRAPHENE: FROM FIRST-PRINCIPLES TO MACHINE LEARNING APPROACHES

PAUL ZAKHARIA FAJAR HANAKATA

Boston University, Graduate School of Arts and Sciences, 2019

Major Professor: David Campbell, Ph.D., Professor of Physics

ABSTRACT

Monolayers and heterostructures of two-dimensional (2D) electronic materials with spin-orbit interactions offer the promise of observing many novel physical effects. While theoretical predictions of 2D layered materials based on density functional theory (DFT) are many, the DFT approach is limited to small simulation sizes (several nanometers), and thus inhomogeneous strain and boundary effects that are often observed experimentally cannot be simulated within a reasonable time. The aim of this thesis is (i) to study effects of strain on 2D materials beyond graphene using first-principles and tight-binding methods and (ii) to investigate the effects of cuts–"kirigami"– on 2D materials using molecular dynamics and machine learning approach.

The first half of this thesis focuses on the effects of strain on manipulating spin and valley degrees of freedom for two classes of 2D materials–monochalcogenide and lead chalcogenide monolayers–using DFT. A tight-binding (TB) approach is developed to describe the electronic changes in lead chalcogenide monolayers due to strains that often persist in real devices. The strain-dependent TB model allows one to establish a relationship between the Rashba field and the out-of-plane strain or

electric polarization from a microscopic view, a connection that is not well understood in the ferroelectric Rashba materials. This framework connecting strain fields and electronic changes is important to overcome the size and computational limitations associated with DFT.

The second part of the thesis focuses on defect engineering and design of 2D materials via the "kirigami" technique of introducing different patterns of cuts. A machine learning (ML) approach is presented to provide physical insights and an effective model to describe the physical system. We demonstrate that a machine learning model based on a convolutional neural network is able to find the optimal design from a training data set that is much smaller than the design space.

Contents

List of Figures

List of Abbreviations and Symbols

AC	armchair
CNN ..	convolutional neural network
DFT ..	density functional theory
DL	deep learning
FERSC	ferroelectric Rashba semiconductor
MD ...	molecular dynamics
ML	machine learning
NN	neural network
OLS ...	ordinary least squares
SOI ...	spin-orbit interaction
TMD ..	transitional metal dichalcogenides
ZZ	zigzag

Chapter 1

Introduction

1.1 Two-dimensional Age

1.1.1 A Brief History of 2D Materials

In 1959, Nobel Laureate physicist Richard Feynman in his famous lecture "There's Plenty of Room at the Bottom" envisioned a future where the entire Encyclopaedia Brittanica could be written on the head of a pin [5]. Current hard drives can store information at around 1 Terabit/inch^2 and since the size of Encyclopaedia Brittanica is around 4 Gigabytes, we have indeed reached what Feynman envisioned where thousands of Encyclopedias can be carried around on a portable hard drive the size of a library card. His proposals and ideas have inspired many generations of scientists and engineers, and progress is still being made in miniaturizing fast computers and information storage.

In 2004, Novosolev, Geim, and colleagues first demonstrated the isolation of a single atom thick sheet of carbon, known as graphene [6]. They successfully isolated graphene by mechanically exfoliating thin layers of graphite with scotch tape. Graphene is one atomic layer of carbons arranged in a hexagonal structure. It is a metal (zero-gap) and the most interesting aspect of graphene that generated significant attention from a diverse spectrum of scientists, from condensed matter to

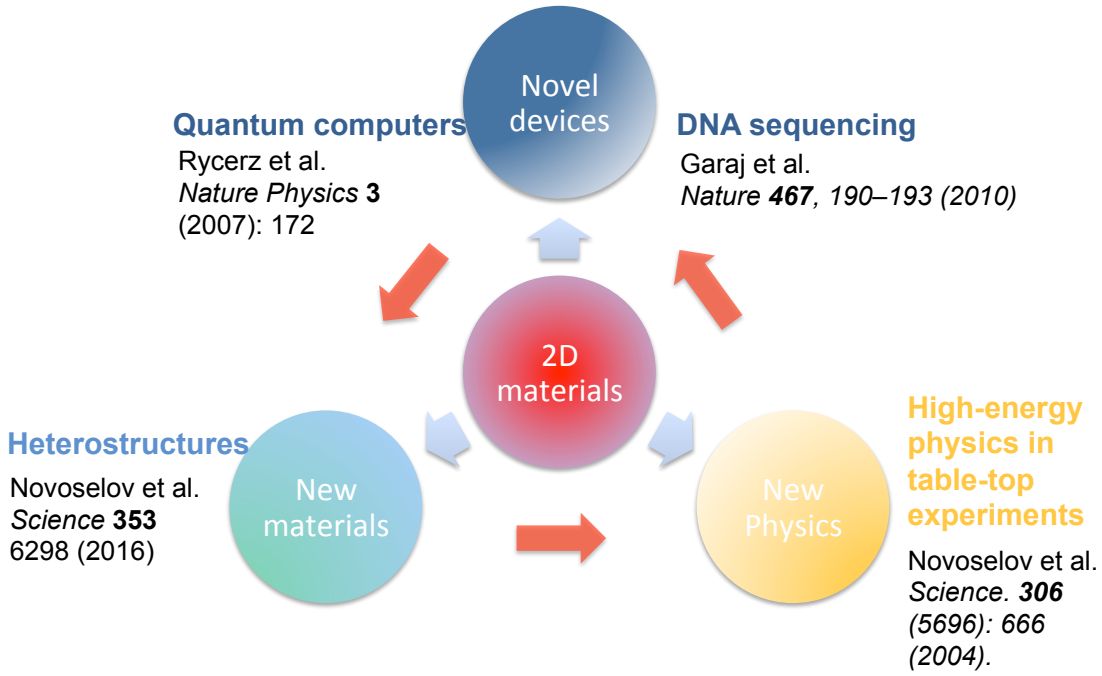

Figure 1.1: A schematic cycle of study of 2D materials: from fundamental studies, applications, to discoveries of new 2D materials.

high energy physicists, is its chiral Dirac fermions. The linear dispersion of electrons in graphene led to many ground breaking discoveries, such as the Quantum Hall Effect [7, 8], Klein tunneling [9], and strain-induced pseudomagnetic fields and non-integer Landau level spacing [10].

Soon after, several other 2D materials, such as transition metal dichalcogenides (TMDs), were successfully isolated using similar mechanical exfoliation techniques [11]. The behavior of these materials in monolayer (single layer) form is different from their 3D bulk counterparts. One of the most intriguing findings in TMD monolayers (such as MoS_2) was the selective valley polarization [12, 13] [1]. Similar to spin, the valley degree of freedom can be used to store information; this mechanism, known as valleytronics, has been proposed for developing valley-based devices. Other novel

[1] Monolayers or single layers of TMDs do not imply one atomic thin layer. Specifically, TMDs like MoS_2 have a transition metal atom sandwiched between two chalcogen atoms in one unit cell.

technological applications have also been demonstrated, ranging from applications of nanopores on 2D materials for DNA sequencing [14] to quantum computers [15]. The isolation of many layered materials was not only a scientific success to make more room at the bottom, it also opened the door for studying low-dimensional systems and many other phenomenon that are difficult to observe in 3D systems, and for developing novel nanoscale devices.

1.1.2 Heterostructures and Defects Engineering

The family of 2D crystals has expanded greatly thanks to recent advances in chemical vapor deposition (CVD) and exfoliation techniques [16, 17, 18]. In the bulk form, the layers in many of these 2D materials are often held together by van der Waals forces [19]. Another great opportunity is that these layered materials can be stacked in both vertical and lateral directions, illustrated in fig. 1.1. Many of these combined materials, known as heterostructures, are not found in nature.

Creating a material with new functionalities or new behaviors can be achieved without combining materials with distinct properties. Different stacking strategies, such as twisting or shifting (which often induce local strains), can be used to break symmetries. Symmetries and conservation laws are particularly important concepts to describe physical phenomena in many systems. For instance, controlling the number of layers or choosing a specific stacking configuration can be used to break the inversion symmetry of few layered materials. This strategy has been utilized to control spin and valley degree of freedom in few layered MoS_2 [20, 21]. And most recently it has been shown experimentally that unconventional superconductivity can be achieved in twisted bilayer graphene systems [22]. Heterostructures provide the opportunity to study new physics and to generate materials with a great variety of

properties and potential applications.

In addition to stacking, adding defects or removing atoms in 2D materials is an effective strategy to alter their mechanical, electronic, or optical properties due to their high surface area. This method is often achieved by patterning the materials with geometrical cuts (antidot lattices) [23, 24, 25] and defects [26]. Electronically, a graphene nanoribbon with zigzag edges is a *semiconductor* (non-zero gap) [27]. In mechanics, arrays of cuts, known as kirigami cuts, allow graphene to stretch more than double that of a pristine, uncut graphene sheet [28]. 2D platforms are indeed a fascinating "playground" for scientists to explore and there are many aspects of physics yet to be explored by expanding this 2D playground. The ability to reduce the thickness of materials to their physical limits and manipulating them at the quantum level with a high precision are among the most important recent scientific advancements.

1.2 Further discovery

In the 10 years since the discovery of graphene, most studies of 2D materials have focused on 2D materials with hexagonal structure, such as graphene and TMDs (MoS_2, $MoSe_2$, WS_2, etc.). Recently, monolayer black phosphorus (phosphorene) with orthorhombic structure and a moderate band gap (in between TMDCs and graphene) has gained significant attention [29]. Phosphorene belongs to the D_{2h}^{18} point group which has a lower symmetry compared to graphene, which has D_{6h}^{4} point group symmetry. Due to the orthorhombic structure and reduced symmetry, phosphorene has highly anisotropic excitonic [30] and mechanical properties [31].

Synthesizing materials is often costly and finding new materials often requires significant trial and error. Simulations via first-principles methods based on density

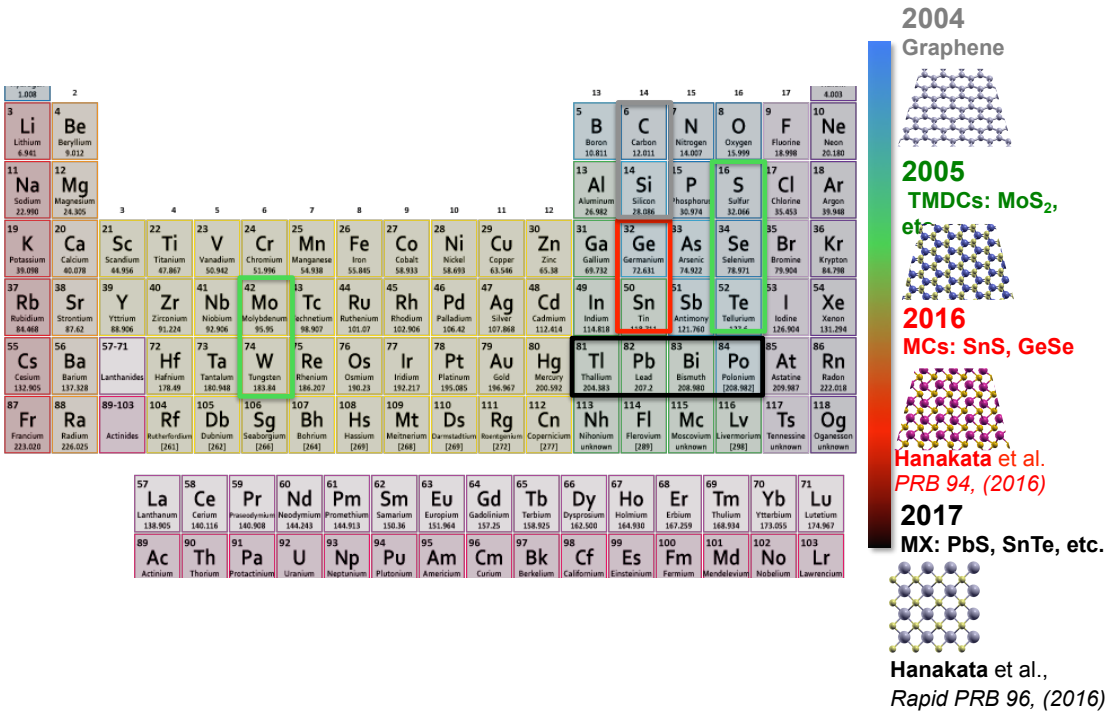

Figure 1.2: The emergence of new classes of 2D materials.

functional theory (DFT) have become very popular for predicting stable phases, band structures, and other important properties. This *ab initio* approach is powerful for discovering new 2D materials because it does not rely on the available experimental data of the proposed materials. First-principles calculations were used to discover several new classes of 2D materials beyond graphene, including monochalcogenide monolayers (SnS, GeSe, etc.) with tunable ferroelectric and valleytronic properties [32]. The monochalcogenide monolayer has a puckered structure similar to phosphorene, but with two types of atoms.

Most studies of 2D materials have focused on materials with relatively *weak* spin-orbit interactions (SOI). SOI interactions add an additional degree of freedom which often brings a much richer physics. It has been proposed that combining topological insulators or semiconductors with Rashba interactions coupled with superconductors

may host Majorana fermions, which are the building blocks for topological quantum computers [33, 34]. This motivated some of the work in this thesis, including studying other possible 2D materials consisting of heavy elements. Doing so led to the addition of a new class of 2D buckled ferroelectric Rashba semiconductors (FERSC) to the family of 2D materials [35, 36]. Figure 1.2 shows the ongoing expansions of discovered 2D layered materials. Figure 1.2 does not include all discovered materials to date, such as phosphorene [29], buckled monolayers with one type of atom (Xene) [37] and very recently discovered 2D magnetic materials (e.g CrI_3) [38].

1.3 Multiscale Approach and Limitations

While DFT is widely used to study the electronic properties of 2D materials, it is computationally expensive thus not practical to study large systems. Within the DFT approach, a time-independent Schrödinger equation of non-interacting many single electrons are solved iteratively [39, 40, 41]. Solving this so-called Kohn-Sham equation requires diagonalizing a matrix of the size of the number of *electrons*. The computational time to find the electronic ground state is roughly $\mathcal{O}(N_e^3)$ where N_e is the number of electrons. In DFT, finding the electronic ground states is a necessary step before calculating the forces acting on nuclei, which are then used for finding the relaxed structure. This makes DFT very expensive once the simulated super-cells reach the size of a nanometer or larger (hundreds of atoms). This limits DFT simulations to inhomogeneous strains over a small region only.

Classical molecular dynamics (MD) is another approach to find equilibrium configurations of a material or to simulate a material under external forces [42]. MD solves newtonian equations of many atoms. Considering all interactions between atoms, the time complexity of MD scales roughly as $\mathcal{O}(N_a^2)$, where N_a is number

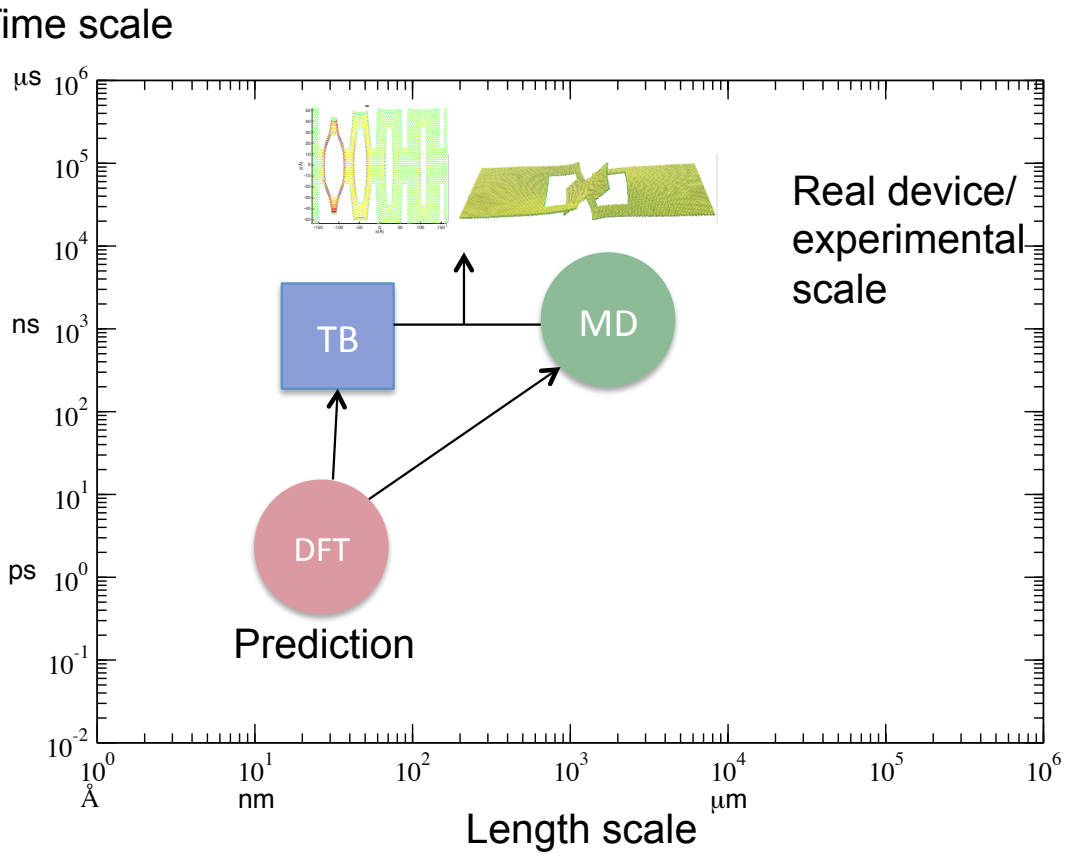

Figure 1.3: Multiscale approaches. The DFT approach is well-suited for calculating properties that depend on quantum mechanical quantities, but cannot account for many atoms. MD can simulate a much larger system, but TB has to be included for calculating the electronic properties.

of *atoms* not electrons [42, 43].This gives MD a huge computational advantage over DFT methods for studying structure. However, unlike DFT, MD relies on "effective" potentials which often are not available for many 2D materials. The effective potentials are usually obtained by fitting the empirical potentials to fundamental properties like phonon dispersion or elastic constants. Because MD is classical, and thus does not explicitly account for electronic degrees of freedom, it cannot be used to calculate electronic properties. In order to calculate electronic properties based on atomic configurations, tight-binding (TB) approaches are often used.

A TB model requires much less computing resources compared to DFT as TB considers only a few bands (usually around the Fermi level) and it does not need to perform self-consistent calculations to find the electronic ground state. TB describes the electronic states of a solid by approximating the total wavefunction as a superposition of localized orbitals centered at the atomic sites [39, 40]. TB models are usually described by Slater-Koster determinant which requires the atomic positions and the hopping parameters (neighbor interactions). Hopping parameters are usually obtained by fitting the band structure of a TB model to the DFT result. Since MD gives atomic configurations, TB can be used to subsequently calculate electronic properties. The length and time scales of DFT and MD methods are summarized in fig. 1.3. The above-discussed limitations of MD and DFT motivated the development of a TB model for lead chalcogenides monolayers, in addition to a continuum model to describe electronic changes within a strain-dependent TB framework.

Another computational challenge arises in attempting to use MD to design nanodevices, or to find an optimal design for a material or structure that satisfies specific performance metrics. Specifically, such a computational design process would require many (likely millions) of MD simulations, which is impractical. For instance, suppose a design problem was to optimally place vacancies (holes) on a 2D material to achieve a specific physical property. If a 2D membrane were partitioned into $N_{\text{grid}} = N_x \times N_y$ grids, there are $2^{N_{\text{grid}}}$ ways to locate the holes. This means the exploration space grows *exponentially* with system size, and clearly brute-force calculations would not be practical with the current computing power. Recently, machine learning (ML) has become a popular tool to describe physical systems [44, 45, 46]. The core idea of ML is to build flexible and expressive models without knowing the physical models, relying from the data (patterns) instead. Several databases, such as Materials

Project [47], Citrine Informatics, and many others [48], have been built as a platform to store, organize, and analyze a vast amount of experimental and DFT data (hundred thousands of compounds) for training ML models. However, to date, most ML approaches have been used for predicting properties of 2D materials with different atomic compositions and/or crystal symmetries [49, 50, 51], but very few for predicting properties or to do inverse design based on *structural* and *geometrical* defects. The last part of the thesis introduces ML approaches to approximate some unknown target functions and use them as a search algorithm.

Using ML for inverse design is particularly valuable for research and industrial purposes as the ML is able pre-screen the best performing designs in simulations with very minimal development costs (few training data), and to use such information to fabricate the materials. The ML method is universal and parameter-free, in a sense that it can be used to design any material without any prior physical knowledge of the system. As the ML method only needs data, it can be applied to experimental work where the physical model is not known and cannot be simulated by MD or other simulation methods.

1.4 Contributions of This Thesis

The main findings reported in this thesis are as follows. First, discoveries of new 2D materials beyond graphene based on DFT. This includes orthorhombic monochalcogenides and non-centrosymmetric ferroelectric monolayers with strong orbit interactions. Next, the development of TB models and continuum approaches to model and study electronic changes in monolayers in the presence of strains are shown. Finally, it is shown how defects (e.g holes or cuts) can be used to modify properties of 2D materials, and furthermore how ML approaches can be used to design 2D materials

to achieve a specific target property. In more detail:

- Chapter 3 presents first-principles studies of newly discovered 2D materials. The simulation results are based on DFT. Structural phases of tin sulfide (SnS) and germanium selenide (GeSe) were studied, and it is demonstrated how their puckering and electric dipole orientations can be switched through the application of either stress or an electric field, which is essential for storing information. Their band structure was also investigated, and it was found that the two valleys located in two different principal axes of the Brillouin zones can be excited selectively using linearly polarized light. By understanding the selection rules, optical transitions can be used to address bits of information. The results are important, as maintaining ferroelectricity in atomically thin films remains a challenge due to depolarization and technologically important for potential devices.

- As DFT is limited to small system sizes, Chapter 4 introduces TB models for two atoms with strong-spin orbit interaction arranged in a square lattice. Theoretical predictions are developed on the emergence of Rashba (Dirac) points as a result of symmetry breaking and strong spin orbit interaction. Finally, the effects of external electro magnetic fields on this material are investigated. Some consequences include Dirac shift in momentum space as well as the occurrence of Landau levels.

- Chapter 5 proposes a new class of ferroelectric Rashba materials. DFT calculations were used to show that lead chalcogenide monolayers PbX (X=S, Se, Te) have buckled (noncentrosymmetric) structures which are energetically more stable than the planar. The heavy lead atom together with non-centrosymmetric

structure results in Rashba-Dirac cone with a helical Rasba type spin-texture. Further, it was found that the material is ferroelectric and the spin-texture can be reversed by switching the electric polarization or buckling direction. A unifying framework based on tight binding (TB) formulations was then developed, which was confirmed by DFT simulation results, and which is applicable for generic buckled free-standing square 2D materials MX (M=Pb, Sn; X=S, Se, Te). In particular, it is addressed how the strength of SOI and the degree of buckling (inversion symmetry breaking term) determine the bands structure, spin splitting, and orbital-spin texture. This understanding enables the manipulation of the spins and Dirac cones via mechanical strains. Moreover, it was investigated how spin chirality couples to orbital texture, a topic that is very new in the studies of ferroelectric Rashba semiconductors (FERSC).

- As a follow-up study, it was investigated how strains modify electronic and spin states in lead chalcogenides monolayers. In Chapter 6, a TB theory was developed using continuum mechanics, validated by DFT calculations, to predict strain-dependent changes in the spin and electronic properties of ferroelectric Rashba lead chalcogenides PbX (X=S, Se, Te). The strain-dependent TB mode enables finding a relationship between the Rashba field and the out-of-plane strain or electric polarization from a microscopic view, a connection that is not well understood in the ferroelectric Rashba materials. This work is important to overcome the size and computational limitations associated with DFT. The developed strain-dependent TB model can be used in conjunction with a classical atomistic simulation (e.g MD) to calculate the effect of inhomogeneous strain due to thermal effects, substrates, defects etc., on the Rashba parameter over the large spatial regions that are relevant to experiments. Third, the

approach goes beyond previous TB studies by including angular effects (bond orientation) and lattice deformation effects of strain on hopping parameters, which are often ignored in many studies. It is found that the strains induce gauge fields in the low-order energy Hamiltonian near the symmetry point. The fields shifts the Rashba point and modify the Rashba parameter, which is equivalent to applications of in-plane magnetic fields by minimal coupling substitution. The out-of-plane strain, which is roughly proportional to the electric polarization, is also shown to modify the Rashba parameter. In particular the strain and electrical control of the Rashba effect is of practical interest because it allows the manipulation of spin states using electric fields (or strains) rather than magnetic fields.

- The last two chapters focus on studies of defects engineering in 2D materials. In Chapter 7, it is investigated how cuts (holes) alter the mechanical properties of MoS_2 and graphene. The results of classical molecular dynamics simulations are reported which focus on studying the mechanical properties of MoS_2 kirigami. The key finding is significant enhancements in tensile yield and fracture strains as compared to pristine MoS_2 nanoribbons, particularly for zigzag MoS_2 that enable yield strain increases by factors of up to four and fracture strain enhancements by factors of up to six. These results in conjunction with recent results on graphene suggest that the kirigami approach may be a generally useful one for enhancing the ductility of two-dimensional materials.

- Lastly, a ML approach to design 2D materials is introduced. The ML models such as convolutional neural networks (CNN) and fully-connected neural networks (NN) are first used to approximate the objective functions such as yield strain and yield stress in the context of supervised learning. This work

is the first demonstration of the applicability of ML to predict stretchability in graphene kirigami. Having found the appropriate ML model to predict targeted function, the CNN is then used as a search algorithm. The objective is to maximize stretchability under certain constraints, such as number of allowed cuts. It is demonstrated that the CNN search is able to find the optimal solutions with only 1000 training data points in a large design space of roughy 4,000,000.

Chapter 2

Computational Methods

2.1 Multiscale Modeling Approaches and Their Limitations

In this chapter we give an overview of different computational approaches employed in this thesis, indicating their advantages and their limitations. In the first part of this chapter we provide a basic understanding of some of the advantages and limitations of the density functional theory (DFT) and molecular dynamics (MD) approaches we use to study the properties of materials. We shall discuss and derive the basic concepts and algorithms that are used in DFT and MD methods. In the second part of this chapter, we will discuss the "machine learning" approaches we will use to further explore how to design materials with specific features. Here we provide basic aspects of neural network models, focusing on convolutional neural networks.

2.1.1 Density Functional Theory

Properties of materials are governed by quantum interactions among electrons and ions. For many-electron systems, solving the full N interacting electron problem is not feasible with the current computing capabilities. For this reason, several approximations have been developed to tackle this problem. Today *ab initio* calculations based on density functional theory (DFT) are the most commonly used method to

simulate and calculate properties of a material. DFT is a variational approach for solving many-electron system by finding the ground-state electron *density* instead of the electronic wave functions. The early ideas were developed by Thomas [52], Fermi [53], and Dirac [54] and later by Hohenberg, Kohn and Sham [55, 56].

The Hamiltonian of a solid consisting electrons and ions can be described by

$$H = \sum_i \frac{\hbar^2}{2m_e}\nabla^2_{\mathbf{r_i}} + -\frac{1}{2}\sum_{i\neq j}\frac{e^2}{|\mathbf{r_i}-\mathbf{r_j}|} \tag{2.1}$$

$$\sum_I \frac{\hbar^2}{2M_I}\nabla^2_{\mathbf{R_i}} + -\frac{1}{2}\sum_{I\neq J}\frac{Z_I Z_J e^2}{|\mathbf{R_i}-\mathbf{R_j}|} \tag{2.2}$$

$$-\frac{1}{2}\sum_{i,I}\frac{Z_I e^2}{|\mathbf{R_i}-\mathbf{ri}|}, \tag{2.3}$$

where m_e, $\mathbf{r}$, e, are the mass, the position, and the electronic charge of an electron, respectively. M, $\mathbf{R}$ and Z are the mass, the position, and the valence charge of an ion, respectively. The first and the third terms are the total kinetic contributions from electrons and ions, respectively. The second and the fourth terms are the electrostatic potential energy between the electrons only and the ions only, respectively. The last term is the electrostatic potential energy between the electrons and the ions. The first approximation is to assume the solid to be a perfect crystal (homogenous) so that by periodic boundary conditions we can reduce the $N \sim 10^{23}$ atoms in a real material to the number of atoms in the repeating unit cell. Current quantum mechanical calculations (e.g. DFT) can solve systems of sizes up to a few nanometers (around hundreds of atoms) within reasonable computational times.

The next approximation is to treat the ions as *static* particles, as the electron mass is much smaller than the ionic mass. Within this approximation, the electrons are moving at a different time scale compared to the ions. This approximation is known

as the *Born-Oppenheimer* or adiabatic approximation. The Hamiltonian becomes simpler, as now it contains kinetic energy of electrons and the interaction between electrons and the effective potential, and the potential experienced by the electrons due to the ions.

2.1.1.1 Hohenberg and Kohn Theorem

Hohenberg, Kohn, and Sham further developed a variational approach that became the theoretical basis of the modern DFT [55, 56]. Hohenberg and Kohn showed that the external potential $v(\mathbf{r})$ is a unique functional of the electron density $n(\mathbf{r})$, where the $n(\mathbf{r})$ is given by

$$n(\mathbf{r}) = N \int \Psi^*(\mathbf{r}, \mathbf{r}_2, \dots \mathbf{r}_N)\Psi(\mathbf{r}, \mathbf{r}_2, \dots \mathbf{r}_N) d\mathbf{r}_2 \dots d\mathbf{r}_N. \tag{2.4}$$

Let H and H' be the two Hamiltonians and Ψ and Ψ' be the ground state wavefunctions, respectively. Suppose that $v(\mathbf{r})$ and $v'(\mathbf{r})$ are the two external potentials that lead to the electronic ground state. The ground state energies E and E' are given by

$$\begin{aligned} E =& \langle \Psi | H | \Psi \rangle \\ E' =& \langle \Psi' | H' | \Psi' \rangle. \end{aligned} \tag{2.5}$$

Then by the variational principle,

$$\begin{aligned} E' < \langle \Psi | H' | \Psi \rangle =& \langle \Psi | H - v + v' | \Psi \rangle \\ =& E + \langle \Psi | v' - v | \Psi \rangle, \end{aligned} \tag{2.6}$$

and similarly,

$$\begin{aligned} E < \langle \Psi' | H | \Psi' \rangle =& \langle \Psi' | H' - v' + v | \Psi' \rangle \\ =& E' + \langle \Psi' | v - v' | \Psi' \rangle. \end{aligned} \tag{2.7}$$

Adding Eq. 2.6 and Eq. 2.7, we obtain

$$E + E' < E + E' + \langle \Psi' | v - v' | \Psi' \rangle + \langle \Psi | v' - v | \Psi \rangle \tag{2.8}$$

Since we have assumed that both H and H' have the same ground state charge density then

$$\langle \Psi_1 | v' - v | \Psi_1 \rangle = \langle \Psi' | v' - v | \Psi' \rangle = \int n(\mathbf{r})[v'(\mathbf{r}) - v(\mathbf{r})] d\mathbf{r}, \tag{2.9}$$

and we obtain $E+E' < E+E'$ which is not correct. This proves by contradiction that the assumption v and v' are different is incorrect. Thus the wavefunction must be *a unique functional* of charge density since there is one-to-one correspondence between the ground state wavefunction and the external potential. Now we can write Eq. 2.3 as

$$H = F[n(\mathbf{r})] + \int v(\mathbf{r}) n(\mathbf{r}) d\mathbf{r}, \tag{2.10}$$

where F contains the kinetic term and the electron-electron potential energy, and the second term contains the interaction between the electrons and the ions. The last term is not difficult to calculate. In the modern DFT packages, pseudopotentials are used to calculate the Coulomb interactions between valence electrons and ions and core electrons. Describing in detail the theoretical basis for the development of pseudopotentials and exchange correlations is beyond the scope of this thesis.

Interested readers are encouraged to read Refs. [39, 40].

2.1.1.2 Single-Particle Picture

To further approximate Eq. 2.1.1.1, we assume that the many-body wavefunctions can be written as a set of many *non-interacting* single particle wavefunctions. The charge density becomes

$$n(\mathbf{r}) = \sum_i |\phi_i(\mathbf{r})|, \tag{2.11}$$

$\phi_i(\mathbf{r})$ is the single particle wavefunction (or orbital). We can decompose $F[n(\mathbf{r})]$ to

$$F[n(\mathbf{r})] = T_s[n(\mathbf{r})] + E[n(\mathbf{r})] + V_{\mathrm{XC}}[n(\mathbf{r})], \tag{2.12}$$

where $T_s[n(\mathbf{r})]$ is the kinetic term of the non-interacting electrons, $E[n(\mathbf{r})]$ is the classical electrostatic potential, and $V_{\mathrm{XC}}[n(\mathbf{r})]$ is the exchange correlation energy, which important to make $F[n(\mathbf{r})]$ close to the exact function. We then can write the Schrödinger equation in the single-particle picture, known as the Kohn-Sham equation, as

$$\Big[-\frac{\hbar}{2m_e}\nabla_r^2 + \underbrace{V(\mathbf{r}) + \int \frac{e^2 n(\mathbf{r}')}{|\mathbf{r}-\mathbf{r}'|} d\mathbf{r}' + V_{\mathrm{XC}}[n(\mathbf{r})]}_{v^{\mathrm{eff}}} \Big] |\phi_i(\mathbf{r})\rangle = \epsilon_i |\phi_i(\mathbf{r})\rangle. \tag{2.13}$$

The first term is the kinetic energy and the second term is the effective potential experienced by an electron due other electrons, the ions, and the exchange potential. These single-particles are known as Kohn-Sham orbitals and they are not really the *real* electrons. Kohn-Sham equation has to be solved iteratively in a self-consistent manner. Usually an initial guess of the density is chosen and then v^{eff} is calculated and followed by solving the eigenvalue problem. The resulting eigenvectors are then

used to calculate the next charge density. This iterative procedure is continued until the charge density is converged.

2.1.1.3 Structural Optimization within Density Functional Theory

Due to vacuum or other interfacial effects, 2D monolayers often have structures that are different from their bulk counterparts. To find stable phase of a material in 2D (free-standing or on a substrate), the atomic positions and lattice vectors need to be relaxed. Classically, the force acting on a particle at $\mathbf{r_i}$ is given by the derivative of the potential energy $\mathbf{f}_i(\mathbf{R}) = -\nabla_{\mathbf{R}} U(\mathbf{R})|_{\mathbf{R}=\mathbf{r}_i}$. Quantum mechanically we expect

$$\begin{aligned} \mathbf{f}(\mathbf{R}) &= -\nabla_{\mathbf{R}} \langle E \rangle \\ &= -\nabla_{\mathbf{R}} \langle \Psi | H | \Psi \rangle. \end{aligned} \tag{2.14}$$

The Hellman-Feyman theorem states that for any perturbation λ we have

$$\begin{aligned} \frac{\partial \langle E \rangle}{\partial \lambda} &= \langle \frac{\partial \Psi}{\partial \lambda} | H | \Psi \rangle + \langle \Psi | \frac{\partial H}{\partial \lambda} | \Psi \rangle + \langle \Psi | H | \frac{\partial \Psi}{\partial \lambda} \rangle \\ &= E \Big[\langle \frac{\partial \Psi}{\partial \lambda} | \Psi \rangle + \langle \Psi | \frac{\partial \Psi}{\partial \lambda} \rangle + \langle \Psi | \frac{\partial H}{\partial \lambda} | \Psi \rangle \\ &= E \frac{\partial}{\partial \lambda} \langle \Psi | \Psi \rangle + \langle \Psi | \frac{\partial H}{\partial \lambda} | \Psi \rangle \\ &= \langle \Psi | \frac{\partial H}{\partial \lambda} | \Psi \rangle. \end{aligned} \tag{2.15}$$

This is what we needed to calculate Eq. 2.14. Here we have assumed that Ψ is normalized and is an eigenstate of H. This means that once we find the electronic ground state we can find the energy, and then calculating the forces acting on the ions (and stresses) should be straight forward. In the modern DFT packages, the relaxed structure can be found after iterations of *electronic* convergence followed by

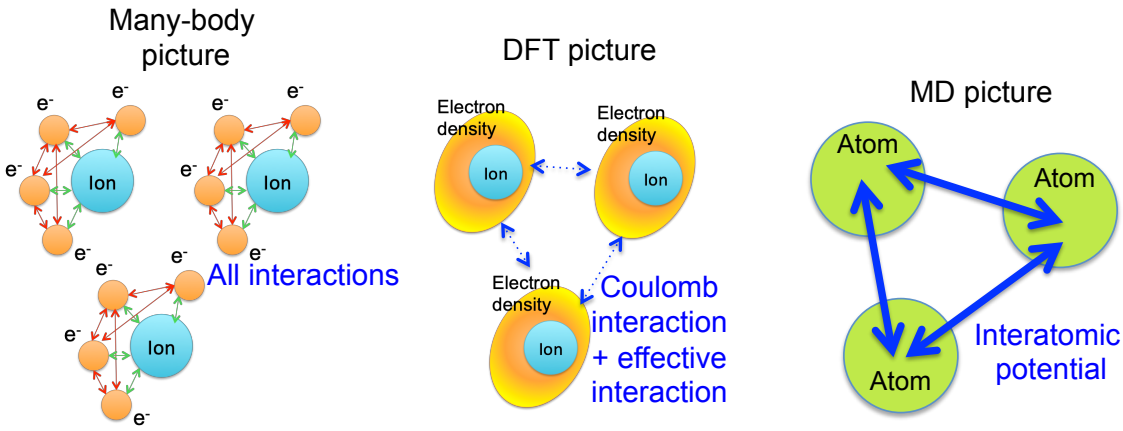

Figure 2.1: The schematic of coarse-graining from a full many-body approach to DFT and from DFT to MD.

force and stress convergence. A force and stress tolerance are chosen based on a desired accuracy; these choices may vary for different systems. The typical stress tolerance is around 0.01 GPa and the typical force tolerance is around 0.01 eV/Å.

We want to note that finding the ground-state *structure* is a classical optimization problem. Depending on how complex the system is, there could be multiple minima. We can find the structural ground-state solution pretty quickly if we provide a good starting configuration. This is the reason why using a structure obtained from the bulk configuration is often helpful to get fast convergence to the relaxed structure in the monolayer form.

2.1.2 Molecular Dynamics

Molecular Dynamics (MD) is a popular coarse-grained method to simulate the dynamics of solid materials as well as liquids. Unlike DFT, MD treats the nuclei and their surrounding electrons as one entity. As explained in the earlier section, within the Born-Oppenheimer approximation, nuclei is treated *classically* and for classical MD the effect of electrons is approximated as a potential energy surface. This ap-

proximation leads to treating the atoms with classical Newtonian mechanics. To gain an accurate description of the physics, effective interatomic potentials need to be developed. The interatomic potentials are appropriate for describing structural and conformal changes but not for chemical reactions or calculating quantum mechanical properties (e.g. band structures). There are different ways to develop the interatomic potentials; the details of these approaches are beyond the scope of this thesis. In this section we will outline the basics of MD; more thorough details on MD can be found in Refs. [42, 57].

The basic idea of MD is to evolve the position $\mathbf{x}_i$ and the momentum $\mathbf{p}_i$ of an atom with Newtonian mechanics. In a system with N atoms, we have a set of $3N$ second-order differential equations to solve. For each particle, the acceleration is given by

$$\frac{d^2\mathbf{r}_i(t)}{dt^2} = \frac{1}{m_i}\mathbf{f}_i(\{\mathbf{r}\}, t) \tag{2.16}$$

where m_i is the mass of the ith atom and f_i is the force acting on it. The force is given by taking the gradient of the potential $\mathbf{f}_i = -\nabla_i U$, where U is the external potential experienced by the atom i. Often because of the locality of the interactions (which diminish rapidly with increase in distance), only contributions from the local neighbors are included in the calculations. This approximation reduces the computational cost from $\mathcal{O}(N^2)$ (including all pairwise interactions) to $\mathcal{O}(N)$. However, we still need to perform an $\mathcal{O}(N^2)$ calculation to correctly find the neighboring atoms for each atom. After finding the neighboring-list, $\mathcal{O}(N)$ calculations are carried out to calculate the all the forces and loop over the number of cells (partitions).

It is clear that we need to solve Eq. 2.16 to find the updated $\mathbf{x}$ and $\mathbf{p}$. Choosing the right integration scheme to solve the dynamics numerically is critical. The simplest

interaction scheme is the Euler method,

$$\begin{aligned}\mathbf{r}_i(t+\Delta t) &= \mathbf{r}_i(t) + \mathbf{v}_i(t)\Delta t + \frac{\Delta t^2 \mathbf{f}_i(t)}{2m_i} + \mathcal{O}(\Delta t^3) \\ \mathbf{v}_i(t+\Delta t) &= \mathbf{v}_i(t) + \frac{\Delta t\, \mathbf{f}_i(t)}{m_i} + \mathcal{O}(\Delta t^2),\end{aligned} \tag{2.17}$$

where $\mathbf{v}_i = \mathbf{p}_i/m_i$ is the velocity and Δt is the time step. The time scale for molecular vibrations is on the order of picoseconds (10^{-12}s) and the typical time step is usually chosen to be on the order of femtosecond (10^{-15}s). The simple Euler algorithm, however, is not ideal for MD because it is neither phase-space preserving nor time-reversible. Hence, the most widely used algorithm for updating positions and momentums in MD is Velocity-Verlet algorithm,

$$\begin{aligned}\mathbf{r}_i(t+\Delta t) &= \mathbf{r}_i(t) + \mathbf{v}t_i(t)\Delta t + \frac{\Delta t^2 \mathbf{f}_i(t)}{2m_i} + \mathcal{O}(\Delta t^3) \\ \mathbf{v}_i(t+\Delta t) &= \mathbf{v}_i(t) + \frac{\Delta t(\mathbf{f}_i(t) + \mathbf{f}_i(t+\Delta t))}{2m_i} + \mathcal{O}(\Delta t^2).\end{aligned} \tag{2.18}$$

The Velocity-Verlet is algorithm favorable because it is stable and preserves the volume in the phase-space.

The setup we described so far is known as micro-canonical ensemble (NVE ensemble) where the number of atoms N, volume V, and energy E are fixed. In our studies, we are interested in a system at a fixed temperature and thus a "thermostat" is added to the simulation. For details, interested readers are referred to Ref. [42]. The schematic of coarse-graining from many-body to DFT then to MD is shown in fig. 2.1.

2.2 Machine Learning Methods

In the computational methods described above, both DFT and MD methods have *well-defined* physical principles and assumptions that are used to model a complex system. Recently, machine learning (ML) has become popular for analyzing complex systems, from physical to social systems. The basis of learning from data, known as the data-driven approach, is to have inputs and outputs to build a model, in contrast to have inputs and a specified model to get the outputs. This is essential because solutions based on some underlying physics principles are often not known for very complex systems. Many modern ML models have been shown to be *expressive* and *efficient* when it comes to predicting the output values (supervised learning) or learning some structures in unlabeled data (unsupervised learning). An expressive model means that the model can approximate any arbitrary function. ML models in particular have become widely used across many systems because of the time and space efficiencies for learning from a large amount of data, which is possible in part due to the increase in computing power. Many modern ML algorithms scale well with the size of the dataset because of the advances in highly optimized algorithms implemented in parallel and GPU (Graphical Processing Unit) computing [58]. There are many choices of ML techniques (linear model, support vector machine, random forest, neural networks, k-nearest neighbors, etc.), and a given model is often chosen based on problem specifics, the size of dataset, and the computing capabilities [58, 59, 60]. In this section we will start with giving an overview of theoretical basis and how to train linear model which is the simplest supervised machine learning model. We then further discuss the basic concepts of modern machine learning techniques focusing on neural networks and convolutional neural networks, which are particularly suitable for the problem of designing defects in 2D materials.

2.2.1 Linear Model

The Hamiltonian (or any physical quantity) of many physical systems in nature can be expanded as a power series. We then can approximate the function of interest f as

$$f(\boldsymbol{x}) = \beta_0 + \sum_i \beta_i x_i + \sum_{i \leq j} \beta_{ij} x_i x_j + \sum_{i \leq j \leq k} \beta_{ijk} x_i x_j x_k + \dots . \tag{2.19}$$

For m samples, we can write Eq. 8.3 as a linear function $f(\boldsymbol{x}) = \mathbf{X} \cdot \boldsymbol{\beta}$, where

$$\mathbf{X} = \begin{pmatrix} 1 & x_1^{(1)} & \dots & x_n^{(1)} & x_1^{(1)} x_2^{(1)} & \dots \\ \vdots & \ddots & & & & \\ 1 & x_1^{(m)} & \dots & x_n^{(m)} & x_1^{(\mathrm{m})} x_2^{(m)} & \dots \end{pmatrix}, \tag{2.20}$$

and $\boldsymbol{\beta}^T = (\beta_0, \beta_1, \dots, \beta_n, \beta_{12}, \dots)$. Suppose that the length of $\boldsymbol{\beta}$ is p. In the machine learning language this is equivalent to applying features transformation to the input vectors [58, 59, 60]. To find $\boldsymbol{\beta}$, mean squared difference between the predictions $\hat{\boldsymbol{y}} = f(\boldsymbol{x})$ and the true values $\boldsymbol{y}$ is minimized. This method is known as ordinary least square regression method. We want to minimize a mean squared loss given by

$$\begin{aligned} \mathcal{L} =& ||\mathbf{X}\boldsymbol{\beta} - \boldsymbol{y}||^2 \\ =& (\boldsymbol{\beta}^T \mathbf{X}^{\mathbf{T}} - \boldsymbol{y}^{\mathbf{T}})(\mathbf{X}\boldsymbol{\beta} - \boldsymbol{y}) \\ =& (\boldsymbol{\beta}^T \mathbf{X}^{\mathbf{T}} \mathbf{X}^{\mathbf{T}} \boldsymbol{\beta} - \boldsymbol{y}^{\mathbf{T}} \mathbf{X}\boldsymbol{\beta} - \boldsymbol{\beta}^{\mathbf{T}} \mathbf{X}^{\mathbf{T}} \boldsymbol{y} + \boldsymbol{y}^{\mathbf{T}} \boldsymbol{y}) \\ =& (\boldsymbol{\beta}^T \mathbf{X}^{\mathbf{T}} \mathbf{X}^{\mathbf{T}} \boldsymbol{\beta} - \mathbf{2}\boldsymbol{\beta}^{\mathbf{T}} \mathbf{X}^{\mathbf{T}} \boldsymbol{y} + \boldsymbol{y}^{\mathbf{T}} \boldsymbol{y}), \end{aligned} \tag{2.21}$$

where we have used the fact the transpose of a scalar is a scalar $(\boldsymbol{y}^T \mathbf{X}\boldsymbol{\beta})^T = \boldsymbol{\beta}^T \mathbf{X}^T \boldsymbol{y}$. We can find the analytic expression of β by finding the minima of $\mathcal{L}$ which is by

setting $0 = \frac{\partial \mathcal{L}}{\partial \boldsymbol{\beta}}$. And after taking derivative we obtain,

$$\begin{aligned} 0 =& 2\mathbf{X^T X\beta} - \mathbf{2X^T y} \\ \boldsymbol{\beta} =& (\mathbf{X^T X})^{-1}\mathbf{X^T y}, \end{aligned} \tag{2.22}$$

where we have used the fact that $\frac{\partial \boldsymbol{y}^T \boldsymbol{y}}{\partial \boldsymbol{\beta}} = 0$. Note that here we assume that $\mathbf{X^T X}$ is invertible and this is the case when $m > p$. In the case where $p > m$ there are infinitely many solutions to $\boldsymbol{\beta}$ as $\boldsymbol{X}$ is not linearly independent. Another simple approach to find the optimal values of $\boldsymbol{\beta}$ is to employ gradient descent optimization method. We have obtained the derivative of the cost function from Eq. 2.22, the coefficients $\boldsymbol{\beta}$ that can be updated iteratively as

$$\boldsymbol{\beta}_{t+1} = \boldsymbol{\beta}_t - \eta_t \mathbf{X^T}(\mathbf{X\beta_t} - \boldsymbol{y}), \tag{2.23}$$

where η_t is a learning rate which controls how large is the step taken in the direction of the gradient. Choice of η_t is crucial to achieve a fast convergence. A very small η_t guarantees to find a *local minima*, but this would require many steps to reach a local minima. A large η on the other hand might overshoot the solution and make the algorithm become unstable. It can be seen that depending on the structure of the cost function the η_t has to be changed adaptively and η_t, in principle, should have different values in each direction. The optimal values of η_t for each component can be found from the Hessian matrix (encodes the local curvature)

$$\mathbf{H_{ij}} = \frac{\partial^2 \mathcal{L}}{\partial \mathbf{x_i} \partial \mathbf{x_j}}\,. \tag{2.24}$$

Calculating a Hessian is computationally expensive especially in a high multidimensional space [59, 60]. Adding stochasticity is also important to escape from local minimas. Many stochastic optimizations techniques with adaptive learning rate (e.g. Adaptive Gradient Algorithm (AdaGrad), Root Mean Square Propagation (RMSProp), ADAM) have been developed to get convergence within reasonable time [58, 59, 60].

2.2.2 Neural Networks

Similar to linear model, a fully-connected Neural Network (NN) is a mathematical function that maps input values to another output values. The underlying concept of a NN was inspired by the biological network in animals brain (perceptron) [58]. The main advantage of NN and other deep learning methods is that they enable feature extractions and transformations of complex representations (usually in a vector representation) to much simpler ones without the need of hand-engineering the transformations. To describe the NN computation, we will denote h as the number of neurons in a hidden layer l. In each layer of a NN, the computation (affine transformation) is given by

$$a^{(l+1)} = g(W^{(l)}a^{(l)} + b^{(l)}), \tag{2.25}$$

where g is the non-linear activation function, $a^{(l)}$, $b^{(l)}$, $W^{(l)}$ are the activations, bias, and the weights in a layer l. Deep neural networks are essentially a composition of many affine transformations followed by non-linear transformations, which can be written as

$$f(\boldsymbol{x}) = g^{(L)}A^{(L)}g^{(L-1)} \cdots g^{(2)}A^{(2)}g^{(1)}A^{(1)}\boldsymbol{x}, \tag{2.26}$$

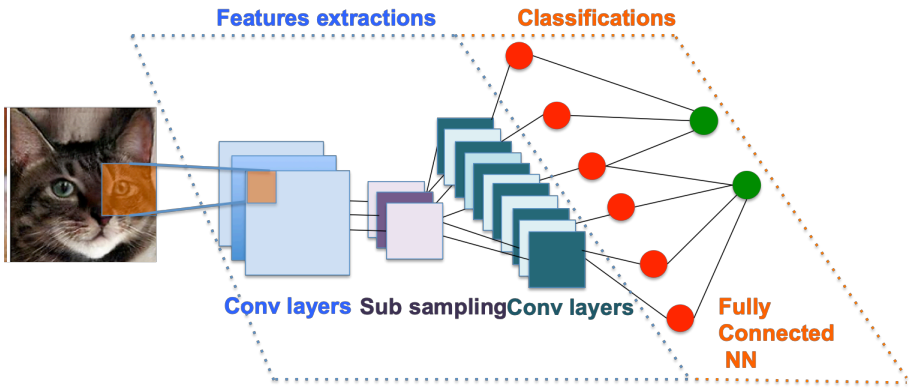

Figure 2.2: A schematic of a typical CNN model. Each convolutional layer is usually followed by max pooling layers, and finally fully-connected layers.

where A^l is the affine transformation and L is the number of layers.

There are several choices of non-linear activation functions. The most common are the sigmoid function $g(z) = \frac{1}{1+e^z}$, the hyperbolic tangent $g(z) = \tanh(z)$, and rectified linear units (ReLU) $g(z) = \max(0, z)$ [58, 60]. Training deep networks is often difficult as the information needs to be transmitted through many layers. This problem is known as the vanishing or exploding gradient problem. ReLU has become the most popular activation function for training deep networks, because unlike the sigmoid function, the gradient of ReLU function does not vanish at large z.

Next we will discuss the basic architecture of convolutional neural networks (CNN). Similar to NN, CNN was inspired by the biological processes found in the animal visual cortex. One major difference of CNN is that CNN uses filters to convolve the input. The schematic of a typical CNN is shown in fig. 2.2. By moving a filter (window) across the image (for the 2D case), the weights are learned. CNN in particular exploits two concepts (i) locality and (ii) shared weights. Because the nature of the receptive fields (filters), the convolutional layers enforce local connectivity. This concept is important and very useful to study systems that have local interactions. Indeed, many physical systems have interactions that are local in space.

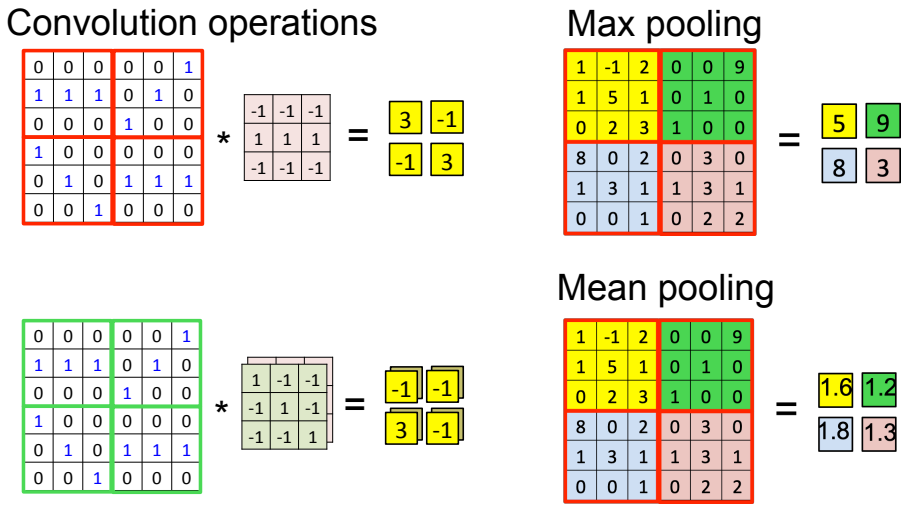

Figure 2.3: The illustration of convolution operations and max- and mean pooling on images. In this example, the first filter detects the horizontal lines while the second filter detects the diagonal line. In the *real* training, the weights are updated during the training phase.

Second, as the filters are moved across the input, some parts of the input will have same responses without the need of having additional filters. This allows the detection of specific features using the same filter regardless the location of the feature in the input.In physics, we encounter this same important concept of *translation invariance*. The parameter sharing and enforcing local connections reduce number of weights (parameters to be learned), and this gives CNN advantages over NN, as the fully-connected one will have many redundant weights to describe the same transformation map. The convolution operations, are illustrated in fig. 2.3. In the examples, the filters are used to detect horizontal lines and diagonal lines.

Because of all these advantages, CNN is the most commonly used deep learning method for categorizing images. In addition to convolutional layers and fully-connected layers, pooling layers are often used in deep CNNs [58, 60]. Pooling layer is useful to reduce the size of the inputs, i.e. summarizing information passed from the previous layer. Down-sampling a representation of images is useful to reduce

the computational cost as the down-sampling reduces number of parameters that need to be learned. The most commonly used pooling layers are max-pooling and mean-pooling. Max pooling operation is done by taking only maximum values of subregions of the initial representation, while mean pooling is taking the mean of subregions the initial representation. The convolution operations, max-pooling and mean pooling operations are illustrated in fig. 2.3. After passing the input through convolutional layers, fully-connected layers are often added to further transform the extracted features (e.g. edges) in order to produce a desired objective function, such as for classification or regression task. The architecture a typical CNN is shown in fig. 2.2.

At the end of the final layer, a loss function is chosen to evaluate the performance of the model. The most commonly used loss functions are the cross-entropy for classification tasks and the mean-squared for regression tasks. The mean-squared loss function is given by

$$\mathcal{L}(\hat{\boldsymbol{y}}_i, \boldsymbol{y}_i) = \sum_i^m |\hat{\boldsymbol{y}}_i - \boldsymbol{y}_i|^2, \tag{2.27}$$

where $\boldsymbol{y}$ is the true value, $\hat{\boldsymbol{y}} = f(\boldsymbol{x})$ is the predicted value, and m is number of samples. During the training the loss function is minimized, as the goal is to build a model that outputs values close to the true model. The weights in the filters and neurons are updated using the forward and back propagation algorithm [61]. We also want to note that there are many "tricks" to train deep networks, such as ways to avoid overfitting with dropout and other regularization schemes, and choices of optimizers to update the weights. The technical details can be found in machine learning books (e.g. Ref. [58]) and a review on introduction to machine learning intended for physicists [60].

2.3 Summary

From this chapter, we see that there are clearly different methodologies and approximations used in DFT and MD simulations. DFT approximation is closer to the true model of representing materials. The quantum mechanical treatments on the many-electrons allow DFT to study chemical reactions and other electronic properties. This approach comes at a computational cost with computational time scaling like $\mathcal{O}(N^3)$, where N is the number of *electrons*. The MD approach on the other hand does not treat the electrons quantum mechanically. By treating nuclei and electrons as one entity, MD does not find the electronic ground state. The time complexity of MD goes like $\mathcal{O}(N^2)$, where N is number of *atoms*. This allows MD to simulate thousands to millions of atoms, while only a few hundreds of atoms can be simulated in DFT. To get a good accuracy, however, MD relies heavily on good interatomic potentials. In the last part of the chapter, we introduced some basics of NN and CNN and outlined some advantages of using machine learning approach to build an effective model without knowing the underlying physical principles.

Chapter 3

Polarization and Valley Switching in Monolayer Group-IV Monochalcogenides

Recently, puckered layered materials (such as black phosphorus and the group-IV monochalcogenides) have been added to the list of two-dimensional (2D) electronic membranes. These newer materials have many important new properties which differ from those of the most studied 2D materials, graphene and the transition metal dichalcogenides. Apart from interesting basic physics questions, these materials promise many novel applications, ranging from photovoltaics and piezoelectrics to valleytronic devices.

In this chapter, we present the studies of two structural phases of SnS and GeSe and demonstrate how their puckering and electric dipole orientations can be switched through the application of either stress or an electric field, which is essential for storing information. Further, we studied the band structure and found that the two valleys located in two different principal axes of the Brillouin zones can be excited selectively using linearly polarized light. By understanding the selection rules, we are able to address bits of information (orientation of the puckering or electric dipole) using optical transitions.

Our key findings are (i) SnS and GeSe are suitable for ferroelectric devices as their polarizations can be controlled through application of electric field and (ii) the

dipole states can then be detected by an optical transition since the band structure is governed by the puckering orientation. Our results are scientifically important, as maintaining ferroelectricity in atomically thin films remains a challenge due to depolarization and technologically important for potential devices. We also want to note that soon after our theoretical study, it has been shown *experimentally* that selective valley polarizations on different valleys (located orthogonally in Brillouin zone) can be achieved via linearly polarized light [62].

The work presented in this chapter (with slight modifications) has been published in:

- **P. Z. Hanakata**, A. Carvalho, D. K. Campbell, H. S. Park,
  "Polarization and valley switching in monolayer group-IV monochalcogenides,"
  Physical Review B 94 (3), 035304 (2016).

3.1 Introduction

The discovery of 2D materials that can be isolated into single layers through exfoliation and exhibit novel properties has established new paradigms for ultrathin devices based on atomically sharp interfaces [17, 18]. In particular, transition metal dichalcogenides (TMDs) have been studied extensively and have shown potential for many technological applications ranging from photovoltaics to valleytronic devices [12, 63, 64, 65, 66, 67, 68]. The family of monolayer 2D materials has recently grown to include other 2D semiconductors, such as phosphorene and related materials.

However, one of the features thus far lacking for applications both in 2D electronics and in valleytronics is non-volatile memory. Ferromagnetism, an essential element in spintronic memories, is believed to be achievable in graphene and other

2D materials but so far remains difficult to realize and control [69]. Ferroelectric memories, in which the information is stored in the orientation of the electric dipole rather than in the magnetization are a possible option. Single-layer graphene (SLG) ferroelectric field-effect transistors (FFET) with symmetrical bit writing have been demonstrated [70], but the prototypes rely on bulk or thin film ferroelectric substrates [70] or ferroelectric polymers [71], rather than on crystalline atomically thin ferroelectric materials. An altogether different approach to information storage relies on phase change materials, where the bit value corresponds to a distinct structural phase of the material. Researchers have recently optimized the phase switching energy by using superlattice structures where the movement of the atoms is confined to only one dimension [72].

In this article, we analyze the stability of group-IV monochalcogenide MX (M=Ge or Sn, and X=S or Se) monolayers, paying particular interest to their potential as memory functional materials. As prototypes, we use SnS and GeSe. In ambient conditions, bulk SnS and GeSe crystallize in the orthorhombic structure of the $Pnma$ space group. At 878 K, SnS goes through a second-order displacive phase transition into the β-SnS phase with $Cmcm$ symmetry [73, 74], which is also a layered phase that can be viewed as a distorted rocksalt structure. For bulk GeSe, such a phase transition has not been observed. Instead, at 924 K bulk GeSe transforms into the rocksalt phase ($Fm\bar{3}m$). This phase can also be stabilized using external pressure [75].

Similar to phosphorene [29, 76], $Pnma$ SnS and GeSe can be exfoliated [77, 78]. In monolayer form, they feature multiple valleys, large spin-orbit splitting[79] and a piezoelectric coefficient that surpasses that of the TMDs [80, 81]. Having an in-plane polar axis makes SnS and GeSe monolayers capable of a mechanical response to an

applied electric field.

Here, we use density functional theory (DFT) calculations to characterize the multistability of SnS and GeSe, exploring ways in which the phase transitions and domain switch can be triggered externally. We start by demonstrating how the reversible phase transition can be induced by uniaxial stress or electric field. Then, we show how the phase and lattice orientation states can be detected using the valley properties.

3.2 Computational Methods

The calculations were based on density functional theory (DFT) implemented in the QUANTUM ESPRESSO package [82]. The generalized gradient approximation (GGA) of Perdew-Burke-Ernzerhof (PBE) was used for the exchange and correlation functional, and Troullier-Martins type pseudopotentials [83]. The Kohn-Sham orbitals were expanded in a plane-wave basis with a cutoff energy of 70 Ry, and for the charge density a cutoff of 280 Ry was used. A k-point grid sampling grid was generated using the Monkhorst-Pack scheme with 10×10×1 points [84], and a finer regular grid of 80×80×1 was used for transition probability calculations. The equilibrium structures were found by using a conjugate-gradient optimization algorithm, and the energy landscape is mapped by relaxing the structure under constraints for each of the in-plane lattice parameters, while all the other structural parameters are allowed to relax. The input files can be found in A.0.1 and A.0.2.

We used the modern theory of polarization [85] to calculate the spontaneous polarization given by

$$\vec{\mathcal{P}} = \frac{1}{\Omega}\sum_{\tau} q_{\tau}^{\text{ion}}\mathbf{R}_{\tau} - \frac{2ie}{(2\pi)^3}\sum_{n}^{\text{occ}}\int_{BZ} d^3\mathbf{k}e^{-i\vec{k}\cdot\mathbf{R}}\left\langle u_{n\mathbf{k}}\middle|\frac{\partial u_{n\mathbf{k}}}{\partial\mathbf{k}}\right\rangle, \tag{3.1}$$

where q_τ is the ionic charge plus the core electrons, $\mathbf{R}_\tau$ is the position of ions, Ω is the unit cell volume, e is the elementary charge, n is the valence band index, $\mathbf{k}$ is the wave vector, and $u_{n\mathbf{k}}$ is the electronic wave function. The first term is the contribution from ions and core electrons, and the second term is the electronic contribution defined as adiabatic flow of current which can be calculated from the Berry connection [85]. The response of the material to a homogenous static external electric field is calculated based on methods developed by Refs. [86, 87] implemented in the QUANTUM ESPRESSO package [82].

3.3 Results

3.3.1 Multistability of SnS and GeSe in the Monolayer Phase

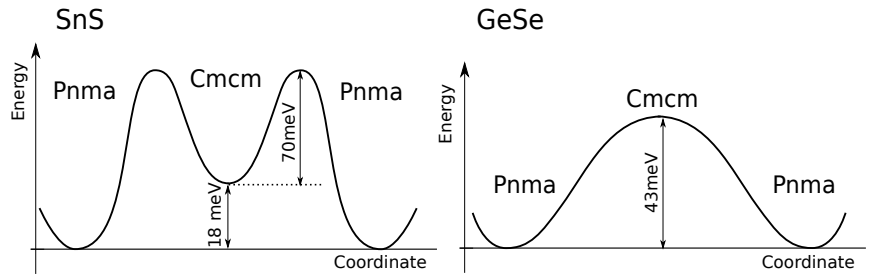

Figure 3.1: Schematic configuration-coordinate diagram for *Cmcm*-ML and *Pnma*-ML phases, in SnS and GeSe.

We start by exploring the energy landscape of monolayer SnS and GeSe. We consider the monolayer form of the two structures that are known for bulk SnS ie., a centrosymmetric structure (*Cmcm*), and the *Pnma* structure resembling black phosphorus, and which is the only known layered structure of bulk GeSe. We will designate the respective monolayer phases by appending 'ML' to the respective bulk space group.

The atomic positions in the *Pnma*-ML phase are $\pm$(M:0.25$\pm\delta$, 0.25, 0.05; X:0.25,

0.25, -0.05) in fractional coordinates, where M=(Sn, Ge) and X=(S, Se), $\delta = 0.06$ and 0.08 for SnS and GeSe, respectively. The *Cmcm*-ML phase is obtained by taking $\delta = 0$. As a result, the *Cmcm*-ML has two perpendicular mirror symmetry planes, as well as inversion symmetry, while *Pnma*-ML has no inversion symmetry. In our DFT simulations we used $\delta = 0.01$ as a tolerance to distinguish the *Pnma*-ML phase from the *Cmcm*-ML phase. We define puckering orientation as a unit vector of the in plane bond formed by the nearest neighbor of MX atoms in the direction of the broken mirror symmetry. For the SnS structure shown in Fig. 3.2(d), the puckering direction $\hat{d}_{\text{puck}} = \hat{x}$ as we define $\hat{d}_{\text{puck}} = \frac{\vec{x_{\text{S}}} - \vec{x_{\text{Sn}}}}{|\vec{x_{\text{S}}} - \vec{x_{\text{Sn}}}|}$.

The *Pnma*-ML and the *Cmcm*-ML phases can both be seen as distortions of a rocksalt bilayer that can be transformed into each other by a displacement of some of the atoms along $\hat{x}$ (see Fig.3.2 for $\hat{x}$ and $\hat{y}$ directions). The *Cmcm*-ML and *Pnma*-ML phases of SnS and GeSe monolayer have also been reported in Ref. [88]. By symmetry, there are four distinct *Pnma*-ML configurations (equivalent by $\pi/2$ rotations of the puckering direction). For SnS, *Cmcm*-ML is a local minima of the energy surface. For GeSe, the *Cmcm*-ML structure is not an energy minimum but a saddle point. The activation energy for reorientation of the *Pnma*-ML puckering direction is very small (88 meV for SnS and 43 meV for GeSe). We note that GGA has been successful in predicting the small enthalpy differences (tens of meV) between different phases of ferroelectric materials, because systematic errors cancel out when comparing systems with very similar structures [89]. The broken inversion symmetry and total energy with a typical double-well potential of SnS and GeSe are the first two indications that these materials may possess ferroelectricity.

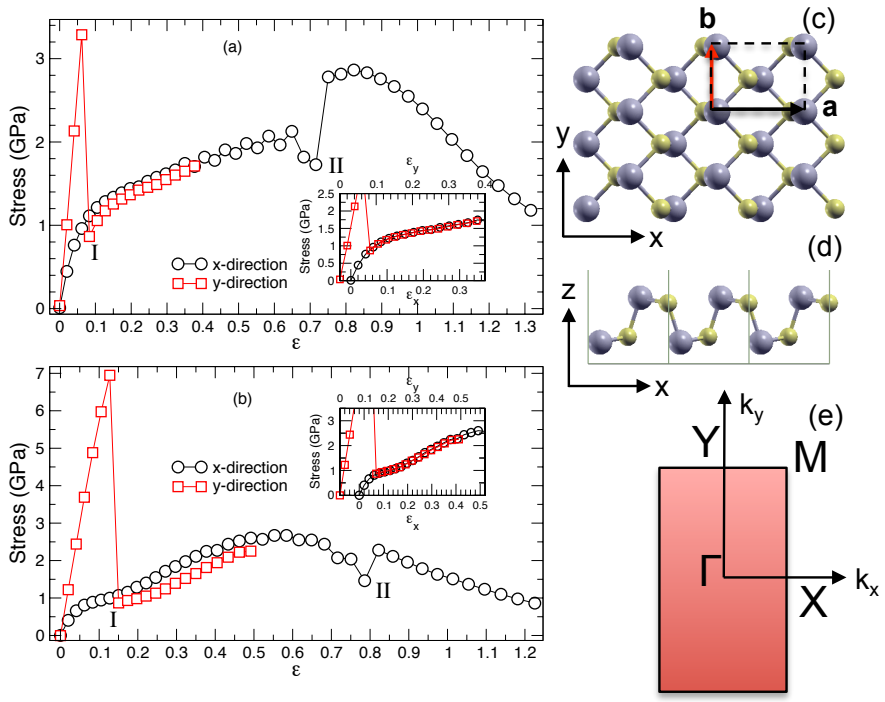

Figure 3.2: Stress-strain curves of monolayer (a) SnS and (b) GeSe for tensile strain along the $\hat{x}$ (black circle) and $\hat{y}$ (red square) directions. (I) indicates the *Pnma*-ML structure reconfiguration such that the puckering (armchair) direction $\hat{d}_{\text{puck}}$ becomes $\hat{y}$ instead of $\hat{x}$. (II) indicates the transformation into an hexagonal phase. In the insets of (a) and (b), the strain in the $\hat{y}$ direction was shifted to highlight the rotation of the *Pnma*-ML structure by $\pi/2$, swapping the armchair and zigzag directions. (c) and (d) top and side view of SnS structure with $\hat{d}_{\text{puck}} = \hat{x}$. The larger grey atom is Sn and the smaller yellow atom is S. (e) The respective Brillouin zone and the high symmetry points.

3.3.2 Application of Uniaxial Stress

The phase transition of SnS to *Cmcm*-ML, or equivalently the reorientation of the *Pnma*-ML structure, can be induced by in-plane uniaxial tensile stress (Fig. 3.2). We use an effective thickness to estimate the values of stress, as outlined in Ref. [81].

For uniaxial stress along $\hat{y}$, the SnS structure begins to resemble *Cmcm*-ML as the shorter lattice parameter b is stretched. For $\epsilon_y > 0.08$, uniaxial stress results in

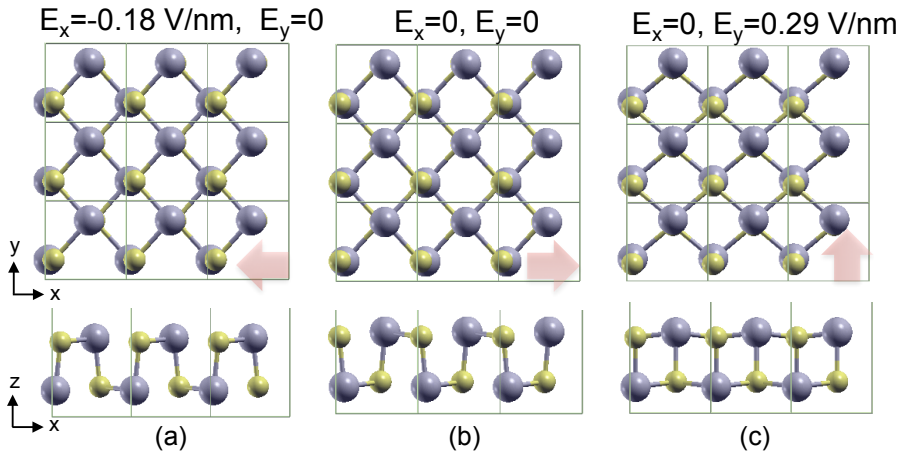

Figure 3.3: Structural visualization of clamped SnS monolayer under uniform electric field at points of transition. Puckering and electric dipole orientation (red arrow) can switch from positive $\hat{x}$ (b) to either negative $\hat{x}$ (a) or positive $\hat{y}$ (c) depending on the directions of applied electric field.

the rotation of the *Pnma*-ML structure by $\pi/2$. The puckering $\hat{d}_{\text{puck}}$thus rotates from $\hat{x}$ to $\hat{y}$ [Fig. 3.2(a), transition I]. Similar qualitative behavior is observed in GeSe (see Fig. 3.2(b)). Both SnS and GeSe transit to *Cmcm* phase, but they spontaneously revert back to *Pnma* once the tensile stress is removed [1].

The application of uniaxial stress along $\hat{x}$ reveals another phase transition at $\epsilon_x = 0.72$ and 0.78 for SnS and GeSe, respectively. The structure is a hexagonal phase resembling blue phosphorene (see Ref. [90]). The hexagonal structure and its band structure are plotted in Fig. 3.4.

3.3.3 Application of Electric Field

Application of an electric field is an alternative way to trigger the transition between different minima on the energy surface of SnS or GeSe. Since the *Pnma*-ML structure

[1] We found that once the stretch is removed the *Cmcm* structure spontaneously reverts back to *Pnma* for both SnS and GeSe. However, we found that during *compression*, the *Cmcm* phase of SnS is stable.

is piezoelectric, the application of an electric field along the polar ($\hat{x}$) direction in a mechanically free sample induces strain as well [81]. However, here we will consider, for simplicity, the application of an electric field to a mechanically clamped sample.

The spontaneous polarization in the *Pnma*-ML phase, which was measured with respect to the centrosymmetric structure by taking as the effective volume the equivalent volume occupied by a layer of the bulk unit cell, is 0.6 and 1.7 C/m^2 for SnS and GeSe, respectively, which is comparable to that of 3D ferroelectrics [91].

In this case, application of an electric field with polarity opposed to the bond dipole results in bonds breaking and creates new bonds with inversion of the polarization along $\hat{x}$, rather than in a rotation of the structure. As shown in Fig. 3.3 (a) the ionic configuration changes (i.e., $\hat{d}_{\text{puck}}$ switches from $\hat{x}$ to $-\hat{x}$), and it is apparent from Eq. 3.1 that the electric dipole orientation can be switched, which we have found to be the case based on our DFT calculations.

The coercive field for this puckering transformation is 0.18×10^7 V/cm for SnS and 0.51×10^7 V/cm for GeSe. Moreover, we found that applying an electric field in $\hat{y}$ at 0.29×10^7 V/cm (0.80×10^7 V/cm) could also convert the $\hat{d}_{\text{puck}}$ from $\hat{x}$ to $\hat{y}$ for SnS (GeSe). The coercive field calculated by this method corresponds to the electric field at which the unfavorable phase becomes unstable and can be seen as an upper bound for the coercive field of a real multi-domain material. This is usually smaller provided that the domain walls are mobile at that temperature and, according to a recent work [92], the domain wall energy is small for this class of materials. Thus, the electrical fields necessary for ferroelectric switching are clearly achievable in current 2D experiments [93]. The structures of SnS monolayer under electric fields at which the puckering orientation switches are plotted in Fig. 3.3.

Since the two materials possess a spontaneous, reversible polarization and bista-

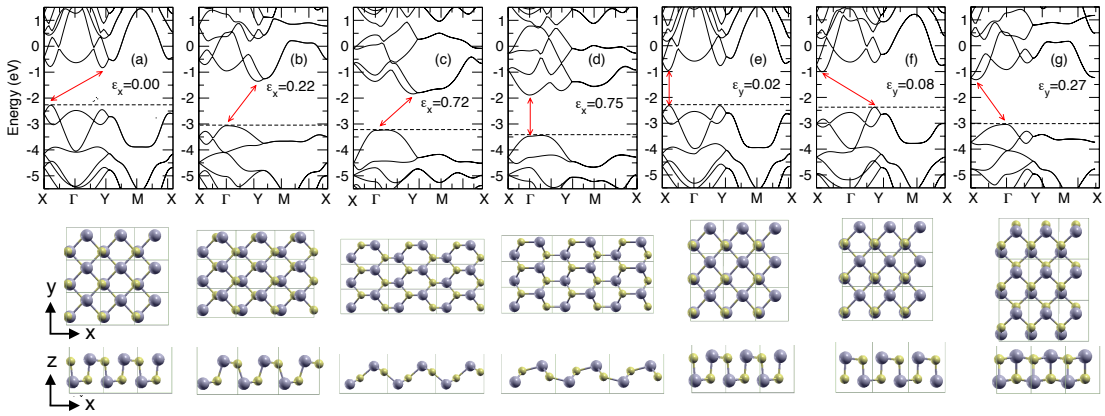

Figure 3.4: Representative band structures of SnS monolayers (a) unstrained, (b) to (d) under tensile uniaxial stress along the $\hat{x}$ for axial strains of $\epsilon_x = 0.22$ to $\epsilon_x = 0.75$, and (e) to (g) under tensile uniaxial stress along $\hat{y}$ for axial strains of $\epsilon_y = 0.02$ to $\epsilon_y = 0.27$. The dotted lines locate the valence band maxima. The corresponding side and top view of structural visualizations are below the band structure plots. It is apparent that the band structure (b) $\epsilon_x = 0.22$ (or an uniaxial stress of $\sigma_{xx} \sim 1.4$GPa) is equivalent to the band structure (g) $\epsilon_y = 0.27$ (or an uniaxial stress of $\sigma_{yy} \sim 1.4$GPa) if the $\hat{x}$ and $\hat{y}$ are inverted (rotation around Γ axis on figures).

bility, they classify as ferroelectrics. The configuration-coordinate diagram of GeSe is typical of a ferroelectric with second-order phase transition at $T = 0$ (consistent with the change in symmetry). The energy curve for SnS has a minimum rather than a saddle point at *Cmcm*-ML, and therefore resembles a ferroelectric with first order phase transition, with the peculiarity that the *Cmcm*-ML structure is stable for all $T > 0$. Recently, based on Car-Parrinello molecular dynamics simulations, Mehboudi et al. showed that monolayer monochalcogenides undergo an order-disorder phase transition [88]. Hence, since SnS and GeSe have four degenerate *Pnma*-ML phases, we expect that the average total polarization goes to zero as temperature approaches T_{m}.

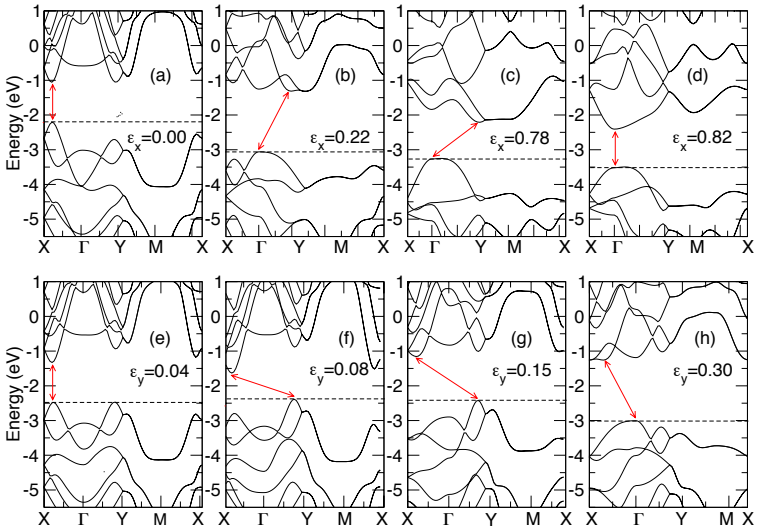

Figure 3.5: Evolution of GeSe band structure with strains in armchair (a) to (d) and zigzag direction (e) to (h). The dotted lines locate the valence band maxima. The structure inversion is found at $\epsilon_y = 0.15$. It is apparent that the band structure (b) $\epsilon_x = 0.22$ (or an uniaxial stress of $\sigma_{xx} \sim 1.4$GPa) is equivalent to the band structure (h) $\epsilon_y = 0.30$ (or an uniaxial stress of $\sigma_{yy} \sim 1.4$GPa) if the $\hat{x}$ and $\hat{y}$ are inverted (rotation around Γ axis on figures).

3.3.4 Band Structure

The phase transitions are accompanied by changes of the band structure and can, therefore, be detected optically. Representative SnS and GeSe band structures under uniaxial stress are shown in Fig. 3.4 and Fig. 3.5, respectively. We note that even though the band gap is underestimated due to our usage of DFT as the calculation method [79], the dispersion of the bands is accurately reproduced. Unstrained SnS is an indirect-gap semiconductor with its valence band maximum located near the X-point (along the Γ-X line) and the conduction band minimum near the Y-point (along the Γ-Y line). There are, therefore, two two-fold degenerate valleys, designated V_x and V_y, respectively. At large strains along $\hat{x}$, SnS transforms to a hexagonal phase at $\epsilon_x = 0.72$ resembling blue phosphorene (Fig. 3.4 (c)) [90] and becomes a direct

gap at $\epsilon_x = 0.75$. For uniaxial stress along $\hat{y}$ there is a transition from indirect gap to direct gap at $\epsilon_y = 0.02$ (see Fig. 3.4(e)), after which the system again becomes indirect gap.

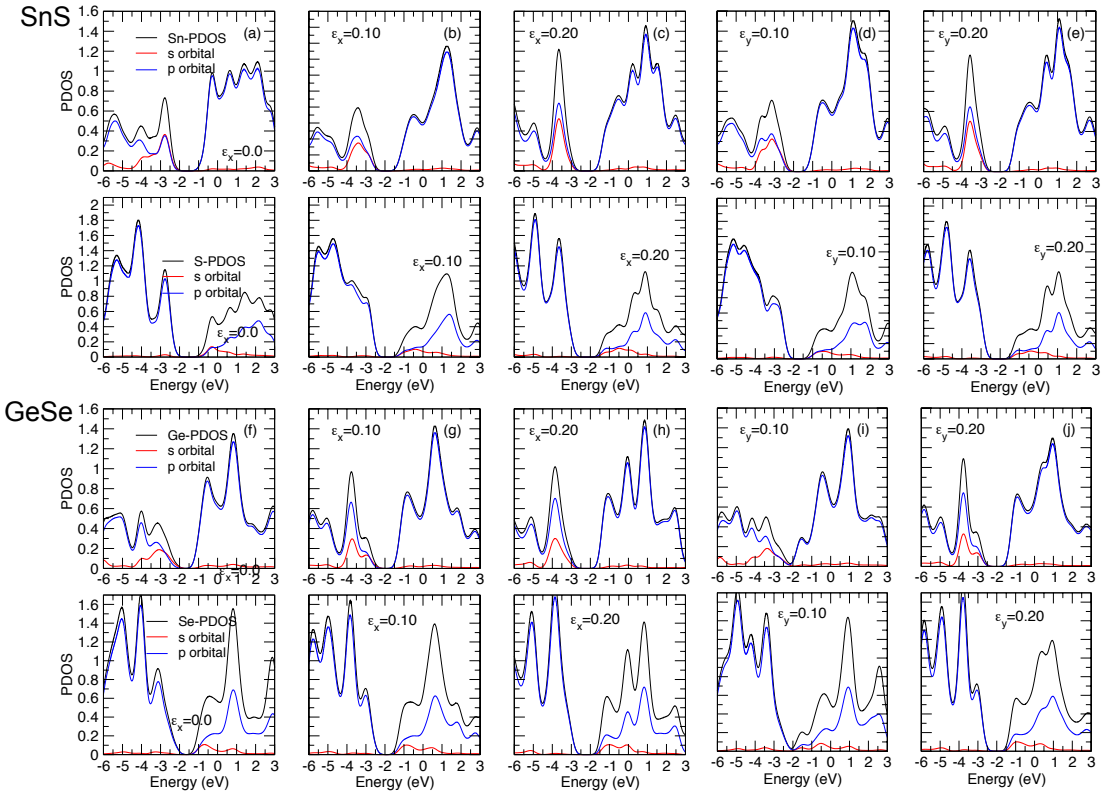

Figure 3.6: Projected density of states (PDOS) of SnS (a) to (e) and GeSe (f) to (j) for different strains. The top panels are PDOS of Sn (Ge) atom and the bottom panels are PDOS of S (Se) atom.

The band structure of GeSe under uniaxial stress is shown in Fig. 3.5 (a) to (d) for the $\hat{x}$ and (e) to (h) for the $\hat{y}$. Even though unstrained GeSe is a direct-gap semiconductor, there are also two nearly degenerate conduction band minima at the V_x and V_y points. The swapping between the $\hat{x}$ and $\hat{y}$ of the *Pnma*-ML structure under tensile stress along the $\hat{y}$ direction occurs at $\epsilon_y = 0.15$ and is in this case accompanied by a loss of the direct bandgap, which becomes indirect as the

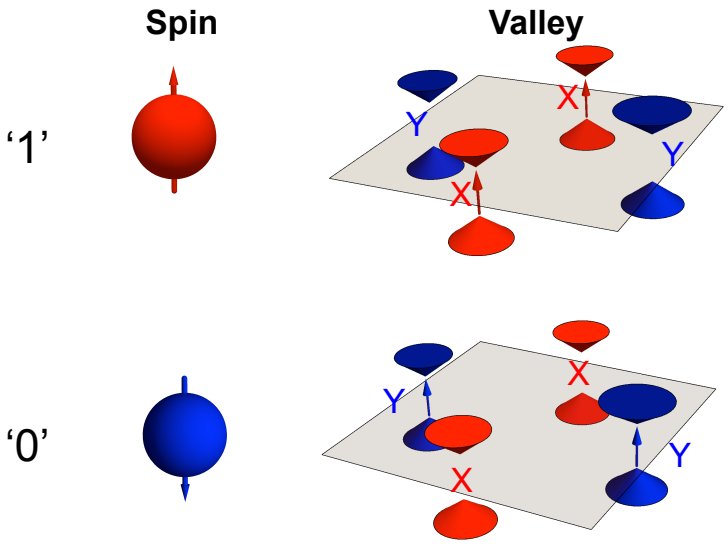

Figure 3.7: Schematic of valley polarization

structure reverts back into *Pnma*-ML.

As shown in Fig. 3.5, the band structure (b) $\epsilon_x = 0.22$ is equivalent to the band structure (h) $\epsilon_y = 0.30$ if the $\hat{x}$ and $\hat{y}$ are inverted (rotation around Γ axis on figures). The transition to a hexagonal phase under tensile stress along $\hat{x}$ ($\epsilon_x = 0.78$) is also accompanied by an indirect- to direct-gap semiconductor transition.

In addition, we calculated the projected density of states for SnS and GeSe for various strains (Fig. 3.6). The trends of the evolution of PDOS of GeSe and SnS with increasing strain are similar. Specifically, the relative contributions of the p-orbitals for Sn and Ge atoms at energies close to the maximum valence band increases with increasing strain.

3.3.5 Valley Selection Rules

Transition metal dichalcogenides (TMDCs) have been studied extensively and have shown potential for many technological applications ranging from photovoltaics to

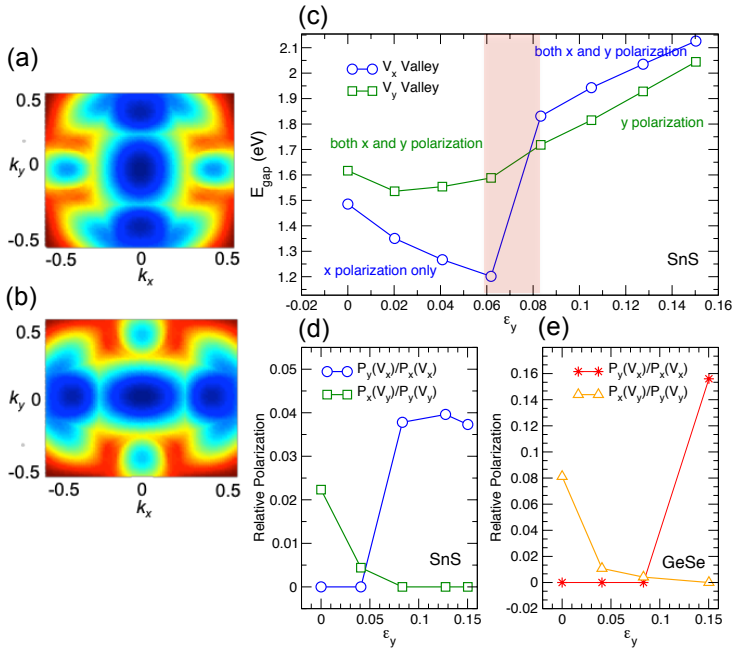

Figure 3.8: Band gap surfaces (a) $\epsilon_x = 0.22$ and (b) $\epsilon_y = 0.27$ demonstrate the valley swapping. (c) Evolution of the bandgap and (d, e) relative polarization under uniaxial stress along $\hat{y}$, highlighting the phase transition. Under small strain, the direct transition at V_x is only visible under incident x-polarized light, while the V_y transition is visible under both incident y and x (with a small coupling) polarized light.

valleytronic devices. Despite of the fast growth of generated data, currently at $\sim$ 2.5 quintillion bytes of data per day, there have been only few developments on applications of 2D materials for memory devices.

Analogous to spintronics, an emerging field called "valleytronics" attempts to store and manipulate information in semiconductors that possess multiple "valleys" (in momentum space). Before going further we will discuss how can we utilize valley degree of freedom in semiconductors to store bit of information. Supposed we have a semiconductor with four valleys located near the boundary of a rectangular Brillouin zone $\mathbf{k} = \{X, X', Y, Y'\} = \{[f\pi/a, 0], [-f\pi/a, 0], [0, f\pi/a], [0, -f\pi/a]\}$, where f is some number close to one. Further, suppose that the semiconductor has a gap on

the order of a few electron volt so that the electrons can be excited from the valence band to the conduction band. Mathematically, we can write the interband transition probability at a given vector $\mathbf{k}$ as [66, 94]

$$P_i(\mathbf{k}) \propto \left| \frac{m}{\hbar} \left\langle c(\mathbf{k}) \left| \frac{\partial H}{\partial k_i} \right| v(\mathbf{k}) \right\rangle \right|^2, \tag{3.2}$$

where i is the direction of the light polarization, $c(\mathbf{k})$ is the conduction band wave function, $v(\mathbf{k})$ is the valence band wave function, and H is the Hamiltonian. Alternatively, one can relate the transition probability to the dipole moment between the initial and the final bands: $\langle \mathbf{c}|\hat{p}_{x/y}|\mathbf{v}\rangle$, where the momentum direction corresponds to the light polarization. And supposed further that there is some selection rule such that we can *selectively* excite a certain valley using a light with a specific polarization. This approach is known as *selective valley polarization*. Similar to spin-up and spin-down, we can define '1' when the X valleys are occupied and '0' when the Y valleys are occupied. This mechanism is the basic approach to build a *valleytronic device*. The schematic of selective valley polarization is shown in fig. 3.7.

While this approach seems promising, the valleytronic property by itself cannot be utilized for non-volatile memory because of its transient nature as the relaxation time (inter-valley scattering time scale) is on the order of femtosecond. In this work, we propose to use group-IV monochalcogenides monolayers that are structurally bistable. Switching between two identical, but rotated states can be done mechanically by strain (or electrically by field) and optical readout of the state is based on valley selection rules.

The selection of valleys V_x or V_y can be achieved by at least two different optical methods: (i) using the fact that the direct gap is different at the two valley pairs; or (ii) using the optical selection rules. The direct transitions at the V_x and V_y valleys

have different energies, provided there is a means to identify the orientation of the crystal (Fig. 3.8). We plot the energy difference between valence and conduction band of SnS as functions of in plane wave vectors shown in Fig. 3.8 (a) and (b). It can be seen that the gap surface of $\epsilon_x = 0.22$ (Fig. 3.8 (a)) is equivalent to $\epsilon_y = 0.27$ (Fig. 3.8 (b)) but rotated 90°. It is evident that under uniaxial stress in $\hat{y}$ the bands have rotated in the Brillouin Zone, i.e. the V_y valley effectively becomes the V_x valley after passing the transition point of ϵ_y=0.08.

Using linearly polarized light to select the valleys V_x or V_y provides an additional method to detect the phase transition optically. For the transition to be allowed, the dipole moment must not vanish. It is possible to determine whether it is finite or not using the symmetry of the bands and the momentum. Since the dipole moment is computed by integrating the product of the initial and final wave functions, and the momentum, it is nonzero only if this product ($\propto \mathbf{c}^\dagger(\mathbf{r})\partial_{x/y}\mathbf{v}(\mathbf{r})$) is not odd with respect to any of the axes. In other words, the integrand must remain unchanged under every symmetry transformation of the space group characterizing the crystal.

We used our *ab initio* results to calculate the transition probabilities. For unstrained SnS, $\hat{y}$-polarized light populates only the V_y valleys, as there is no coupling between the valence and conduction band at V_x in the $\hat{y}$ direction (see Fig. 3.8 (d)). As shown by Ref. [94], the conduction band, valence band, and the p_x have a same irreducible representation. Consequently, the direct product of these quantities results in a non-vanishing transition probability coupling. On the other hand, $\hat{y}$-polarized light cannot excite V_x, as it possesses different representation. $\hat{x}$-polarized light can populate both V_x and V_y but it populates predominantly the V_x valleys, with $P_x(V_x)/P_x(V_y) \sim 40$. Similar behavior is observed in GeSe with a smaller selective valley polarization ratio. For instance, with linearly $\hat{x}$-polarized light the selective

valley polarization ratio was found to be $P_x(V_x)/P_x(V_y) \sim 15$.

The evolution of local gap V_x and V_y of SnS under stress in the $\hat{y}$ direction is shown in Fig. 3.8(c). We see that there is an abrupt change in V_y gap near the transition point $\epsilon_y = 0.08$. We also plot the relative polarization $P_y(V_x)/P_x(V_x)$ and $P_x(V_y)/P_y(V_y)$ as a function of axial strain ϵ_y, shown in Fig. 3.8(d) and (e) for SnS and GeSe, respectively. As we discussed earlier, $\hat{x}$-polarized light populates predominantly the V_x valleys but there is still a small transition probability at V_y when $\hat{x}$-polarized light is used. The absorption threshold for $\hat{x}$-polarized light has an abrupt change near $\epsilon_y = 0.08$ ($\epsilon_y = 0.15$ for GeSe), when the phase transition takes place. However, the absorption edge for $\hat{y}$-polarized light changes smoothly.

Before the transition point, the structure has a mirror symmetry inverting $\hat{y}$, and the V_y valleys can be populated using polarized light along $\hat{y}$ and $\hat{x}$ (the latter with a very small coupling). However, after the transition point, the puckering direction is rotated to be in the $\hat{y}$, and the reflection symmetry in $\hat{y}$ is broken, whereas a reflection symmetry emerges in $\hat{x}$. As a result, V_x can be excited by both $\hat{x}$ and $\hat{y}$ polarized light after the transition takes place. We have therefore demonstrated how optical transitions can be used to detect the orientation of the structure which determines valley configurations.

3.4 Summary

In summary, we have used first-principles calculations to demonstrate the potential of group-IV monochalcogenide monolayers as functional materials for information storage. This strategy, demonstrated using SnS and GeSe as prototypes, relies on the metastability and the possibility of switching the polarization direction using stress or electric field, creating a binary memory device. Comparing these prototype

materials, SnS differs from GeSe because it has a stable centrosymmetric phase which, at $T = 0$, is close in energy to the $Pnma$-ML phase.

Due to their peculiar band structures, both SnS and GeSe could in principle be used as functional materials for memory devices that can easily be interfaced with valleytronics logic. Valleytronics is based on the concept that the valley index can potentially be used to store information for subsequent logic operations, equivalent to spin in spintronics. However, in most valleytronics materials the information can be considered non-volatile only up to the timescale defined by inter-valley scattering processes, which are ubiquitous in real materials. Structural changes, used to store information in phase change memory devices, take place on a timescale orders of magnitude longer. Materials such as SnS and GeSe can be used to convert information stored as structural phase into information stored as valley index. One possibility is for example by using near-bandgap light that excites only the pair of valleys corresponding to the lowest energy exciton. The subsequent electronic state will have electron-hole pairs with momentum $(\pm k_x, 0)$ or $(0, \pm k_y)$, depending on the structure orientation. This valley state can be transmitted onto a valley-filter [95]. Alternatively, if coupled to a polarized light detector, the polarization switching can be detected optically taking advantage of valley-dependent direction of the linear polarization of the luminescence [94].

Chapter 4

Tight-binding Formalism

As we discussed earlier in Chapter 1, studies of materials based on density functional theory (DFT) approach are limited to small systems, usually around a few hundreds of atoms. Classical molecular dynamics (MD) is another method that can efficiently simulate thousands to millions of atoms. The MD method however does not calculate electronic properties such as band structure. Thus, development of a tight-binding model is needed to "bridge" the MD and the electronic properties. TB can capture the important physics (e.g. band structure near the Fermi level) based solely on atomic configurations, which can be obtained from the MD simulations.

In this chapter, we present some basic principles to develop a tight-binding (TB) model for monolayers. Specifically, we build a TB model for two atoms on a square lattice. Spin-orbit interactions (SOI) are included as we are interested in the studies of monolayers with strong SOI. In addition, we will also derive some properties of the material under external fields, such as in-plane magnetic field.

The work presented in this chapter (with some modifications) are parts of the following published papers:

- **P. Z. Hanakata**, A. S. Rodin, A. Carvalho, H. S. Park, D. K. Campbell, A. H. C. Neto,"Two-dimensional square buckled Rashba lead chalcogenides" *Physical Review B* 96 (16), 161401(R) (2017).

- **P. Z. Hanakata**, A. S. Rodin, H. S. Park, D. K. Campbell, A. H. C. Neto, "Strain-induced gauge and Rashba fields in ferroelectric Rashba lead chalcogenide monolayers PbX monolayers (X=S, Se, Te)" *Physical Review B* 97 (23), 235312 (2018). (2016).

- A. S. Rodin, **P. Z. Hanakata**, A. Carvalho, H. S. Park, D. K. Campbell, A. H. C. Neto,
"Rashba-like dispersion in buckled square lattices," *Physical Review B* 96 (11), 115450 (2016).

4.1 Introduction

Lead chalcogenide PbX (X=S, Se, Te) consists of two atoms per unit cell, denoted by A and B atoms, respectively. Lead is a heavy atom (Z(Pb)=82), and it is crucial for creating large spin-orbit interaction (SOI). The schematic top and side views of a buckled AB lattice and the Brillouin zone are shown in fig. 4.1(a). $\boldsymbol{a}$ is the unit lattice vector and $\boldsymbol{\delta}_j$ is the vector connecting atom i and its j neighbor. We denote the relaxed bond length between the neighboring A and B atoms by d, the vector connecting A and B atoms in the $(0,0)$ unit cell $\boldsymbol{\delta}_1 = d(\alpha, \alpha, -\gamma)$ where $\alpha = \frac{\cos\theta}{\sqrt{2}}$, $\gamma = \sin\theta$, and θ is the buckling angle (with $\theta = 0$ corresponding to a flat lattice).

From DFT calculations we found that the bands near the Fermi level are mostly composed of s and p orbitals from both A and B atoms [35]. In this work we will include first nearest neighbors interaction and SOI. For the two atom AB unit cell shown in Fig. 8.1(a), the relevant orbital basis involves $\{s^A, p_x^A, p_y^A, p_z^A, s^B, p_x^B, p_y^B, p_z^B\}$. As we include the SOI, we will write our Hamiltonian in angular momentum basis. The dimension of the total Hilbert space is 16×16 with new basis of $|\mu\rangle \rightarrow |m\rangle|m_{\text{orb}}\rangle|s\rangle$, where $m = \{|A\rangle, |B\rangle\}$ is the sublattice degree of freedom, $m_{\text{orb}} =$

$\{|0,0\rangle, |1,1\rangle, |1,-1\rangle, |1,0\rangle\}$ is the orbital angular momentum degree of freedom, and $s = \{(|+\rangle, |-\rangle\}$ is the spin degree of freedom.

4.2 Tight-binding Model

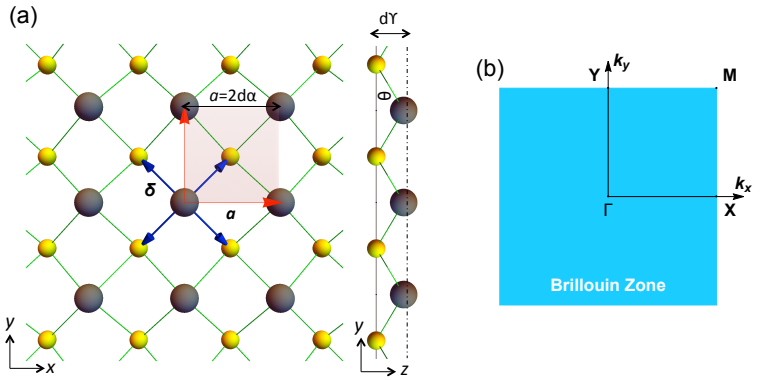

Figure 4.1: (a) Schematic top and side view of PbX and the corresponding Brillouin zone.

The lead chalcogenide monolayer has two atoms per unit cell (A, B). The wave function of sublattice A then can be written as

$$\psi^A(r) = \frac{1}{\sqrt{N}} \sum_{\mathbf{k},\mu} e^{i\mathbf{k}\cdot\mathbf{R}} a_{\mu,\mathbf{k}} \phi_\mu(\mathbf{r} - \mathbf{R}), \tag{4.1}$$

where $\mathbf{R}$ is the lattice vector, $\mathbf{k}$ is a wave vector, μ is the basis wave function $[s, p_x, p_y, p_z]$. Including only nearest neighbor hopping the spinless Hamiltonian can be written as

$$H_{\text{orb}} = \sum_{\mu,\nu} \sum_{i,j} [t_{ij,\mu\nu} c^\dagger_{i,\mu} c_{j,\nu} + h.c] + \sum_{\mu,\nu} \sum_i E_{\mu\nu} c^\dagger_{i,\mu} c_{i,\nu}, \tag{4.2}$$

where $\langle i, j\rangle$ runs over the onsite cell and the nearest neighboring cells. $c^\dagger_{i,\mu}$ creates an electron in the unit cell i with atomic orbital μ. We can write this more compactly

as

$$H_{\text{orb}} = \begin{pmatrix} H_{AA} & H_{AB} \\ H_{AB}^{\dagger} & H_{BB} \end{pmatrix} , \tag{4.3}$$

where H_{AA} (the onsite term) is given by

$$H_{AA} = \begin{pmatrix} E_A^s & 0 & 0 & 0 \\ 0 & E_A^{p_x} & 0 & 0 \\ 0 & 0 & E_A^{p_y} & 0 \\ 0 & 0 & 0 & E_A^{p_z} \end{pmatrix} . \tag{4.4}$$

To write down the hopping matrix, we use the following Slater-Koster matrix elements for the orbitals of neighboring atoms [96]:

$$\begin{aligned} &s\text{-}s : V_{ss\sigma} , \\ &s\text{-}p : V_{sp\sigma} \hat{d} \cdot \hat{o}_j , \\ &p\text{-}p : (\hat{o}_i \cdot \hat{o}_j) V_{pp\pi} + \left(\hat{o}_i \cdot \hat{d}\right) \left(\hat{o}_j \cdot \hat{d}\right) (V_{pp\sigma} - V_{pp\pi}) . \end{aligned} \tag{4.5}$$

Here, $\hat{o}_i$ is the orientation of the ith orbital and $\hat{d}$ is the unit vector pointing from atom 1 to atom 2. If we include up to first nearest neighbors only we can write the inter-lattice hopping matrix $H_{AB} \equiv K$ as

$$K = \Theta_\Gamma \begin{pmatrix} V_{ss\sigma} & 0 & 0 & -\gamma V_{sp\sigma}^{(1)} \\ 0 & V_{pp\pi} + \alpha^2 \Delta & 0 & 0 \\ 0 & 0 & V_{pp\pi} + \alpha^2 \Delta & 0 \\ \gamma V_{sp\sigma}^{(2)} & 0 & 0 & V_{pp\pi} + \gamma^2 \Delta \end{pmatrix} + 4\alpha^2 \Delta \Theta_M \begin{pmatrix} 0 & 0 & 0 & 0 \\ 0 & 0 & 1 & 0 \\ 0 & 1 & 0 & 0 \\ 0 & 0 & 0 & 0 \end{pmatrix}$$

$$+ 4\alpha\Theta_X \begin{pmatrix} 0 & iV^{(1)}_{sp\sigma} & 0 & 0 \\ -iV^{(2)}_{sp\sigma} & 0 & 0 & -i\gamma\Delta \\ 0 & 0 & 0 & 0 \\ 0 & -i\gamma\Delta & 0 & 0 \end{pmatrix} + 4\alpha\Theta_Y \begin{pmatrix} 0 & 0 & iV^{(1)}_{sp\sigma} & 0 \\ 0 & 0 & 0 & 0 \\ -iV^{(2)}_{sp\sigma} & 0 & 0 & -i\gamma\Delta \\ 0 & 0 & -i\gamma\Delta & 0 \end{pmatrix} . \quad (4.6)$$

where

$$\begin{aligned} \Theta_\Gamma &= \cos\frac{k_x a}{2}\cos\frac{k_y a}{2} \\ \Theta_M &= \sin\frac{k_x a}{2}\sin\frac{k_y a}{2} \\ \Theta_X &= \sin\frac{k_x a}{2}\cos\frac{k_y a}{2} \\ \Theta_Y &= \sin\frac{k_y a}{2}\cos\frac{k_x a}{2} . \end{aligned}$$

The momentum $\pi/a \leq k_{x/y} \leq \pi/a$ and $\gamma = \sin\theta$. We see that Θ is dictated by crystal symmetry. $\Theta_{k^{\text{simmetry}}}$ equals to one if $\mathbf{k} = \mathbf{k}^{\text{simmetry}}$. To keep the expression more compact, we have introduced $\Delta = V_{pp\sigma} - V_{pp\pi}$. In addition, since the A and B species are not necessarily the same, we have two quantities of the $V_{sp\sigma}$ form.

While it is convenient to use s and p orbitals to write down the hopping matrix, since we are interested in including SOI in our model, it is helpful to go to a basis which is more natural for the angular momentum operators:

$$|0,0\rangle = |s\rangle\,, \quad |1,\pm1\rangle = \frac{\mp|p_x\rangle - i|p_y\rangle}{\sqrt{2}}\,, \quad |1,0\rangle = |p_z\rangle\,, \quad (4.7)$$

where the first number represents the orbital momentum quantum number and the second one is its projection along the $\hat{z}$ direction. This basis change does not alter the H_{AA} and H_{BB} matrices. The inter-lattice hopping portion of the Hamiltonian,

on the other hand, becomes

$$\bar{K} = \Theta_\Gamma \underbrace{\begin{pmatrix} V_{ss\sigma} & 0 & 0 & -\gamma V^{(1)}_{sp\sigma} \\ 0 & V_{pp\pi}+\alpha^2\Delta & 0 & 0 \\ 0 & 0 & V_{pp\pi}+\alpha^2\Delta & 0 \\ \gamma V^{(2)}_{sp\sigma} & 0 & 0 & V_{pp\pi}+\gamma^2\Delta \end{pmatrix}}_{K_\Gamma} + 4\alpha^2\Delta\Theta_M \underbrace{\begin{pmatrix} 0 & 0 & 0 & 0 \\ 0 & 0 & -i & 0 \\ 0 & i & 0 & 0 \\ 0 & 0 & 0 & 0 \end{pmatrix}}_{K_M} +$$
$$+ 2\sqrt{2}\alpha\Theta_X \underbrace{\begin{pmatrix} 0 & -iV^{(1)}_{sp\sigma} & iV^{(1)}_{sp\sigma} & 0 \\ iV^{(2)}_{sp\sigma} & 0 & 0 & i\gamma\Delta \\ -iV^{(2)}_{sp\sigma} & 0 & 0 & -i\gamma\Delta \\ 0 & i\gamma\Delta & -i\gamma\Delta & 0 \end{pmatrix}}_{K_X} + 2\sqrt{2}\alpha\Theta_Y \underbrace{\begin{pmatrix} 0 & V^{(1)}_{sp\sigma} & V^{(1)}_{sp\sigma} & 0 \\ V^{(2)}_{sp\sigma} & 0 & 0 & \gamma\Delta \\ V^{(2)}_{sp\sigma} & 0 & 0 & \gamma\Delta \\ 0 & -\gamma\Delta & -\gamma\Delta & 0 \end{pmatrix}}_{K_Y} . \tag{4.8}$$

From here we write $H \equiv UH_{\rm orb}U^{-1}$, where U is a matrix projector from the orbital basis to the angular momentum basis.

4.3 Spin-orbit Interaction

To include the SOI, we use the standard form describing the spin-orbit coupling arising from the interaction with the nucleus:

$$H_{\rm SOI} = T_{\mathcal{X}} \left(\frac{L_+ \otimes s_- + L_- \otimes s_+}{2} + L_z \otimes s_z \right) , \tag{4.9}$$

where $\mathcal{X}$ is either Pb or X (X=S, Se, Te). The last term modifies the diagonal elements of the self-energy for $|1,\pm1\rangle$ by adding (subtracting) $T_{\rm X}/2$ if L_z and s_z point in the same (opposite) direction. The first tem couples $|1,1\rangle \otimes |\downarrow\rangle$ with $|1,0\rangle \otimes |\uparrow\rangle$ and $|1,-1\rangle \otimes |\uparrow\rangle$ with $|1,0\rangle \otimes |\downarrow\rangle$ with the coupling strength $T_{\rm X}/\sqrt{2}$.

The total Hamiltonian can then be written as

$$H_{\text{tot}} = H \otimes 1_{2x2} + H_{\text{SOI}} \tag{4.10}$$

4.3.1 Energy Splitting in Free Electron Model

Before going to see the effects of buckling (symmetry breaking) and SOI on the band structure, we will review some basics of energy splitting. Kramers theorem states that if time-reversal symmetry is not broken then all eigenstates are at least doubly degenerate. We will denote $\mathcal{T}$ as the time-reversal transformation and $\mathcal{R}$ as the spatial-inversion transformation. By time-reversal symmetry, $t \to -t$ and $\mathbf{k} \to \mathbf{k}$. This implies that $\mathcal{T} : E_s(\mathbf{k}) = E_{-s}(-\mathbf{k})$, where E is the eigen energy and s is the spin. If SOI does not present then $E(\mathbf{k}) = E(-\mathbf{k})$, regardless of the inversion symmetry. For a centrosymmetric crystal we have

$$\mathcal{T} : E_s(\mathbf{k}) = E_{-s}(-\mathbf{k}) \tag{4.11}$$

$$\mathcal{R} : E_{-s}(-\mathbf{k}) = E_{-s}(\mathbf{k}) \tag{4.12}$$

$$\implies E_s(\mathbf{k}) = E_{-s}(\mathbf{k}). \tag{4.13}$$

If a crystal is not centrosymmetric then $E_s(\mathbf{k}) \neq E_{-s}(\mathbf{k})$. Energy splitting can occur in a non-centrosymmetric material at zero magnetic field. From this symmetry analysis we expect that the out-of-plane buckling will play an important role in splitting the energy. Another way to understand energy splitting is to consider 2D free-electron gas under external fields. Without any external field, the energy should be degenerate for all $\mathbf{k}$ and the energy dispersion is quadratic. As we break the time-reversal symmetry by applying an out-of-plane magnetic field $\boldsymbol{\mathcal{B}}$, the energies are no longer degenerate at each $\mathbf{k}$. The energy splitting is constant and proportional to the

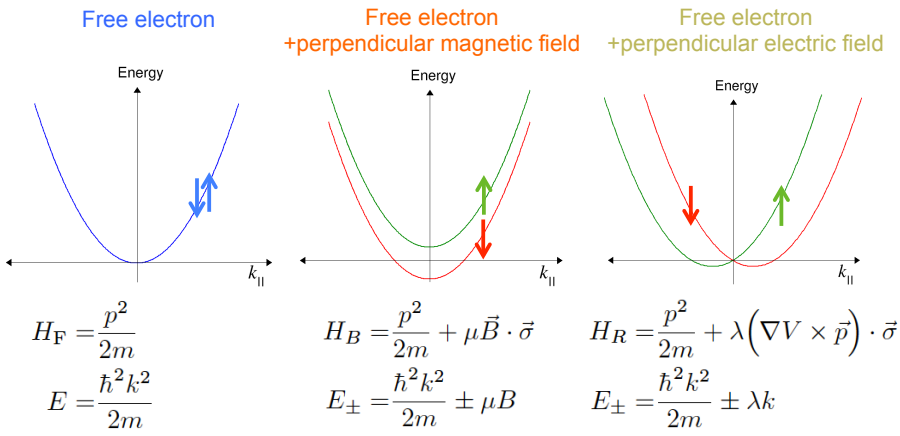

Figure 4.2: Band energy of 2D free-electron gas in without any external field, with out-of-plane magnetic field, and with out-of-plane electric field.

strength of the applied magnetic field $E_{\pm} = \hbar \frac{\hbar^2 k^2}{2m} \pm \mu \mathcal{B}_{\perp}$, where μ is the magnetic moment. Spins are polarized in the direction of the magnetic field and this energy splitting is known as the Zeeman splitting.

Electron moving in a electric field will experience an effective magnetic field $\mathbf{k} \times \boldsymbol{\mathcal{E}}_{\text{field}}$ in its rest-frame. In solids, the electric field is given by $\boldsymbol{\mathcal{E}}_{\text{field}} = \nabla V$, where V is the crystal potential. For simplicity we will consider a constant out-of-plane electric field. This electric field does not break the time-reversal symmetry, however it does break the inversion symmetry. The energies are no longer degenerate except at the protected time-reversal point ($\mathbf{k} = \mathbf{0}$). This simple picture is often used to describe Rashba effects in solids, especially in surfaces and interfaces between different materials [97]. The Hamiltonian, known as Rashba Hamiltonian, can be written as,

$$\begin{aligned} H_R =& \frac{p^2}{2m} 1_{2\times 2} + \lambda (\nabla V \times \boldsymbol{p}) \cdot \vec{\sigma} \\ =& \frac{p^2}{2m} 1_{2\times 2} + \lambda (\sigma_y p_x - \sigma_x p_y) \,. \end{aligned} \tag{4.14}$$

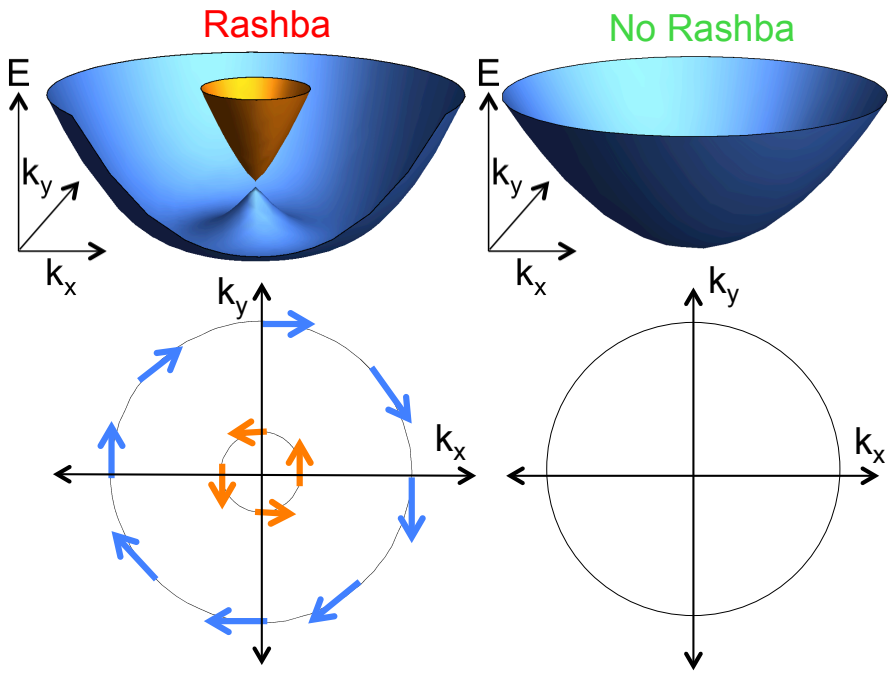

Figure 4.3: Rashba splitting and spin-polarization.

The eigen energy is given by $E_{\pm} = \frac{\hbar^2 k^2}{2m} \pm \lambda k$ and k is the in-plane momentum. We can obtain the spin-polarization by taking the expectation of the spinors $\vec{\sigma}$ with respect to the eigenstates $\psi_{\rm I}\rangle$ and $\psi_{\rm II}\rangle$. Unlike the Zeeman splitting, electrons are spin-polarized in clockwise and anti-clockwise directions. The ratio between energy splitting and the momentum shift is known as the Rashba coupling $\lambda = 2E_{\rm Rashba}/k_R$ and the spin-texture is given by

$$\langle\psi_{\rm I,II}|\hat{\sigma}|\psi_{\rm I,II}\rangle = \pm\frac{|\lambda|}{\lambda}(\sin\phi, -\cos\phi, 0) \tag{4.15}$$

The schematics of the spin-splitting due to external fields are shown in fig. 4.2. Figure 4.3 shows the Rashba splitting in a 3D plot and the spin-polarizations. These simple pictures of applying external fields to 2D electron gas give some qualitative

understanding on spin-splitting in solids. This approach however is is only phenomenological. A tight-model approximation should be carried to get a more realistic description of the energy splitting in solids [97]. In the next section, we will show that from a tight-binding framework we will obtain a Hamiltonian that resembles the Rashba Hamiltonian.

4.3.2 M Point

We first look around the M point $k_x = k_y = \pi/a$. To the leading order in q, the hopping matrix $\tilde{K}$ is given by,

$$\tilde{K} = 4\alpha^2\Delta \begin{pmatrix} 0 & 0 & 0 & 0 \\ 0 & 0 & -i & 0 \\ 0 & i & 0 & 0 \\ 0 & 0 & 0 & 0 \end{pmatrix} - a\sqrt{2}\alpha q \begin{pmatrix} 0 & V^{(1)}_{sp\sigma}e^{-i\phi} & V^{(1)}_{sp\sigma}e^{i\phi} & 0 \\ V^{(2)}_{sp\sigma}e^{i\phi} & 0 & 0 & \gamma\Delta e^{i\phi} \\ V^{(2)}_{sp\sigma}e^{-i\phi} & 0 & 0 & \gamma\Delta e^{-i\phi} \\ 0 & -\gamma\Delta e^{-i\phi} & -\gamma\Delta e^{i\phi} & 0 \end{pmatrix}, \tag{4.16}$$

where ϕ is the angle measured from the $\hat{x}$ direction. At $q = 0$ ($k_x = k_y = \pi/a$), the Hamiltonian decomposes into several uncoupled blocks with the corresponding bases:

$$\begin{aligned} H_s^{m,\pm} &= E_m^s : |0,0\rangle \otimes |\pm\rangle \otimes |m\rangle\,, \\ H_p^{mn,\pm} &= \begin{pmatrix} E_m^p - \frac{T_m}{2} & \frac{T_m}{\sqrt{2}} & \mp 4i\alpha^2\Delta \\ \frac{T_m}{\sqrt{2}} & E_m^p & 0 \\ \pm 4i\alpha^2\Delta & 0 & E_n^p + \frac{T_n}{2} \end{pmatrix} : \begin{pmatrix} |m\rangle \otimes |1,\pm 1\rangle \otimes |\mp\rangle \\ |m\rangle \otimes |1,0\rangle \otimes |\pm\rangle \\ |n\rangle \otimes |1,\mp 1\rangle \otimes |\mp\rangle \end{pmatrix}, \end{aligned} \tag{4.17}$$

where $m \neq n$ labels the sublattices and the middle $|\pm\rangle$ ket denotes the spin state. Using the direct sum notation, we can write down the total Hamiltonian as $H = H_s^{A,+} \oplus H_s^{A,-} \oplus H_s^{B,+} \oplus H_s^{B,-} \oplus H_p^{AB,+} \oplus H_p^{AB,-} \oplus H_p^{BA,+} \oplus H_p^{BA,-}$.

From H_s, we see that for a given m, the eigenstates are spin-degenerate. The degeneracy becomes four-fold if the atoms of sublattices A and B are the same, leading to $E_A^p = E_B^p$. Equation (4.16) shows that at finite q there is no coupling between the degenerate $|0,0\rangle$ states that is linear in momentum. This means that the bands composed of s orbitals have local extrema at the M point.

Next, we turn to H_p from Eq. (4.17). Just like for H_s, the bands are doubly or four-fold degenerate depending on whether the sublattices are composed of the same atomic species. Without making assumptions about the lattice composition, the general form of the degenerate states is

$$\begin{aligned} |\Psi^{\pm}\rangle_{mn} = c_0|m\rangle \otimes |1,\pm 1\rangle \otimes |\mp\rangle + c_1|m\rangle \otimes |1,0\rangle \otimes |\pm\rangle \\ \pm i c_2|n\rangle \otimes |1,\mp 1\rangle \otimes |\mp\rangle \,, \end{aligned} \tag{4.18}$$

with c_0, c_1, and c_2 real. At finite q,

$$_{mn}\langle\Psi^{+}|H|\Psi^{-}\rangle_{mn} = -a \sin 2\theta c_1 c_2 \left(\Delta i q e^{-i\phi}\right) \varepsilon_{mn} \,, \tag{4.19}$$

where $\varepsilon_{\mathrm{AB}} = -\varepsilon_{\mathrm{BA}} = 1$ is the two-dimensional Levi-Civita symbol. This coupling between the degenerate states leads to an effective Rashba-like Hamiltonian:

$$H_{\mathrm{eff}}^{mn} = a \sin 2\theta c_1 c_2 \Delta \varepsilon_{mn} \left[(\mathbf{q} \times \boldsymbol{\sigma}) \cdot \hat{z}\right] : \begin{pmatrix} |\Psi^{+}\rangle_{mn} \\ |\Psi^{-}\rangle_{mn} \end{pmatrix} ., \tag{4.20}$$

or in the matrix form

$$H_{\text{eff}} = \begin{pmatrix} 0 & -i\lambda(q_x - iq_y) \\ i\lambda(q_x + iq_y) & 0 \end{pmatrix}, \tag{4.21}$$

We use values of c_0, c_1, and c_2 obtained from DFT results. To give better physical pictures of these coefficients, we will solve the Hamiltonian Eq. 4.17. We treat the spin orbit interaction (SOI) as perturbations and we will assume that $T_m \gg T_n$ where m is the index denoting Pb with strong SOI and n denotes weak SOI of chalcogen atom. Focusing on $H_p^{mn,+}$, Eq. 4.17 becomes

$$H_p^{mn,+} = \begin{pmatrix} E_m^p & 0 & -4i\alpha^2\Delta \\ 0 & E_m^p & 0 \\ 4i\alpha^2\Delta & 0 & E_n^p \end{pmatrix} : \begin{pmatrix} |m\rangle \otimes |1,1\rangle \otimes |-\rangle \\ |m\rangle \otimes |1,0\rangle \otimes |+\rangle \\ |n\rangle \otimes |1,-1\rangle \otimes |-\rangle \end{pmatrix}, \tag{4.22}$$

and the perturbation

$$\delta H_p^{mn,+} = \begin{pmatrix} -\frac{T_m}{2} & \frac{T_m}{\sqrt{2}} & 0 \\ \frac{T_m}{\sqrt{2}} & 0 & 0 \\ 0 & 0 & 0 \end{pmatrix} : \begin{pmatrix} |m\rangle \otimes |1,1\rangle \otimes |-\rangle \\ |m\rangle \otimes |1,0\rangle \otimes |+\rangle \\ |n\rangle \otimes |1,-1\rangle \otimes |-\rangle \end{pmatrix}. \tag{4.23}$$

We first solved Eq. 4.22 to find the eigenvalues and eigenvectors and used first order perturbation theory to obtain the corrections to the eigenvectors. Using MATHEMATICA, we found to the first order in T_m that

$$|c_1 c_2| \simeq \frac{T_m(E_m^p - E_n^p + \sqrt{(E_m^p - E_n^p)^2 + 64\alpha^4\Delta^2})}{8\sqrt{2}\alpha^2\Delta(E_n^p - E_m^p + \sqrt{(E_m^p - E_n^p)^2 + 64\alpha^4\Delta^2})}. \tag{4.24}$$

Recall that we defined Rashba parameter $\lambda \equiv a \sin 2\theta \Delta c_1 c_2$. From Eq. 4.24 we see that $|c_1 c_2|$ weakly depends on strains. For this reason, in the main text we assumed

c_1 and c_2 are constant and the corrections to λ come mostly from Δ and θ.

4.3.3 Γ Point

Next, we move to the Γ point at the center of the Brillouin zone. Unlike the M point, the Rashba-like dispersion appears only for heterogeneous lattices. Moreover, because of the band composition and the required coupling between different orbitals, the splitting here will generally be weaker than at the M point.

As before, we start by obtaining the simplified effective Hamiltonian. Here, $\tilde{K}$ does not undergo such a drastic simplification as at the corner of the Brillouin zone:

$$\tilde{K} = 4\begin{pmatrix} V_{ss\sigma} & 0 & 0 & -\gamma V^{(1)}_{sp\sigma} \\ 0 & V_{pp\pi}+\alpha^2\Delta & 0 & 0 \\ 0 & 0 & V_{pp\pi}+\alpha^2\Delta & 0 \\ \gamma V^{(2)}_{sp\sigma} & 0 & 0 & V_{pp\pi}+\gamma^2\Delta \end{pmatrix} - 2\sqrt{2}i\alpha q \begin{pmatrix} 0 & V^{(1)}_{sp\sigma}e^{i\phi} & -V^{(1)}_{sp\sigma}e^{-i\phi} & 0 \\ -V^{(2)}_{sp\sigma}e^{-i\phi} & 0 & 0 & -\gamma\Delta e^{-i\phi} \\ V^{(2)}_{sp\sigma}e^{i\phi} & 0 & 0 & \gamma\Delta e^{i\phi} \\ 0 & -\gamma\Delta e^{i\phi} & \gamma\Delta e^{-i\phi} & 0 \end{pmatrix}. \tag{4.25}$$

For $q = 0$, we get the following uncoupled Hamiltonian blocks:

$$H_1^{\pm} = \begin{pmatrix} E^s_m & 0 & 0 & 4V_{ss\sigma} & 0 & -4\gamma V^{(1)}_{sp\sigma} \\ 0 & E^p_m - \frac{T_m}{2} & \frac{T_m}{\sqrt{2}} & 0 & 4V_{pp\pi}+4\alpha^2\Delta & 0 \\ 0 & \frac{T_m}{\sqrt{2}} & E^p_m & 4\gamma V^{(2)}_{sp\sigma} & 0 & 4V_{pp\pi}+4\gamma^2\Delta \\ 4V_{ss\sigma} & 0 & 4\gamma V^{(2)}_{sp\sigma} & E^s_n & 0 & 0 \\ 0 & 4V_{pp\pi}+4\alpha^2\Delta & 0 & 0 & E^p_n - \frac{T_n}{2} & \frac{T_n}{\sqrt{2}} \\ -4\gamma V^{(1)}_{sp\sigma} & 0 & 4V_{pp\pi}+4\gamma^2\Delta & 0 & \frac{T_n}{\sqrt{2}} & E^p_n \end{pmatrix}. \tag{4.26}$$

$$\begin{pmatrix} |m\rangle \otimes |0,0\rangle \otimes |\pm\rangle \\ |m\rangle \otimes |1,\pm1\rangle \otimes |\mp\rangle \\ |m\rangle \otimes |1,0\rangle \otimes |\pm\rangle \\ |n\rangle \otimes |0,0\rangle \otimes |\pm\rangle \\ |n\rangle \otimes |1,\pm1\rangle \otimes |\mp\rangle \\ |n\rangle \otimes |1,0\rangle \otimes |\pm\rangle \end{pmatrix},$$

$$H_2^{\pm} = \begin{pmatrix} E_m^p + \frac{T_m}{2} & 4V_{pp\pi} + 4\alpha^2\Delta \\ 4V_{pp\pi} + 4\alpha^2\Delta & E_n^p + \frac{T_n}{2} \end{pmatrix} : \begin{pmatrix} |m\rangle \otimes |1,\pm1\rangle \otimes |\pm\rangle \\ |n\rangle \otimes |1,\pm1\rangle \otimes |\pm\rangle \end{pmatrix}. \tag{4.27}$$

Same as before, the blocks are doubly-degenerate. The total Hamiltonian can be written as $H = H_1^+ \oplus H_1^- \oplus H_2^+ \oplus H_2^-$. From Eq. (4.25), one can see that at finite k, only $L_z = 0$ and $L_z \neq 0$ are coupled. This means that the degenerate eigenstates of H_2 blocks remain uncoupled since they are composed exclusively of $L_z \neq 0$ states.

The case of H_2 is slightly more complicated. The general form of the degenerate wave functions is

$$\begin{aligned} |\Psi^{\pm}\rangle = {} & a_{\mathrm{A}}|m\rangle \otimes |0,0\rangle \otimes |\pm\rangle + b_{\mathrm{A}}|m\rangle \otimes |1,\pm1\rangle \otimes |\mp\rangle + \\ & + c_{\mathrm{A}}|m\rangle \otimes |1,0\rangle \otimes |\pm\rangle + a_{\mathrm{B}}|n\rangle \otimes |0,0\rangle \otimes |\pm\rangle + \\ & + b_{\mathrm{B}}|n\rangle \otimes |1,\pm1\rangle \otimes |\mp\rangle + c_{\mathrm{B}}|n\rangle \otimes |1,0\rangle \otimes |\pm\rangle\,. \end{aligned} \tag{4.28}$$

Similarly to the M point, here we get

$$\begin{aligned} & \langle\Psi^+|H|\Psi^-\rangle = 4\sqrt{2}i\alpha q e^{-i\phi} \times \\ & \left[a_{\mathrm{A}}b_{\mathrm{B}}V_{sp\sigma}^{(1)} + a_{\mathrm{B}}b_{\mathrm{A}}V_{sp\sigma}^{(2)} + \gamma\Delta\left(c_{\mathrm{B}}b_{\mathrm{A}} - c_{\mathrm{A}}b_{\mathrm{B}}\right)\right]. \end{aligned} \tag{4.29}$$

Despite being somewhat more elaborate compared to Eq. 4.20, Eq. 4.29 has the same form. The main difference between the two points of the Brillouin zone appears when the atoms of both sublattices are the same. In this case, $V_{sp\sigma}^{(1)} = V_{sp\sigma}^{(2)}$.

Additionally, $a_{\mathrm{A}} = -a_{\mathrm{B}}$, $b_{\mathrm{A}} = b_{\mathrm{B}}$, and $c_{\mathrm{A}} = c_{\mathrm{B}}$, leading to a vanishing matrix element in Eq. (4.29). Thus, unlike the M point, where having a lattice composed of a single atomic type eliminates the spin texture while preserving the linear dispersion, Rashba-like dispersion at the Γ point requires two different atomic species.

4.4 Magnetic Field

Let us now try to include external fields to the system. The magnetic field can be included via the Peierls substitution so that $\mathbf{q} \to \mathbf{q} - e\mathbf{A}/c$, where $\mathbf{A}$ is the vector potential. In addition, applying an external magnetic field leads to the interaction of the electron angular momentum with the field.

The total magnetic moment of an electron is given by

$$\mu = -\mu_B \frac{\mathbf{L} + 2\mathbf{S}}{\hbar}\,, \tag{4.30}$$

so that

$$\mathbf{B}\cdot\mu = -\mu_B \frac{B_x\left(\frac{L_+ + L_-}{2} + S_+ + S_-\right) + B_y\left(\frac{L_+ - L_-}{2i} + \frac{S_+ - S_-}{i}\right) + B_z\left(L_z + 2S_z\right)}{\hbar}\,. \tag{4.31}$$

Setting $\mathbf{B} = \left(B_\parallel \cos\tau, B_\parallel \sin\tau, B_\perp\right)$ gives

$$\begin{aligned}\mathbf{B}\cdot\mu =& -\mu_B \frac{B_\parallel \cos\tau\left(\frac{L_+ + L_-}{2} + S_+ + S_-\right) - iB_\parallel \sin\tau\left(\frac{L_+ - L_-}{2} + S_+ - S_-\right)}{\hbar} \\ &+ \frac{B_\perp\left(L_z + 2S_z\right)}{\hbar}\end{aligned} \tag{4.32}$$

$$= -\mu_B \frac{B_\parallel\left[e^{-i\tau}\left(\frac{L_+}{2} + S_+\right) + e^{i\tau}\left(\frac{L_-}{2} + S_-\right)\right] + B_\perp\left(L_z + 2S_z\right)}{\hbar}\,. \tag{4.33}$$

The first term $\propto B_{\parallel}$ introduces coupling between $|\Psi^{+/-}\rangle$ while the last term $\propto B_{\perp}$ modifies and breaks the symmetry between the degenerate states. Starting with last term, we get

$$\langle\Psi^{+}|\mathbf{B}\cdot\mu|\Psi^{+}\rangle = -\langle\Psi^{-}|\mathbf{B}\cdot\mu|\Psi^{-}\rangle = -\mu_B B_{\perp}\left(c_1^2 - 2c_2^2\right) . \tag{4.34}$$

Next, we apply the first term onto $|\Psi^{+}\rangle$:

$$\begin{aligned}
&-\mu_B \frac{B_{\parallel}\left[e^{-i\tau}\left(\frac{L_+}{2}+S_+\right)+e^{i\tau}\left(\frac{L_-}{2}+S_-\right)\right]}{\hbar}(c_0|m\rangle\otimes|1,1\rangle\otimes|-\rangle + c_1|m\rangle\otimes|1,0\rangle\otimes|+\rangle \\
&+ ic_2|n\rangle\otimes|1,-1\rangle\otimes|-\rangle) = \\
=&-\mu_B B_{\parallel}\Big[e^{-i\tau}c_0|m\rangle|1,1\rangle|+\rangle + e^{-i\tau}\frac{c_0}{\sqrt{2}}|m\rangle|1,0\rangle|-\rangle + e^{-i\tau}\frac{c_1}{\sqrt{2}}|m\rangle|1,1\rangle|+\rangle \\
&+ e^{i\tau}\frac{c_1}{\sqrt{2}}|m\rangle|1,-1\rangle|+\rangle + e^{i\tau}c_1|m\rangle|1,0\rangle|-\rangle + e^{-i\tau}i\frac{c_2}{\sqrt{2}}|n\rangle|1,0\rangle|-\rangle + e^{i\tau}ic_2|n\rangle|1,-1\rangle|+\rangle\Big] \\
=&-\mu_B B_{\parallel}\Big[e^{i\tau}(\frac{c_0}{\sqrt{2}}+c_1)|m\rangle|1,0\rangle|-\rangle + e^{-i\tau}(c_0+\frac{c_1}{\sqrt{2}})|m\rangle|1,1\rangle|+\rangle + c_1e^{i\tau}c_1|m\rangle|1,-1\rangle|+\rangle \\
&+ e^{-i\tau}i\frac{c_2}{\sqrt{2}}|n\rangle|1,0\rangle|-\rangle + e^{i\tau}ic_2|m\rangle|1,-1\rangle|+\rangle\Big]
\end{aligned} \tag{4.35}$$

Now, we apply $\langle\Psi^{-}|$ onto Eq. (4.35). We see that the states on $|n\rangle$ drop out. The remaining states yield

$$\langle\Psi^{-}|\mathbf{B}\cdot\mu|\Psi^{+}\rangle = -\mu_B B_{\parallel}e^{i\tau}\left[c_1\left(\frac{c_0}{\sqrt{2}}+c_1+c_0\right)\right] . \tag{4.36}$$

Thus, our general Hamiltonian becomes

$$H = \lambda\left[\left(\mathbf{q}-\frac{e\mathbf{A}}{c}\right)\times\boldsymbol{\sigma}\right]\cdot\hat{z} + m_{\perp}\sigma_z B_{\perp} + m_{\parallel}\mathbf{B}_{\parallel}\cdot\sigma_{\parallel} \tag{4.37}$$

where $m_{\perp} = -\mu_B(c_1^2 - 2c_2^2)$ and $m_{\parallel} = -\mu_B\left[c_1\left(\frac{c_0}{\sqrt{2}}+c_1+c_0\right)\right]$. We indeed find that the electron couples to magnetic field $\propto \mathbf{B}\cdot\boldsymbol{\sigma}$. The strength of coupling however is

not isotropic and it depends on the orbital character. Interestingly, $m_\perp$ depends on the wavefunction coefficients of atom m with out-of-plane orbital number and atom n with in-plane orbital number, while $m_\parallel$ depends on the wavefunction coefficients of *same* atoms but with different orbital orientations (see Eq. 4.18). This suggests that by changing the geometry or the atomic compositions we can tune the relative strength of in-plane and out-of-plane couplings.

4.5 In-Plane Field

If the field is in-plane, the Hamiltonian is given by

$$H = \begin{pmatrix} 0 & i\lambda q e^{i\phi} + \mathcal{B}e^{-i\tau} \\ -i\lambda q e^{-i\phi} + \mathcal{B}e^{i\tau} & 0 \end{pmatrix} = \lambda \begin{pmatrix} 0 & iqe^{i\phi} + \frac{\mathcal{B}}{\lambda}e^{-i\tau} \\ -iqe^{-i\phi} + \frac{\mathcal{B}}{\lambda}e^{i\tau} & 0 \end{pmatrix}, \tag{4.38}$$

where we have defined $\mathcal{B} \equiv m_\parallel B_\parallel$. The eigenvalues become

$$\mathcal{E} = \pm\lambda\sqrt{\left(q_x - \frac{\mathcal{B}}{\lambda}\sin\tau\right)^2 + \left(q_y - \frac{\mathcal{B}}{\lambda}\cos\tau\right)^2}. \tag{4.39}$$

Applying an in-plane magnetic field shifts the cone in the Brillouin zone.

Let us take a closer look at the Hamiltonian:

$$\begin{aligned} H &= \lambda \begin{pmatrix} 0 & i\left[\left(q_x - \frac{\mathcal{B}}{\lambda}\sin\tau\right) + i\left(q_y - \frac{\mathcal{B}}{\lambda}\cos\tau\right)\right] \\ -i\left[\left(q_x - \frac{\mathcal{B}}{\lambda}\sin\tau\right) - i\left(q_y - \frac{\mathcal{B}}{\lambda}\cos\tau\right)\right] & 0 \end{pmatrix} \\ &= \lambda \begin{pmatrix} 0 & ipe^{i\xi} \\ -ipe^{-i\xi} & 0 \end{pmatrix}. \end{aligned} \tag{4.40}$$

The eigenstates are

$$|I\rangle = \frac{|\Psi^+\rangle + ie^{-i\xi}|\Psi^-\rangle}{\sqrt{2}}\,,$$
$$|II\rangle = \frac{|\Psi^+\rangle - ie^{-i\xi}|\Psi^-\rangle}{\sqrt{2}}\,. \tag{4.41}$$

Now we can obtain the in-plane spin texture for the cones. First, it is easy to show that

$$\langle\Psi^{\rm I}|\sigma_{x/y}|\Psi^{\rm I}\rangle = \langle\Psi^{\rm II}|\sigma_{x/y}|\Psi^{\rm II}\rangle = 0\,. \tag{4.42}$$

Next,

$$\langle\Psi^{\rm II}|\sigma_x|\Psi^{\rm I}\rangle = c_1^2\langle+|\sigma_x|-\rangle = c_1^2\,,$$
$$\langle\Psi^{\rm II}|\sigma_y|\Psi^{\rm I}\rangle = c_1^2\langle+|\sigma_y|-\rangle \ = -ic_1^2\,. \tag{4.43}$$

This leads to

$$\langle I|\sigma_x|I\rangle = \frac{-ie^{i\xi}}{2}c_1^2 + \frac{ie^{-i\xi}}{2}c_1^2 = -i\frac{c_1^2}{2}\left(e^{i\xi} - e^{-i\xi}\right) = c_1^2\sin\xi\,,$$
$$\langle I|\sigma_y|I\rangle = -ic_1^2\frac{-ie^{i\xi}}{2} + ic_1^2\frac{ie^{-i\xi}}{2} = -c_1^2\frac{e^{i\xi}}{2} - c_1^2\frac{e^{-i\xi}}{2} = -c_1^2\cos\xi\,,$$
$$\langle II|\sigma_x|II\rangle = \frac{ie^{i\xi}}{2}c_1^2 + \frac{-ie^{-i\xi}}{2}c_1^2 = -c_1^2\sin\xi\,,$$
$$\langle II|\sigma_y|II\rangle = ic_1^2\frac{-ie^{i\xi}}{2} - ic_1^2\frac{ie^{-i\xi}}{2} = c_1^2\cos\xi\,. \tag{4.44}$$

As a result, the spin texture becomes:

$$\langle I|\hat{\sigma}|I\rangle = c_1^2\left(\hat{x}\sin\xi - \hat{y}\cos\xi\right) \propto \left(\hat{x}p_y - \hat{y}p_x\right)\,,$$
$$\langle II|\hat{\sigma}|II\rangle = -c_1^2\left(\hat{x}\sin\xi - \hat{y}\cos\xi\right) \propto -\left(\hat{x}p_y - \hat{y}p_x\right)\,. \tag{4.45}$$

Recall that

$$p_x = q_x - \frac{\lambda}{\hbar v}\sin\tau\,,$$
$$p_y = q_y - \frac{\lambda}{\hbar v}\cos\tau\,. \tag{4.46}$$

This means that spin contours now revolve not around the $\mathbf{q} = 0$ point but instead around a $\mathbf{p} = 0$ point.

4.6 Landau Levels

For the transverse magnetic field $B\hat{z}$, we have $\mathbf{A} = Bx\hat{y}$, leading to

$$H = \hbar v \begin{pmatrix} M & ik_x - \left(k_y - \frac{eB}{\hbar c}x\right) \\ -ik_x - \left(k_y - \frac{eB}{\hbar c}x\right) & -M \end{pmatrix}. \tag{4.47}$$

Since the gauge field is x dependent, we can focus on the part of wavefunction that has x dependent. From this, we can write

$$H\Psi = \hbar v \begin{pmatrix} M & ik_x + \frac{eB}{\hbar c}x \\ -ik_x + \frac{eB}{\hbar c}x & -M \end{pmatrix} \begin{pmatrix} \psi_1(x) \\ \psi_2(x) \end{pmatrix} = E \begin{pmatrix} \psi_1(x) \\ \psi_2(x) \end{pmatrix},$$
$$\left[ik_x + \frac{eB}{\hbar c}x\right]\psi_2(x) = \left(\frac{E}{\hbar v} - M\right)\psi_1(x)\,,$$
$$\left[-ik_x + \frac{eB}{\hbar c}x\right]\psi_1(x) = \left(\frac{E}{\hbar v} + M\right)\psi_2(x)\,. \tag{4.48}$$

Combining the last two equations yields, the left hand side becomes

$$\left[-ik_x + \frac{eB}{\hbar c}x\right]\left[ik_x + \frac{eB}{\hbar c}x\right]\psi_2(x) = \left[k_x^2 + i\frac{eB}{\hbar c}(xk_x - k_x x) + \left(\frac{eB}{\hbar c}\right)^2 x^2\right]\psi_2(x)\,,$$

and the right hand side becomes

$$\left(\frac{E}{\hbar v}-M\right)\left(\frac{E}{\hbar v}+M\right)\psi_2(x)=\left[\left(\frac{E}{\hbar v}\right)^2-M^2\right]\psi_2(x)\,.$$

We then can solve $\psi_2(x)$,

$$\left[k_x^2+\left(\frac{eB}{\hbar c}\right)^2x^2\right]\psi_2(x)=\left[\left(\frac{E}{\hbar v}\right)^2-M^2+\frac{eB}{\hbar c}\right]\psi_2(x)\,,$$

$$\psi_2(x)=D_{\frac{\left(\frac{E}{\hbar v}\right)^2-M^2}{2\frac{eB}{\hbar c}}}\left[\sqrt{\frac{2eB}{\hbar c}}x\right]\,. \tag{4.49}$$

And similarly we can solve $\psi_1(x)$,

$$\left[k_x^2+\left(\frac{eB}{\hbar c}\right)^2x^2\right]\psi_1(x)=\left[\left(\frac{E}{\hbar v}\right)^2-M^2-\frac{eB}{\hbar c}\right]\psi_1(x)\,,$$

$$\psi_1(x)=D_{\frac{\left(\frac{E}{\hbar v}\right)^2-M^2-2\frac{eB}{\hbar c}}{2\frac{eB}{\hbar c}}}\left[\sqrt{\frac{2eB}{\hbar c}}x\right]\,. \tag{4.50}$$

This leads to

$$\frac{\left(\frac{E}{\hbar v}\right)^2-M^2}{2\frac{eB}{\hbar c}}=n\rightarrow\left(\frac{E}{\hbar v}\right)^2=2\frac{eB}{\hbar c}n+M^2\,, \tag{4.51}$$

$$\frac{\left(\frac{E}{\hbar v}\right)^2-M^2-2\frac{eB}{\hbar c}}{2\frac{eB}{\hbar c}}=m\rightarrow\left(\frac{E}{\hbar v}\right)^2=2\frac{eB}{\hbar c}\left(m+1\right)+M^2\,, \tag{4.52}$$

$$\psi_1(x)=D_m\left[\sqrt{\frac{2eB}{\hbar c}}x\right]=2^{-m/2}\exp\left[-\frac{1}{2}\frac{eB}{\hbar c}x^2\right]H_m\left[\sqrt{\frac{eB}{\hbar c}}x\right]\,, \tag{4.53}$$

where H_m is the Hermite polynomials.

Finally, we obtain

$$\left(\frac{E}{\hbar v}\right)^2 - M^2 + \frac{eB}{\hbar c} = \frac{eB}{\hbar c}(2n+1) \rightarrow E = \pm\hbar v\sqrt{\frac{2eB}{\hbar c}n + M^2}\,, \tag{4.54}$$

$$\left(\frac{E}{\hbar v}\right)^2 - M^2 - \frac{eB}{\hbar c} = \frac{eB}{\hbar c}(2n+1) \rightarrow E = \pm\hbar v\sqrt{\frac{2eB}{\hbar c}(n+1) + M^2}\,. \tag{4.55}$$

Combining the last two equations yields

$$\begin{aligned}\left[k_x^2 + \left(\frac{eB}{\hbar c}\right)^2 x^2\right]\psi_2(x) &= \frac{eB}{\hbar c}\left[2n+1\right]\psi_2(x)\,,\\ \left[k_x^2 + \left(\frac{eB}{\hbar c}\right)^2 x^2\right]\psi_1(x) &= \frac{eB}{\hbar c}\left[2n-1\right]\psi_1(x)\,.\end{aligned} \tag{4.56}$$

Finally, we get

$$\left(\frac{E}{\hbar v}\right)^2 - M^2 + \frac{eB}{\hbar c} = \frac{eB}{\hbar c}(2n+1) \rightarrow E = \pm\hbar v\sqrt{\frac{2eB}{\hbar c}n + M^2}\,, \tag{4.57}$$

$$\left(\frac{E}{\hbar v}\right)^2 - M^2 - \frac{eB}{\hbar c} = \frac{eB}{\hbar c}(2n+1) \rightarrow E = \pm\hbar v\sqrt{\frac{2eB}{\hbar c}(n+1) + M^2}\,, \tag{4.58}$$

where $n = 0, 1, 2\cdot$ similar to the values in Harmonic oscillator. First we find that for $n = 0$ only one of the electron with spin up (or down depending on direction of magnetic field) occupies the lowest energy. In the vicinity of the M point, we expect PbX to have Landau level with a $\sqrt{n}$ energy spacing which is similar to graphene [98]. Landau level of Dirac electrons in 3D Rashba materials have also been observed experimentally [99]. This shows the promise of using the helical spin polarization of non-degenerate Dirac electrons to develop new spintronics.

Chapter 5

Two-dimensional Square Buckled Rashba Lead Chalcogenides

In this chapter we propose the lead sulphide (PbS) monolayer as a 2D semiconductor with a large Rashba-like spin-orbit effect controlled by the out-of-plane buckling. The buckled PbS conduction band is found to possess Rashba-like dispersion and spin texture at the M and Γ points, with large effective Rashba parameters of $\lambda \sim 5$ eVÅ and $\lambda \sim 1$ eVÅ, respectively. Using a tight-binding formalism, we show that the Rashba effect originates from the very large spin-orbit interaction and the hopping term that mixes the in-plane and out-of-plane p orbitals of Pb and S atoms. The latter, which depends on the buckling angle, can be controlled by applying strain to vary the spin texture as well as the Rashba parameter at Γ and M. Our density functional theory results together with tight-binding formalism provide a unifying framework for designing Rashba monolayers and for manipulating their spin properties.

The work presented in this chapter (with slight modifications) has been published in:

- **P. Z. Hanakata**, A. S. Rodin, A. Carvalho, H. S. Park, D. K. Campbell, A. H. C. Neto,"Two-dimensional square buckled Rashba lead chalcogenides" *Physical Review B* 96 (16), 161401(R) (2017).

5.1 Introduction

Over the past two decades there has been a growing interest in materials with strong spin-orbit interaction (SOI), as they are of a profound importance for fundamental understanding of quantum phenomena at the atomic level and applications to spintronics. This relativistic interaction is linked to important effects such as Rashba, Zeeman, spin-Hall effect, and topological insulator (TI) states [100, 101, 102, 103].

The spin-orbit splitting of the bands occurs in crystals without inversion symmetry, where it is known as Dresselhaus effect and in 2D structures or surfaces, where it is known as Rashba effect, even though these can be seen as different manifestations of the same phenomenon [104]. However, suitable atomically thin 2D materials with a large Rashba coefficient are hard to find. To have Rashba-type spin splitting there are two key properties that should present: strong SOI and broken inversion symmetry. In graphene and non-polar two-dimensional materials, such as transition metal dichalcogenides, breaking inversion symmetry is often achieved by application of out-of-plane electric fields or through interfacial effects [105, 106, 107]. Unfortunately, the respective spin splitting in graphene is rather small, rendering the spin polarization unusable at room temperature. Group IV and III-V binary monolayers (e.g SiGe and GaAs) with buckled hexagonal geometry were found to have a Rashba-like spin texture; the band splitting, however, has a Zeeman-like splitting [108]. Spin-splitting in WSe_2 monolayer is also of Zeeman-type due to the out-of plane mirror symmetry ($M_z : z \rightarrow -z$) suppressing the Rashba term [106]. Transition metal dichalcogenides with asymmetric surfaces, e.g. WSeTe, have a sizeable Rashba splitting, but this does not coincide with the direct bandgap [109]. A Rashba-type effect has been measured in few-layer samples of the topological insulator Bi_2Se_3, but this is attributed to the interactions with the substrate [110].

Recently, we proposed that a Rashba-like splitting can also be obtained in bucked

heavy metal square lattices, where it is controlled by out-of-plane buckling and/or electric dipole [36]. However, materials in this class are almost always metals, which reduces the ways in which spins can be manipulated.

In addition to study of spin splitting and texture in materials with strong SOI, several works have also investigated the orbital switching in topological insulators [111, 112] and in *hexagonal* 3D Rashba semiconductors [113, 114]. Specifically, Cao et al. found that below the Dirac point the wavefunctions are more radial while above the Dirac point the wavefunctions are more tangential [111]. However, further studies for materials with different geometry (e.g square) are still lacking.

Very recently, several studies have investigated topological properties of the rock salt structure materials, such as PbX (X=Se, S, Te), in both monolayer and bilayer forms with no buckling [102, 103, 115]. In particular, Chang et al. have successfully grown few-layer SnTe and PbTe [116] [1]. In this article, we study two-dimensional (2D) lead chalcogenide PbX (X=S, Se, Te) monolayers in square geometry with two atoms per primitive cell. For definiteness, we focus on lead sulfide PbS, but similar effects can be found for other lead chalcogenides and even heavy metals [36].

Using density functional theory (DFT), we find that buckled PbS monolayer possesses a strong Rashba splitting. In this polar material, the buckling direction can be reversed, leading to the reversal of the spin texture. Based on our DFT results we develop a tight binding formulation of the buckled and planar 2D square lattice for PbS which is generally applicable for other similar materials (*e.g*, PbSe and PbTe). With this formalism, we are able to understand how the Rashba spitting depends on SOI strength, which in turn depends on the atomic species and the buckling angle, similar to the case of heavy metal square lattices [36]. Moreover, our theory provides a new understanding of how spins and orbitals are coupled and

[1] Chang et al. reported PbTe data in the supplementary section.

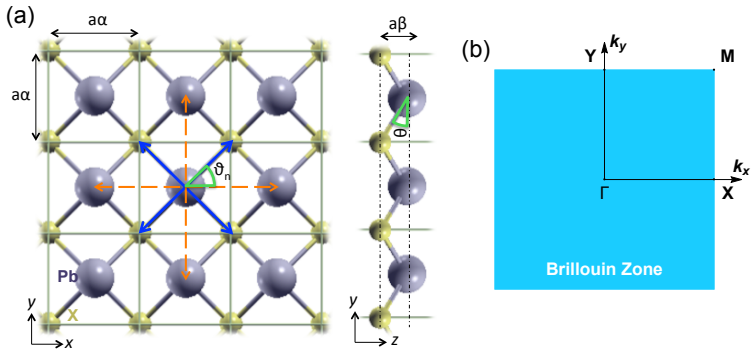

Figure 5.1: (a) Structural visualizations of buckled PbX monolayer. Buckling angle $\theta = 0$ ($\beta = 0$) for planar structure. Blue and orange arrows indicate vectors connecting Pb and its first and second nearest neighbors, respectively and (b) the corresponding Brillouin zone.

how they can be controlled. These all together provide guidelines for designing and manipulating orbital-spin effects in Rashba monolayers.

5.2 Methods

The structural visualization of buckled PbX is shown in fig. 5.1. Our findings are based on density functional theory (DFT) calculations implemented in the Quantum ESPRESSO package [82]. We employed Projector Augmented-Wave (PAW) type pseudopotentials with Perdew-Burke-Ernzerhof (PBE) within the generalized gradient approximation (GGA) for the exchange and correlation functional [117]. The Kohn-Sham orbitals were expanded in a plane-wave basis with a cutoff energy of 100 Ry, and for the charge density a cutoff of 200 Ry was used. A k-point grid sampling grid was generated using the Monkhorst-Pack scheme with 16×16×1 points [84], and a finer regular grid of 40×40×1 was used for spin texture calculations. We used the modern theory of polarization [85] to calculate the spontaneous polarization implemented in the Quantum ESPRESSO package [82]. Input files can be found in A.0.3. To compare the electric polarization of monolayer PbS to

the typical bulk ferroelectrics, we approximate the thickness as twice the distance between S and Pb atom which is roughly half of the lattice constant of bulk PbS. Similar approximations have also been used in other several works [32, 118, 119].

For electronic band structure calculations, the spin orbit interaction was included using noncollinear calculations with fully relativistic pseudopotentials. To apply biaxial strains, we varied the in-plane lattice constants and let the system relax until the stress perpendicular to the plane is less than 0.01 GPa.

We used the modern theory of polarization to calculate electric polarization[85]

$$\vec{\mathcal{P}} = \frac{1}{V}\sum_{\tau} q_{\tau}^{\text{ion}}\mathbf{R}_{\tau} - \frac{2ie}{(2\pi)^3}\sum_{n}^{\text{occ}}\int_{BZ} d^3\mathbf{k}e^{-i\vec{k}\cdot\mathbf{R}}\left\langle \Psi_{n\mathbf{k}}\middle|\frac{\partial\Psi_{n\mathbf{k}}}{\partial\mathbf{k}}\right\rangle, \tag{5.1}$$

where q_{τ} is the ionic charge plus the core electrons, $\mathbf{R}_{\tau}$ is the position of ions, V is the unit cell volume, e is the elementary charge, n is the valence band index, $\mathbf{k}$ is the wave vector, and $\Psi_{n\mathbf{k}}$ is the electronic wave function. The first term is the contribution from core electrons and ions, and the second term is the electronic contribution defined as the adiabatic flow of current, which can be calculated from the Berry phase (BP) [85]. The spontaneous polarization is calculated by taking the difference between the polarization of the polar (buckled) state and the non-polar (reference) state, $\Delta\vec{\mathcal{P}} = \vec{\mathcal{P}}_{\text{polar}} - \vec{\mathcal{P}}_{\text{non-polar}}$. To calculate the electric polarization of monolayer PbS, we estimate the thickness as twice the distance between S and Pb atom which is roughly half of the lattice constant of bulk PbS. Similar approximations have also done in other several works [32, 118, 119].The calculated spontaneous polarizations of path I (optimized buckled lattice parameters) and path II (optimized planar lattice parameters) are 0.2 C/m^2 and 0.1 C/m^2, respectively.

Here we tabulate the optimized geometrical parameters of buckled PbX (X=S, Se, and Te) monolayers.

Table 5.1: Lattice constant a, buckling angle θ, buckling height d_z, and nearest-neighbor bond distance d.

	a Å	$\theta(^\circ)$	d_z Å	d Å
PbS	3.74	21.6	1.04	2.84
PbSe	3.82	24.4	1.22	2.96
PbTe	4.01	26.3	1.40	3.16

5.3 Structure, bistability, and ferroelectricity

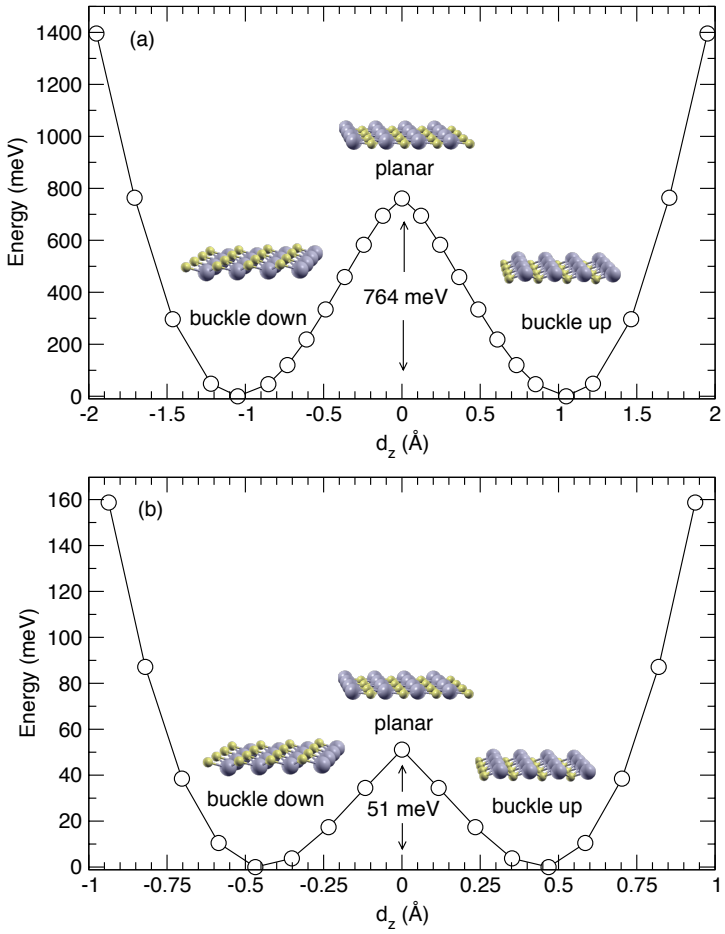

Figure 5.2: Potential energy surface of PbS as a function of distance d_z with (a) fixed buckled lattice parameters and (b) fixed planar lattice parameters.

Our first principles calculations show that PbX monolayer has a buckled structure

(see fig. 5.2), which is a minimum of the energy surface, whereas the planar structure is a saddle point of the energy surface. We found that the optimized buckled structure of PbS has a lower enthalpy of 120 meV compared to that of optimized planar structure. The lattice constant a and buckling angle θ for buckled (planar) structure are 3.74Å (4.01Å) and 21.6° (0°), respectively. The optimized planar lattice constant is close to the value reported in study of planar PbS [115].

The potential energy barriers in ferroelectric materials are usually strain dependent. For instance, Wang and Qian have shown that energy barriers in ferroelectric SnS, SnSe, GeS, and GeSe monolayers may increase or decrease depending on the strains [119].

The energy barrier between the planar (paraelectric) and buckled (ferroelectric) is obtained by displacing the Pb and S atoms in the z direction while keeping the lattice parameters fixed at the values optimized for the the buckled (ferroelectric) phase. We vary $d_z = z(\text{Pb}) - z(\text{S})$ with the fixed optimized ferroelectric (buckled) lattice parameters, the energy barrier is 764 meV and the spontaneous polarization is $\Delta\vec{\mathcal{P}} = 0.2$ C/m^2. Since the calculation is carried out keeping the lattice parameters fixed at the values optimized for the buckled phase, the relative energy of the paraelectric phase is overestimated (see fig. 5.2 (a)). In addition, we also do the same procedure but using the paraelectric (planar) phase as the initial configuration. When the lattice parameters are fixed at the optimized paraelectric phase, the energy barrier is 51 meV and the spontaneous polarization is $\Delta\vec{\mathcal{P}} = 0.1$ C/m^2, shown in fig. 5.2 (b)). In either case, we find that the planar structure is a saddle point.

We approximate the energy surface to a fourth order polynomial function [120]

$$E = \eta_1 \mathcal{P}^2 + \eta_2 \mathcal{P}^4 \tag{5.2}$$

Knowing $\Delta\mathcal{P}$ and the E_{barrier}, we obtain $\eta_1 = \frac{2E_{\text{barrier}}}{\Delta\mathcal{P}^2}$ and $\eta_2 = -\frac{E_{\text{barrier}}}{\mathcal{P}^4}$. Next we introduce the electric enthalpy $F = E - \mathcal{E}\mathcal{P}$, where $\mathcal{E}$ is the electric field we the can calculate the coercive field $\mathcal{E}_c = (4/3)^{(3/2)} E_{\text{barrier}}/\Delta\mathcal{P}$. The calculated coercive field with the starting configuration from paraelectric (planar) and ferroelectric (buckled) are, ~ 1 V/nm and ~ 10 V/nm respectively. Applied electric fields of ~ 1 V/nm are achievable in current 2D experiments [93]. This suggests that PbS is suitable for a ferroelectric device as long as it is grown in planar phase.

5.4 Band structure

Next we compare the band structure of planar PbS (PbS-p) and buckled PbS (PbS-b). PbS-p is a direct gap semiconductor with a small bandgap of 0.2 eV. Because of the inversion symmetry, no spin-splitting is observed. PbS-b is an indirect-gap semiconductor in which the minimum energy of the lowest conduction band is located near the M-point and the maximum energy of the highest valence band is located near the Γ-point (see fig. 5.3). At both the M and Γ points, the conduction band shows a sizable Rashba splitting. The effective Rashba parameters, given by $\lambda = 2E_R/k_R$, where E_R is the difference between the lowest energy of upper band and lower band, k_R is the shift in momentum space relative to the cone axis, are $\lambda = 1.03$ eVÅ at Γ (fig. 5.4(a)) and $\lambda = 5.10$ eVÅ at M (fig. 5.4 (b)). These values are comparable to those of three-dimensional (3D) giant Rashba materials [100, 101, 121].

5.5 Origin of the Spin Splitting: A Tight-binding Formulation

Next, we use tight binding formalism as a framework to understand the Rashba effects in lead chalcogenide monolayers. We first need to find the relevant orbitals.The ab

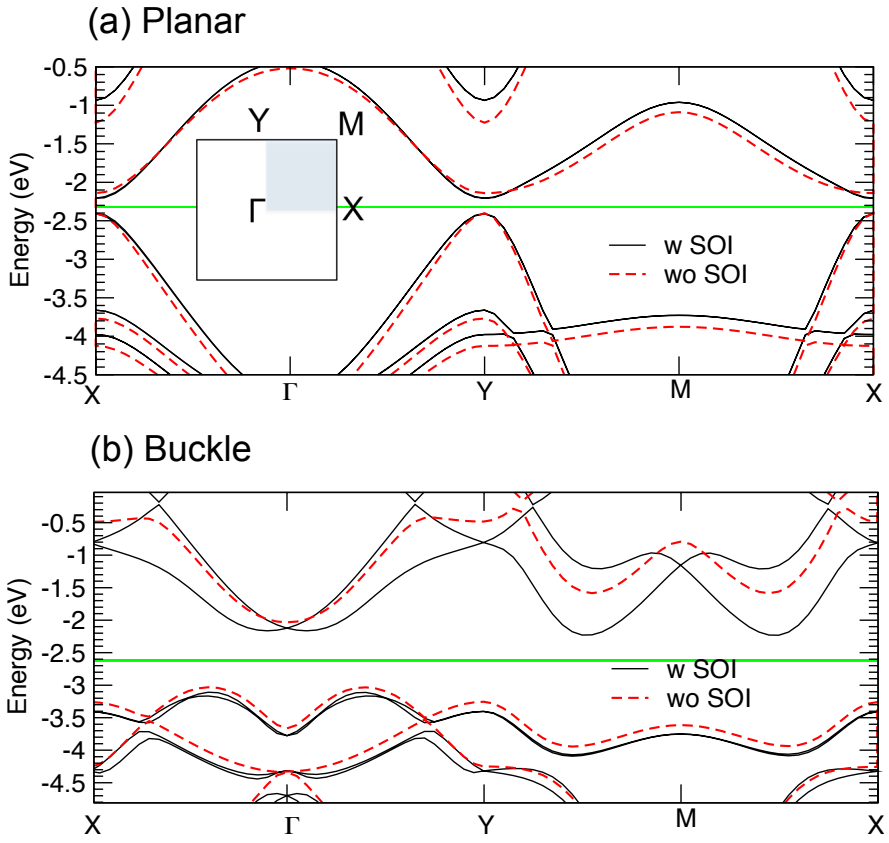

Figure 5.3: Band structure of monolayer PbS in planar (a) and buckled structure (b) along the high symmetry lines of Brillouin zone. Green lines indicate Fermi energy. There is no splitting in the planar structure because of inversion symmetry. In contrast, there is no mirror-plane in z for buckled structure resulting broken inversion symmetry, and this leads to band-splitting. The calculated Rashba parameter at Γ (M) gives rise to a larger energy splitting between bands than other giant Rashba materials. Rashba-like dispersion at Γ (c) and M point (d).

initio calculations reveal a fairly complicated band structure with multiple local minima in the conduction band and a fairly flat valence band. In order to better understand the origin of the band structure, we turn to the tight-binding model.

Numerical calculations show that the relevant bands are composed almost exclusively of s and p orbitals of the constituent atoms, with d appearing in lower-energy valence bands, allowing us to neglect them (see fig. 5.5). The lowest conduction band

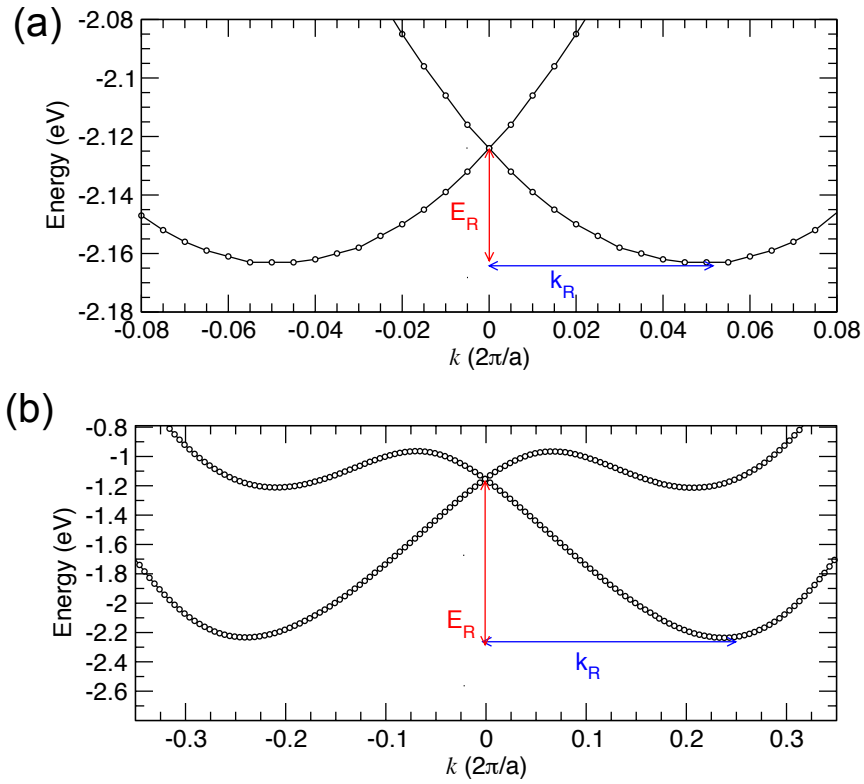

Figure 5.4: Rashba-like dispersion at Γ (a) and M point (b) of buckled PbX monolayer.

consists mostly the p orbitals of the Pb atom while the highest valence band consists mostly the p orbitals of the S atom.

This means that each atom introduces four (one s and three p) orbitals. While it is convenient to use p_x and p_y orbitals to write down the hopping elements, since we are including SOI in our model, it is helpful to go to a basis which is more natural for the angular momentum operators. We transform the basis as follows:

$$|1,1\rangle = (-|p_x\rangle + i|p_y\rangle)/\sqrt{2} \quad \text{and} |1,-1\rangle \qquad = (|p_x\rangle + i|p_y\rangle)/\sqrt{2}. \tag{5.3}$$

The new basis then for each 4×4 block is $|0,0\rangle$, $|1,1\rangle$, $|1,-1\rangle$, and $|1,0\rangle$, where

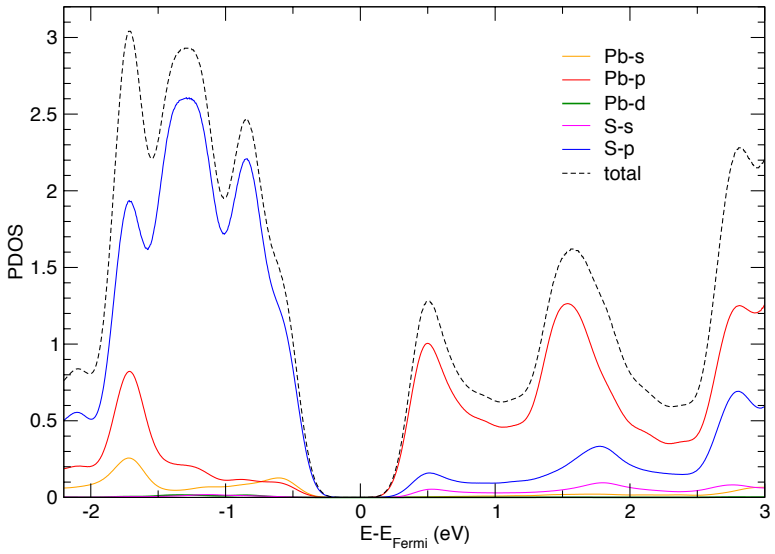

Figure 5.5: Projected density of states (PDOS) of Pb and S atoms. Note that the Pb-d contribution is too small to be seen on this figure

the first number represents the orbital momentum quantum number and the second one is the projection along the z direction. We have carried detailed derivations in chapter 4. In this chapter, we will focus on the M point. Some of the notations are slightly different from the previous chapter.

The first high-symmetry point that we examine is the M-point, located at $(\pi/2, \pi/2)$ in the Brillouin zone. At the M-point the full Hamiltonian H can be decomposed into several blocks, and the Hamiltonian describing the two lowest conduction bands (C1, C2) and the third valence band (V3) is given by

$$H_1 = \left(\varepsilon_s^{\mathrm{Pb}}\right) , \quad H_2 = \left(\varepsilon_s^{\mathrm{S}}\right) , \tag{5.4}$$

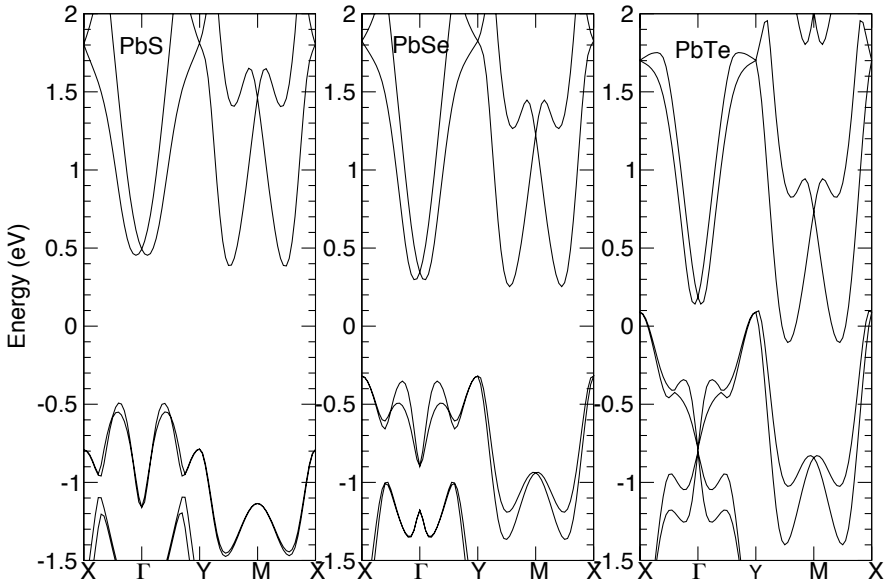

Figure 5.6: Band structures of buckled PbS, PbSe and PbTe with spin-orbit interaction included. Fermi energy is set to be zero. All buckled lead chalcogenides have large Rashba splitting in the conduction band. In the highest valence bands, however, the Rashba splitting is smaller for compounds containing lighter chalcogen species.

$$H_a = \begin{pmatrix} \varepsilon_p^{\mathrm{Pb}} + \frac{T_{\mathrm{Pb}}}{2} & 0 & \pm 4i\alpha^2\Delta \\ 0 & \varepsilon_p^{\mathrm{S}} & \frac{T_{\mathrm{S}}}{\sqrt{2}} \\ \mp 4i\alpha^2\Delta & \frac{T_{\mathrm{S}}}{\sqrt{2}} & \varepsilon_p^{\mathrm{S}} - \frac{T_{\mathrm{S}}}{2} \end{pmatrix}, \tag{5.5}$$

$$H_b = \begin{pmatrix} \varepsilon_p^{\mathrm{S}} + \frac{T_{\mathrm{S}}}{2} & \mp 4i\alpha^2\Delta & 0 \\ \pm 4i\alpha^2\Delta & \varepsilon_p^{\mathrm{Pb}} - \frac{T_{\mathrm{Pb}}}{2} & \frac{T_{\mathrm{Pb}}}{\sqrt{2}} \\ 0 & \frac{T_{\mathrm{Pb}}}{\sqrt{2}} & \varepsilon_p^{\mathrm{Pb}} \end{pmatrix}. \tag{5.6}$$

At the M-point, the degenerate wave functions (labeled as 1 and 2) describing

the lowest conduction band C1 are given by

$$|\Psi_1\rangle = iA|1,1\rangle \otimes |\uparrow\rangle_{\rm S} \; + B|1,-1\rangle \otimes |\uparrow\rangle_{\rm Pb} + C|1,0\rangle \otimes |\downarrow\rangle_{\rm Pb}$$
$$|\Psi_2\rangle = -iA|1,-1\rangle \otimes |\downarrow\rangle_{\rm S} + B|1,1\rangle \otimes |\downarrow\rangle_{\rm Pb} + C|1,0\rangle \otimes |\uparrow\rangle_{\rm Pb}\,, \qquad (5.7)$$

where A, B and C are real numbers. The other block H_a describing the highest valence (V1) band has a very similar form to Eq. 5.6, but where Pb and S are interchanged.

The degeneracy breaking term γ is given by

$$\gamma = \langle\Psi_1|H|\Psi_2\rangle = 2i\sin(2\theta)\,\Delta k e^{i\phi} AC\,, \qquad (5.8)$$

where θ is the structure buckling angle, where $\Delta = V_{pp\sigma} - V_{pp\pi}$ (V is the hopping parameter between S and Pb atom, see Supplemental Material), and $ke^{i\phi} = k_x + ik_y$. This leads to a linear dispersion for small k, as expected. Defining $\lambda \equiv 2\sin(2\theta)\,\Delta AC$, we can write the effective Hamiltonian describing the lowest conduction band as

$$H_{\rm eff} = \lambda[\vec{k} \times \vec{\sigma}] \cdot \hat{z}, \qquad (5.9)$$

where $\vec{\sigma} = (\sigma_x, \sigma_y, \sigma_z)$, which is the Rashba Hamiltonian. The eigenstates are $|\psi_{\rm I,II}\rangle = |\Psi_1\rangle \pm e^{-i\phi}\frac{|\lambda|}{\lambda}|\Psi_2\rangle$.

It is clear from Eq. 5.6 that the SOI mixes the p_z orbital with other in-plane orbitals of atoms with same species; however SOI by itself does not lift the degeneracy because SOI is independent of k. For instance, the band structure of *planar* PbS obtained by DFT, including the SOI, does not show spin-splitting [Fig. 5.3 (a)]. The inversion symmetry breaking term originated from the buckling couples the p_z of Pb and the in-plane p orbitals of S atoms; this term results in the spin-splitting with

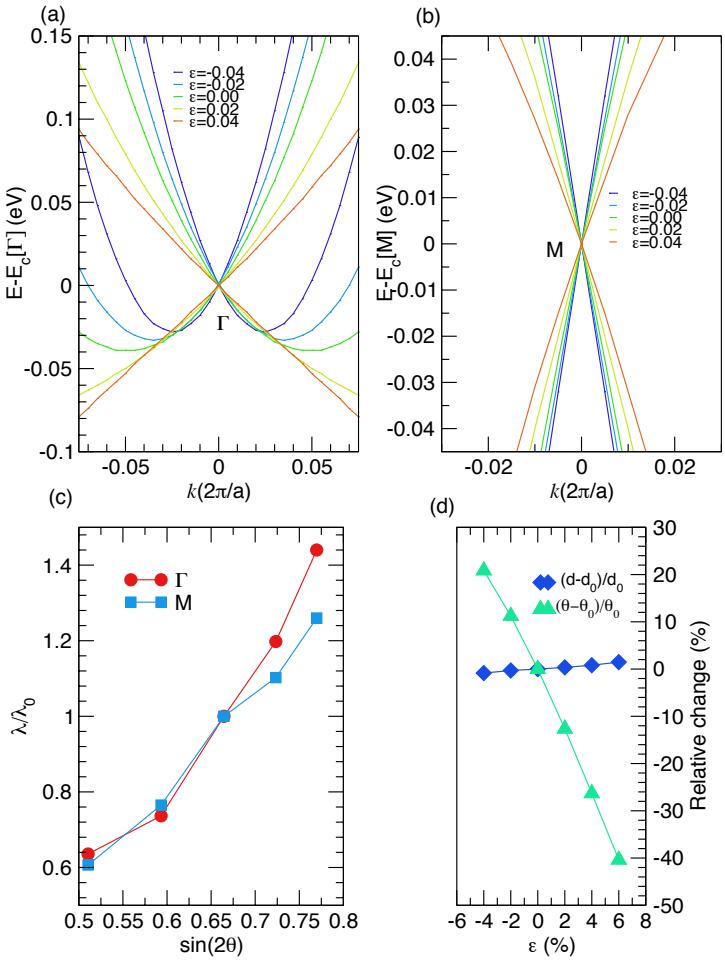

Figure 5.7: Evolution of band structure around Γ (a) and M (b) with application of biaxial strains. Energy is subtracted by energy at Γ (M) for comparative purposes. (b) λ scaled by its unstrained value λ_0 as a function of $\sin 2\theta$. λ increases with increasing buckling angle, which is consistent with tight-binding analysis. (c) Relative changes in buckling angle θ and bond distance d as a function of biaxial strain ϵ.

Rashba-like dispersion (see Eq. 5.8). Taking $T_{\mathrm{Pb}} \gg T_{\mathrm{S}}$ and solving the Hamiltonian H_b perturbatively, which we have shown in Chapter 4, to the first leading order, $AC \sim T_{\mathrm{Pb}}$. These two consequences are consistent with our DFT results: spin-splitting occurs when both SOI and θ are not zero.

While the same arguments hold for H_a, which describes the valence band, we do not observe a substantial SOI-induced splitting in PbS (see Fig. 5.3(b)). This

is because the sulphur atom has of a much smaller atomic SOI than the Pb atom, leading to a weaker mixing of orbitals, suppressing the AC term in the equation above. As shown in fig. 5.6, PbTe and PbSe, however, have large spin-splitting in both the conduction and valence bands because Te and Se are relatively much heavier than S (stronger SOI).

Similarly to the M point, one can perform a low-k expansion around the Γ point for the Hamiltonian matrix (see Supplemental Material). Because there are more non-vanishing coupling terms at the center of the Brillouin zone, the Hamiltonian does not reduce as well to smaller independent blocks as it does at the M point. Nevertheless, it is possible to show that in buckled structures, there is a linear term breaking the degeneracy of the conduction band.

We have found the relevant parameters to tune the band splitting from the TB-formulation. Clearly the hopping parameters depend on both the bond distance and the buckling angle. Since these two quantities are often strain dependent, it is natural to ask whether it is possible to tune the hopping parameters using strain. Our DFT simulations showed that under biaxial strains the bond distance changes by only 1% while buckling angle changes by roughly 30% at a biaxial strain of 6% (shown in Fig. 5.7).

We obtain λ by taking the derivative of energy dispersion $\lambda = \frac{\partial E}{\partial k}$ at Γ and M. As shown in Fig. 5.7 (c), λ increases with increasing θ, consistent with our TB formulation (see Eq. 5.8). Note that λ is not linear with $\sin 2\theta$ because A and C also depend on θ. Our DFT results show that, relative to its unstrained value λ_0, λ can increase by more than 20% when compressed by 4% or decrease by 20% when stretched by 4%. The apparent variations of λ show that PbS is a tunable spin-splitting material.

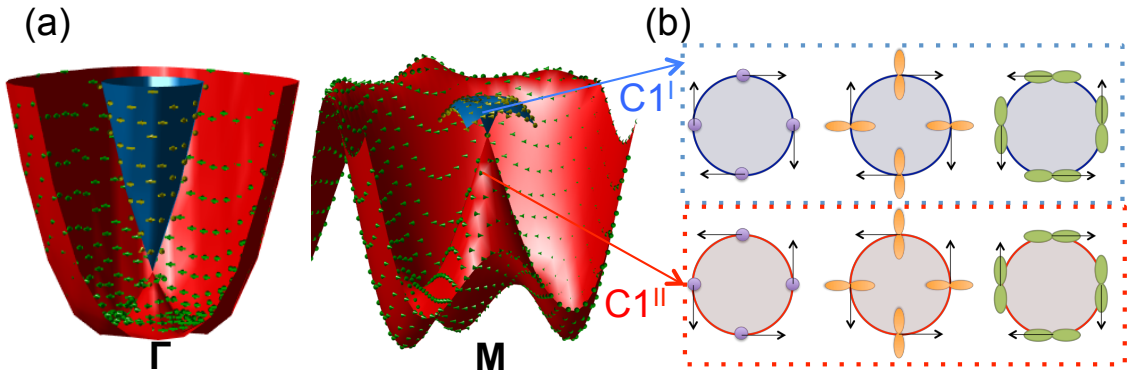

Figure 5.8: (a) Band plots of the first ($C1^{II}$) and second lowest ($C1^{I}$) conduction band near the Γ and M point. Clockwise (counter clockwise) spin textures are represented by the yellow (green) arrows. Near the band crossing (inner Dirac cone), the upper and lower band have opposing helical spin texture similar to the Rashba spin texture. (b) Corresponding schematic orbital spin texture of Pb atom at M point. The radial p_r and tangential p_t have opposite spin orientation, and they cancel each other. Spin helicity is flipped after passing through the Dirac point while the orbital compositions are still the same.

5.6 Spin and Orbital Texture

Lastly, we investigate the orbital texture of PbS as it has been shown that TIs and hexagonal 3D Rashba materials have orbital switching at the Dirac point [111, 112, 113, 114]. To our best knowledge, such analysis has not been done for monolayers with square symmetry. We can do such analysis by transforming our basis to radial p_r and tangential p_t orbitals:

$$|1,1\rangle = -e^{i\phi}|p_r\rangle + i|p_t\rangle \tag{5.10}$$

$$|1,-1\rangle = e^{-i\phi}|p_r\rangle - i|p_t\rangle \tag{5.11}$$

$$|1,0\rangle = |p_z\rangle. \tag{5.12}$$

In this basis the upper and bottom wavefunctions can be written as

$$\begin{aligned}|\psi_{\mathrm{I,II}}\rangle =& C|p_z\rangle \otimes |\pm\rangle_{\mathrm{Pb}} \mp i\frac{B}{\sqrt{2}}|p_r\rangle \otimes |\pm\rangle_{\mathrm{Pb}} \\ &\pm \frac{B}{\sqrt{2}}|p_t\rangle \otimes |\mp\rangle_{\mathrm{Pb}} \mp i\frac{A}{\sqrt{2}}e^{-2i\phi}|p_r\rangle \otimes |\mp_3\rangle_{\mathrm{S}} \\ &\pm \frac{A}{\sqrt{2}}e^{-2i\phi}|p_t\rangle \otimes |\pm_3\rangle_{\mathrm{S}}\end{aligned} \tag{5.13}$$

where

$$|+_n\rangle = \frac{1}{\sqrt{2}}\begin{pmatrix}\frac{|\lambda|}{\lambda}ie^{-in\phi}\\ 1\end{pmatrix} \tag{5.14}$$

is clockwise in-plane spin and

$$|-_n\rangle = \frac{1}{\sqrt{2}}\begin{pmatrix}-\frac{|\lambda|}{\lambda}ie^{-in\phi}\\ 1\end{pmatrix} \tag{5.15}$$

is counter clockwise in-plane spin.

In the upper band of PbS the radial component of the Pb atom couples to the clockwise spin while the tangential component couples to the counter clockwise spin, as shown schematically in Fig. 5.8. As it passes through the band crossing point (Dirac point) right at the M point, where the upper band and lower band meet, the tangential component now couples to the counter clockwise spin. This switching is similar to what have been observed in TIs [111, 112] and hexagonal bulk Rashba materials [113, 114]. The difference is that the radial and tangential components contribute equally and cancel out, and thus the net in-plane spin texture comes from the p_z orbital only. This suggests that the orbital texture is not always polarized and thus the orbital polarization depends on the crystal symmetry of the material.

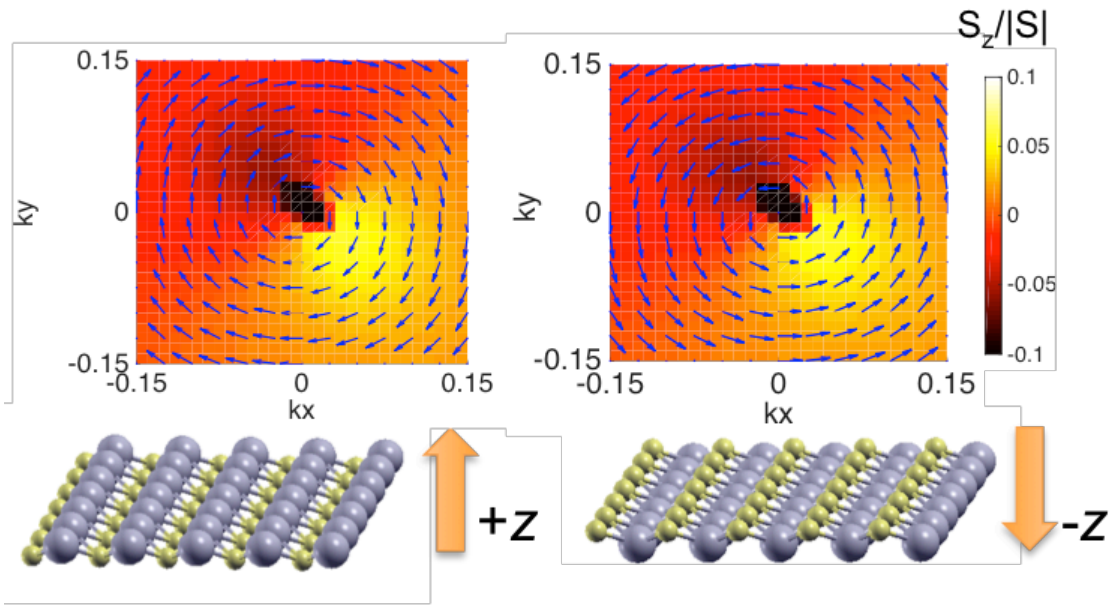

Figure 5.9: Two dimensional plot of spin polarizations near M. The color plot shows the projection of spin along z direction. Clearly, the out-of-plane spin components are small. The direction of spin polarizations is reversed when the buckling direction is reversed.

From the TB results, we found that the direction of the spin is given by

$$\langle \psi_{\mathrm{I,II}} | \hat{\sigma} | \psi_{\mathrm{I,II}} \rangle = \pm \frac{|\lambda|}{\lambda} (\sin\phi, -\cos\phi, 0) \tag{5.16}$$

We can see that the spin texture is helical and depends on the direction of the buckling (inversion symmetry breaking term λ). Notice that the PbS-b has a degenerate structure as the polarization vector in z-direction define as $d_z = z(\mathrm{Pb}) - z(\mathrm{S})$ can be positive or negative (sign of λ), as shown in Fig. 5.9. Thus, the in-plane spin texture can be reversed when λ is negative (PbS buckled in the opposite direction). This is confirmed by our DFT results shown in Fig. 5.9. While the coefficients A, B, and C in Eq. 5.7 are material dependent, the orbital texture is independent of the direction of the buckling. These findings are in agreement with the very recent work on hexagonal 3D Rashba BiTeI [113].

5.7 Summary

In summary, using first-principles calculations based on density functional theory, we have found a new class of 2D materials (lead chalcogenides) possessing a tunable giant Rashba splitting with a characteristic orbital and spin texture in an energy range close to the bandgap edge. Based on our tight-binding analysis, we found that the atomic composition and buckling angle are the two key parameters controlling the Rashba effects. First, the atomic composition plays important role as the SOI is the parameter that mixes the in-plane and out-of-plane orbitals. With the recent success in creating janus (polar) transition metal dichalcogenide monolayers [122] and few-layer SnTe and PbTe [116] via atomic layer deposition techniques, the growth of buckled polar materials like PbS, PbSe, and PbTe should also be achievable using existing technology.

In buckled PbS monolayers, the Rashba coefficient depends on the degree of buckling, and the orientation of the helical in-plane spin depends on the direction of the buckling. As we have shown in DFT simulations, this buckling can be controlled through application of moderate strains of $\leq 10\%$, which are achievable in the current 2D experiments [123, 124]. A similar system showing such tunability is $LaOBiS_2$ [125]. In addition to mechanical strains, the electric polarization (direction of buckling) can be switched as PbS is ferroelectric. And thus PbS spin texture can be switched in a non-volatile way which is similar to recently found ferroelectric Rashba semiconductors (FERSC) GeTe [126, 126]. Further, we also found orbital-spin texture switching in buckled PbS. Our results suggest that the orbital-spin switching at the Dirac point is not exclusive to TIs and the orbital texture is not always polarized, as it depends on the crystal symmetry of the material. Our unifying framework based on tight binding provides design principles and orbital-spin texture manipulations which will be important for development of new devices.

Chapter 6

Strain-induced Gauge and Rashba Fields in Ferroelectric Rashba Lead Chalcogenide PbX (X=S, Se, Te)

One of the exciting features of two-dimensional (2D) materials is their electronic and optical tunability through strain engineering. In the previous chapter we have introduced a new class of 2D ferroelectric Rashba semiconductors PbX (X=S, Se, Te) with tunable spin-orbital properties. In this chapter, based on our previous tight-binding (TB) results, we derive an effective low-energy Hamiltonian around the symmetry points that captures the effects of strain on the electronic properties of PbX. We find that strains induce gauge fields which shift the Rashba point and modify the Rashba parameter. This effect is equivalent to the application of in-plane magnetic fields. The out-of-plane strain, which is proportional to the electric polarization, is also shown to modify the Rashba parameter. Overall, our theory connects strain and spin-splitting in ferroelectric Rashba materials, which will be important to understand the strain-induced variations in local Rashba parameters that will occur in practical applications.

The work presented in this chapter (with some modifications) has been published in:

- **P. Z. Hanakata**, A. S. Rodin, H. S. Park, D. K. Campbell, A. H. C. Neto, "Strain-induced gauge and Rashba fields in ferroelectric Rashba lead chalcogenide monolayers PbX monolayers (X=S, Se, Te)" *Physical Review B* 97 (23), 235312 (2018). (2016).

6.1 Introduction

Monolayers and heterostructures of two-dimensional (2D) materials with spin-orbit interaction offer promise for observing many novel physical effects [19, 97, 127]. In particular, it has been proposed that topological insulators or semiconductors with Rashba interactions coupled with superconductors may host Majorana fermions, which are potential building blocks for topological quantum computers [33, 34].

In addition to 2D materials that exist in the hexagonal phase, such as graphene and the transition metal dichalcogenides (TMDs), 2D materials with square lattices have been successfully fabricated [116, 128]. Recently, the Rashba effect has been observed in thin layers (6–20 nm) of lead sulfide (PbS) [128], where an external electric field is used to break the inversion symmetry. However, the spin-splitting is not large. In our previous work based on density functional theory (DFT) calculations, we found that lead chalcogenide monolayers PbX (X=S, Se, Te) have large Rashba coupling $\lambda \sim 1$ eVÅ in their non-centrosymmetric buckled phase [35]. In addition, the spin texture can be switched in a non-volatile way by applying an electric field or mechanical strain, which puts these materials into the family of ferroelectric Rashba semiconductors (FERSCs) [108, 126]. This spin-switching mechanism has recently been observed experimentally in thin films GeTe where the surface is engineered to have either an inward or outward electric polarization [129].

In reality, monolayers experience strains due to substrates, defects, and so on, where local strains may change the electronic properties of monolayers. Important

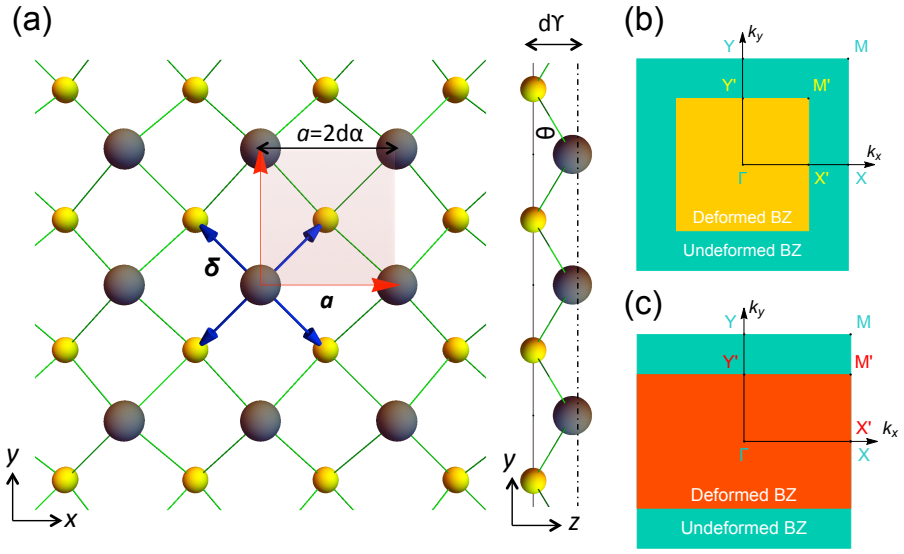

Figure 6.1: (a) Schematic top and side views of a buckled AB monolayer. (b) Undeformed and deformed Brillouin zone as the monolayer is stretched in the x and y direction.

examples of such effects are pseudo-Landau levels in graphene blisters [10] and band gap shifts in biaxially strained MoS_2 [130]. Recently, spatial variations of Rashba coupling due to variations in local electrostatic potentials were reported in InSb [131]. To date, most theoretical studies of lead chalcogenide monolayers have been based solely on DFT calculations [103, 115]. However, because DFT is limited to the simulation of small systems, typically several nanometers, it is difficult to model inhomogeneous strains over large spatial areas using DFT.

In this paper, based on our previous tight-binding (TB) model [35, 36], we develop a continuum model to predict strain-induced changes in the spin and electronic properties of buckled PbX monolayers. We have also performed DFT calculations to validate our TB predictions. Due to the buckled structure of PbX, the angular dependence becomes important as the relative angle between hybrid orbitals of the top and bottom layer can change substantially [35]. We note that some studies on (non-buckled) SnTe and PbX (X=S, Se, Te) rock-salt type materials have incorpo-

rated strain effects in the TB, but did not include the changes in hopping parameters due to angle changes [132, 133]. In contrast, our TB formulation incorporates the effects due to changes in (i) bond distance and (ii) angle between nearest neighbors as well as (iii) lattice vector deformation.

In the low-energy Hamiltonian, the biaxial (or uniaxial) strains can be described as gauge fields, which are equivalent to, by minimal coupling, the application of in-plane magnetic fields. The out-of-plane strain is directly related to the out-of-plane polarization and this also modifies the Rashba parameter. Within this framework we are able to quantify the Rashba fields in terms of the strain fields.

6.2 Computational Details

To validate our tight-binding predictions we performed density functional theory (DFT) calculations implemented in the Quantum ESPRESSO package [82]. We employed projector augmented-wave (PAW) type pseudopotentials with Perdew-Burke-Ernzerhof (PBE) within the generalized gradient approximation (GGA) for the exchange and correlation functional with [117]. The Kohn-Sham orbitals were expanded in a plane-wave basis with a cutoff energy of 100 Ry and a charge density cutoff of 200 Ry. The cutoff was chosen following the suggested minimum cutoff in the pseudopotental file. A k-point grid sampling was generated using the Monkhorst-Pack scheme with 16×16×1 points [84]. A vacuum of 20 Å was used. The relaxed structures of PbS, PbSe, and PbTe were obtained by relaxing the ionic positions and the lattice vectors. A convergence threshold on total energy of 10^{-5} eV and a convergence threshold on forces of 0.005 eV/Å^{-1} were chosen. Lattice vectors are relaxed until the stress is less than 0.01 GPa. Our first-principles calculations show that the buckled phase of the PbX monolayer is more stable than the centrosymmetric planar phase [35], consistent with other DFT studies [115, 134]. Detailed discussions

on the bistable nature, ferroelectric properties and orbital-spin texture properties of lead chalcogenides can be found in our previous paper [35]. In the current work, the deformations (atomic distortions) are applied to the optimized buckled structure.

We used a finer grid for band structure calculations with the spin-orbit interaction included. We have tried several large numbers of k points and found that a grid of 100 k points between two symmetry points (e.g between X and M) is enough to obtain the Rashba parameter λ at the M point [35]. A regular grid of 40×40×1 was used for the surface plot of the energy spin splitting.

Here we tabulate the optimized (relaxed) geometrical parameters of buckled PbX (X=S, Se, and Te) monolayers in table 6.1. The Rashba parameters λ are obtained by taking the derivative of energy dispersion near the M point. The orbital coefficients are obtained by projecting the wave functions into the atomic orbital basis. The unstrained values of λ and Δ are tabulated in table 6.2. From the table it can be seen that the wave functions are mostly composed of in-plane and out-of-plane of p orbitals of Pb and an in-plane orbital of the chalcogen X (X=S, Se, Te).

Table 6.1: Relaxed lattice constant a, buckling angle θ, buckling height d_z, nearest-neighbor bond distance d.

	a(Å)	θ(°)	d_z(Å)	d(Å)
PbS	3.74	21.6	1.04	2.84
PbSe	3.82	24.3	1.22	2.96
PbTe	4.01	26.3	1.40	3.16

Table 6.2: Rashba parameters λ, projected wave functions coefficients $|c_0|^2$, $|c_1|^2$, $|c_2|^2$ obtained from DFT and Δ.

	$\lvert c_0\rvert^2$	$\lvert c_1\rvert^2$	$\lvert c_2\rvert^2$	λ(eVÅ)	Δ (eV)
PbS	0.305	0.534	0.115	3.40	5.36
PbSe	0.272	0.549	0.137	3.37	4.28
PbTe	0.286	0.522	0.130	3.18	3.83

6.3 Tight-binding

Lead chalcogenide PbX (X=S, Se, Te) consists of two atoms per unit cell, denoted by A and B atoms, respectively. Lead is a heavy atom (Z(Pb)=82), and it is crucial for creating large spin-orbit interaction (SOI). The schematic top and side views of a buckled AB lattice are shown in fig. 6.1(a). $\boldsymbol{a}$ is the unit lattice vector and $\boldsymbol{\delta}_j$ is the vector connecting atom i and its j neighbor. We denote the relaxed bond length between the neighboring A and B atoms by d, the vector connecting A and B atoms in the $(0,0)$ unit cell $\boldsymbol{\delta}_1 = d(\alpha, \alpha, -\gamma)$ where $\alpha = \frac{\cos\theta}{\sqrt{2}}$, $\gamma = \sin\theta$, and θ is the buckling angle (with $\theta = 0$ corresponding to a flat lattice).

The bands near the Fermi level are mostly composed of s and p orbitals from both A and B atoms [35]. The bands near the symmetry points can be described within the TB framework including first nearest neighbors and SOI. We we will only outline the important parts; a more detailed derivation can be found in in chapter 4.

For the two atom AB unit cell shown in Fig. 6.1(a), the relevant orbital basis involves $\{s^A, p_x^A, p_y^A, p_z^A, s^B, p_x^B, p_y^B, p_z^B\}$. To write down the hopping matrix, we use the Slater-Koster matrix elements for the orbitals of neighboring atoms [96]. As we include the SOI, $H_{\text{SOI}} = T_{\mathcal{X}} \left(\frac{L_+ \otimes s_- + L_- \otimes s_+}{2} + L_z \otimes s_z \right)$ (where $\mathcal{X} = A, B$), we will write our Hamiltonian in angular momentum basis. The dimension of the total Hilbert space is 16×16 with new basis of $|\mu\rangle \to |m\rangle|m_{\text{orb}}\rangle|s\rangle$, where $m = \{|A\rangle, |B\rangle\}$ is the sublattice degree of freedom, $m_{\text{orb}} = \{|0,0\rangle, |1,1\rangle, |1,-1\rangle, |1,0\rangle\}$ is the orbital angular momentum degree of freedom, and $s = \{(|+\rangle, |-\rangle\}$ is the spin degree of freedom.

We found a Rashba-like dispersion near the Γ and M points when the two sublattices are not equivalent [35, 36]. In this paper, we develop a continuum strain model describing changes in the Rashba dispersion near the M point, and thus the Hamiltonian is expanded around the M point $\mathbf{k} = (\pi/a, \pi/a)$. Exactly at M $[q = 0]$,

the Hamiltonian decomposes into several uncoupled blocks and the wave function of the conduction band is given by $|\Psi^{\pm}\rangle_{mn} = c_0|m\rangle \otimes |1, \pm 1\rangle \otimes |\mp\rangle + c_1|m\rangle \otimes |1, 0\rangle \otimes |\pm\rangle \pm ic_2|n\rangle \otimes |1, \mp 1\rangle \otimes |\mp\rangle$, with c_0, c_1, and c_2 being real numbers [35, 36]. The Hamiltonian for the valance band can be obtained by interchanging m and n.

Projecting the Hamiltonian onto the conduction band subspace we obtain the effective Rashba-like Hamiltonian

$$H_{\text{eff}}^{mn} = \lambda \left[(\mathbf{q} \times \boldsymbol{\sigma}) \cdot \hat{z} \right] : \begin{pmatrix} |\Psi^{+}\rangle_{mn} \\ |\Psi^{-}\rangle_{mn} \end{pmatrix} , \tag{6.1}$$

where $\mathbf{q}$ is the momenta, $\boldsymbol{\sigma} = (\sigma_x, \sigma_y, \sigma_z)$, $\lambda \equiv a \sin 2\theta \Delta c_1 c_2$ is the Rashba parameter, and $\Delta = V_{pp\sigma} - V_{pp\pi}$. The coefficients c_0, c_1, c_2 can be obtained from the DFT calculations. Since we know the buckling angle θ we can can evaluate Δ. All of the relevant (unstrained) parameters are tabulated in Appendix 6.2.

6.4 Strain-induced Gauge Fields

Since the SOI is independent of lattice distortions, in this derivation we will focus on the spinless Hamiltonian and then reintroduce the spin terms. We will focus on the conduction band only, as the changes in valence band should be similar.

Under deformation a vector connecting two points in a unit cell i can be approximated as

$$\boldsymbol{r}'_j - \boldsymbol{r}'_i \simeq \boldsymbol{\delta}_j + \boldsymbol{\delta}_j \cdot \nabla \boldsymbol{u}(\boldsymbol{r}_i), \tag{6.2}$$

where $\boldsymbol{u} = (u_x, u_y, u_z)$ is the displacement vector, and $\nabla \boldsymbol{u} = \tilde{\boldsymbol{\epsilon}} + \tilde{\boldsymbol{\omega}}$. The strain tensor component ϵ_{ij} is given by

$$\epsilon_{ij} = \frac{1}{2}\left(\frac{\partial u_i}{\partial x_j} + \frac{\partial u_j}{\partial x_i} + \frac{\partial u_l}{\partial x_i} \frac{\partial u_l}{\partial x_j} \right). \tag{6.3}$$

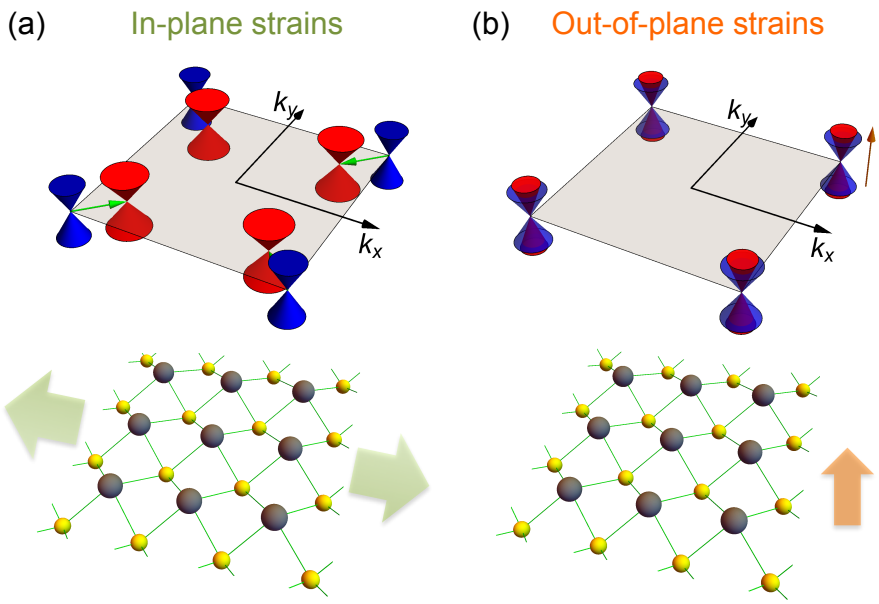

Figure 6.2: Schematic changes in the Rashba dispersions due to (a) in-plane strains and (b) out-of-plane strains. The linear Rashba dispersions at the M for unstrained systems are colored blue. Under positive in-plane strains, the Rashba points shift closer to Γ and the strength of Rashba parameters decrease (smaller slope) with increasing strains. On the other hand, under out-of-plane strain, the strength of Rashba parameters increases with increasing uniaxial out-of-plane strain while the Rashba points do not shift.

In this work we focus on deformation that does not involve local rotation $\tilde{\boldsymbol{\omega}} = 0$. Similarly, between two lattice vectors

$$\boldsymbol{R}'_j - \boldsymbol{R}'_i \simeq \boldsymbol{a}^i + \boldsymbol{a}^i \cdot \nabla \boldsymbol{u}(\boldsymbol{R}_i). \tag{6.4}$$

Alterations in bond distance will result in changes in the hopping energies. Since studies of lead chalcogenides under strain are very limited, we follow the Wills-Harrison's argument [135] and assume that the hopping energy $t \propto r^{-\beta_{\mu\nu}}$. Similar considerations also have been used for strained TMDCs [136, 137, 138] and phosphorene [139, 140]. Note that the hopping matrix derived from Slater-Koster has angular dependence and these relative angles should change due to strain. Assuming

the hopping matrix depends on bond distance only, the modified hopping parameter, in terms of the strain tensor $\tilde{\boldsymbol{\epsilon}}$ [136, 137], is

$$t'_{ij,\mu\nu}(\delta_{ij}) \simeq t_{ij,\mu\nu}(1 - \beta_{\mu\nu}\frac{1}{d^2}\boldsymbol{\delta}_j \cdot \tilde{\boldsymbol{\epsilon}} \cdot \boldsymbol{\delta}_j), \tag{6.5}$$

This approximation is also the case for graphene, where the hopping modulation is approximated as $t'(\boldsymbol{\delta}_{ij}) = te^{-\beta(|\boldsymbol{\delta}_{ij}|/d-1)}$. In particular, this approximation works well for *flat* graphene under strain because the angle between p_z orbitals does not change. The angular dependence becomes more important when deformations, such as nanobubbles and kirigami patterns, create large curvature (bending) [141, 142]. In buckled lead chalcogenides, however, the relevant hopping terms for the Rashba dispersion depend on the buckling angle even in the simple case of biaxial strains [35]. Thus we will include this angular dependence, and we will show that this is important to capture the changes in Rashba coupling with uniaxial strain.

Let the unstrained vector connecting an atom A and its neighbor be defined as $\boldsymbol{\delta}_j = (x, y, z)$ and the equilibrium distance $r = d$. Here we show the derivation for $t_{p_xp_z}$, while the others can be found by following the same procedure. We assume $\Delta(r') = \Delta_0 \left(\frac{r}{r'}\right)^\beta$ and we expect $\beta \approx 3$ [135]. In Cartesian coordinates the strained hopping is given by

$$t_{p_xp_z}(x', y', z') = \frac{x'z'}{r'^2}\Delta_0 \left(\frac{r}{r'}\right)^\beta, \tag{6.6}$$

and by Taylor expansion we obtain,

$$\begin{aligned}\delta t_{ij,p_xp_z}(x', y', z') \simeq - t_{ij,p_xp_z}(x, y, z)\Big(&\Big[(2+\beta) - (r/x)^2\Big]\frac{1}{r^2}\mathbf{x}\cdot(\mathbf{x}'-\mathbf{x}) \\ &- \Big[2+\beta\Big]\frac{1}{r^2}\mathbf{y}\cdot(\mathbf{y}'-\mathbf{y}) \\ &- \Big[(2+\beta) - (r/z)^2\Big]\frac{1}{r^2}\mathbf{z}\cdot(\mathbf{z}'-\mathbf{z})\Big).\end{aligned} \tag{6.7}$$

Within the strain approximation

$$\begin{aligned}\mathbf{x}' - \mathbf{x} =& \hat{x} \cdot \tilde{\boldsymbol{\epsilon}} \cdot \boldsymbol{\delta}_j \\ \mathbf{y}' - \mathbf{y} =& \hat{x} \cdot \tilde{\boldsymbol{\epsilon}} \cdot \boldsymbol{\delta}_j \\ \mathbf{z}' - \mathbf{z} =& \hat{x} \cdot \tilde{\boldsymbol{\epsilon}} \cdot \boldsymbol{\delta}_j \end{aligned} \tag{6.8}$$

If we alter only the bond distance while keeping the angle constant, we will get the same expression as above when angular effects are assumed to be negligible.

The interlattice-spinless Hamiltonian in reciprocal space can be written as

$$\begin{aligned} H^{\text{int}}_{\text{orb}}(\mathbf{k}) =& \sum_{\mu,\nu} \sum_{\langle ij \rangle} (t_{ij,\mu\nu} + \delta t_{ij,\mu\nu}) e^{i\mathbf{k}\cdot\boldsymbol{\Delta}_j(1+\tilde{\boldsymbol{\epsilon}})} c^\dagger_{i,\mathbf{k},\mu} c_{j,\mathbf{k},\nu} + h.c. \\ =& \underbrace{\sum_{\mu,\nu} \sum_{\langle i,j \rangle} t_{ij,\mu\nu} e^{i\mathbf{k}\cdot\boldsymbol{\Delta}_j} c^\dagger_{i,\mathbf{k},\mu} c_{j,\mathbf{k},\nu}}_{H_0} + \underbrace{\sum_{\mu,\nu} \sum_{\langle i,j \rangle} i t_{ij,\mu\nu} \mathbf{k} \cdot \tilde{\boldsymbol{\epsilon}} \cdot \boldsymbol{\Delta}_j e^{i\mathbf{k}\cdot\boldsymbol{\Delta}_j} c^\dagger_{i,\mathbf{k},\mu} c_{j,\mathbf{k},\nu}}_{H^{(1)}} + \end{aligned} \tag{6.9}$$

$$\underbrace{\sum_{\mu,\nu} \sum_{\langle i,j \rangle} \delta t_{ij,\mu\nu} e^{i\mathbf{k}\cdot\boldsymbol{\Delta}_j} c^\dagger_{i,\mathbf{k},\mu} c_{j,\mathbf{k},\nu}}_{H^{(2)}} + \mathcal{O}(\epsilon^2), \tag{6.10}$$

where $\langle ij \rangle$ is the sum over nearest neighbor pairs and $\boldsymbol{\Delta}_j = \mathbf{R}_j - \mathbf{R}_i$. The first term H_0 is the unstrained Hamiltonian, $H^{(1)}$ is the correction due to lattice deformation, and $H^{(2)}$ is the correction from the altered hopping parameter due to changes in both the interatomic distance and angle between orbitals.

6.5 Homogenous Isotropic Strains

We start with a simple deformation with no shear

$$\tilde{\boldsymbol{\epsilon}} = \begin{pmatrix} \epsilon_{xx} & 0 & 0 \\ 0 & \epsilon_{yy} & 0 \\ 0 & 0 & \epsilon_{zz} \end{pmatrix}. \tag{6.11}$$

We will focus on the matrix elements that are relevant to the conductions band, such as $|A\rangle|1,0\rangle$ and $|B\rangle|1,1\rangle$. In the *angular momentum* basis, the correction from $H^{(1)}$ and $H^{(2)}$ at M is given by

$$\begin{aligned} {}_A\langle 1,0|H^{(1)}|1,1\rangle_B =& a_0\sqrt{2}\alpha_0\Delta_0\gamma_0\Big[\epsilon_{xx}\pi/a_0 + q_x\epsilon_{xx} - i\epsilon_{yy}\pi/a_0 - iq_y\epsilon_{yy}\Big] \\ {}_A\langle 1,0|H^{(2)}|1,1\rangle_B =& -a_0\sqrt{2}\alpha_0\gamma_0\Delta_0\alpha_0^2(2+\beta)\Big[(\epsilon_{xx} \\ & + f_1\epsilon_{yy} + f_2\epsilon_{zz})q_x - (f_1\epsilon_{xx} + \epsilon_{yy} + f_2\epsilon_{zz})iq_y\Big] \end{aligned} \tag{6.12}$$

where,

$$f_1 = 1 - \frac{1}{\alpha_0^2(2+\beta)} \quad \text{and} \tag{6.13}$$

$$f_2 = \frac{\gamma_0^2}{\alpha_0^2} - \frac{1}{\alpha_0^2(2+\beta)}. \tag{6.14}$$

Note that $a_0, \alpha_0, \beta_0, \gamma_0, \Delta_0$ are the *unstrained* geometrical and hopping parameters. $H^{(1)}$ is independent of the z direction strains (e.g ϵ_{xz}) because the lattice vector $\mathbf{R}$ and $\mathbf{k}$ are two-dimensional. Because of the symmetry of M, we found that the first correction at M due to bond alterations is first order in ϵ *and* momentum q. In graphene, the first correction from hopping modulation that is linear in ϵ (but not proportional to q) is not zero [143, 144, 145]. We have to include the contributions of $H^{(1)}$ up to first order in q as well because in $H^{(2)}$ (β-dependent term) we keep terms up to first order in q and ϵ.

To obtain β we will consider an isotropic strain $\epsilon \cdot 1_{3\times 3}$. Notice that the change in

low-energy Hamiltonian of Eq. 6.1 due to $H^{(1)}$ and $H^{(2)}$ at M can be written as gauge potentials,

$$H_{\text{eff}} = -i\lambda_0 \begin{pmatrix} 0 & (q_x - iq_y) + \boldsymbol{A}_1 + \boldsymbol{A}_2 \\ (q_x + iq_y) + \boldsymbol{A}_1^* + \boldsymbol{A}_2^* & 0 \end{pmatrix}. \tag{6.15}$$

where,

$$\boldsymbol{A}_1 = \begin{pmatrix} \epsilon\pi/a_0 + \epsilon\, q_x \\ -i\epsilon\pi/a_0 - i\epsilon\, q_y \end{pmatrix} \quad \text{and} \tag{6.16}$$

$$\boldsymbol{A}_2 = -\beta \begin{pmatrix} \epsilon\, q_x \\ -i\epsilon\, q_y \end{pmatrix} \tag{6.17}$$

where we have used $2\alpha_0^2 + \gamma_0^2 = 1$ to simplify $\boldsymbol{A}_1, \boldsymbol{A}_2$ and λ_0 is the unstrained Rashba parameter.

$\boldsymbol{A}_2$ and the second term of $\boldsymbol{A}_1$ are *proportional* to q. This modifies the strength of Rashba parameter

$$\frac{\lambda}{\lambda_0} - 1 \simeq (1 - \beta)\epsilon. \tag{6.18}$$

This alteration in the Rashba term is similar to the modification of Fermi velocity in graphene [144, 145, 146].

We next present our DFT results to validate our TB predictions. Strains are applied to the relaxed buckled phase. In order to find the effects that come from changes in bond distance only, we deformed the monolayer in the DFT simulations by changing the bond distance while keeping the angle constant. The lattice vectors and atomic positions are not relaxed under this deformation. The Rashba parameters λ are obtained by taking the derivative of the energy dispersion in the vicinity of the M point, $|q| < 0.1\pi/a$. Under isotropic deformations, we found that λ at M decreases with increasing strain (weakening of the hopping interaction), as expected from Eq. 6.15, shown in fig. 6.3(a)-(c). A direct comparison between DFT results and TB with strain-included allows us to extract β. By

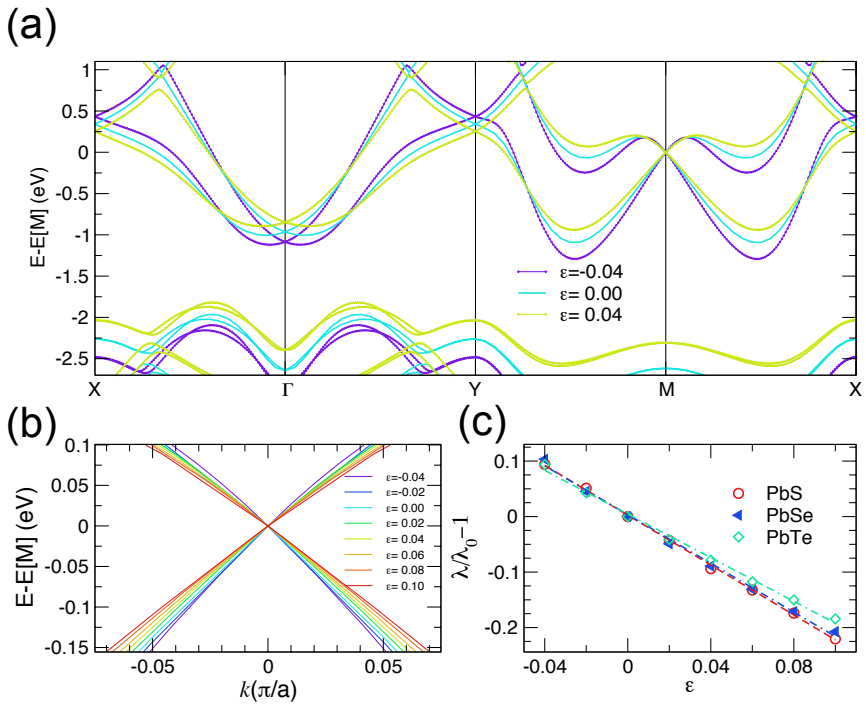

Figure 6.3: (a) Representative band structures of strained PbS along symmetry points X-Γ-Y-M-X and (b) close to M. (c) Relative change in the Rashba parameters obtained from DFT calculations as a function of strain ϵ for PbS, PbSe, and PbTe.

fitting DFT data points to a straight line, we obtained $\beta = 3.25, 3.20, 2.97$ for PbS, PbSe, and PbTe, respectively (fig. 6.3(c)). We see that the value of β would be different if the lattice deformation correction was not included.

As we stretch the lattice, the Brillouin zone (BZ) will shrink, and the corner of the BZ (M point) will shift as

$$\begin{aligned}\left(\frac{\pi}{a_0}, \frac{\pi}{a_0}\right) &\rightarrow \left(\frac{\pi}{a_0(1+\epsilon)}, \frac{\pi}{a_0(1+\epsilon)}\right) \\ &\simeq \left(\frac{\pi}{a_0}(1-\epsilon), \frac{\pi}{a_0}(1-\epsilon)\right), \end{aligned} \tag{6.19}$$

where a_0 is the undeformed lattice constant. For positive strains, the M point shifts towards the Γ point (relative to the undeformed BZ), shown in fig. 6.1(b). In our modified TB

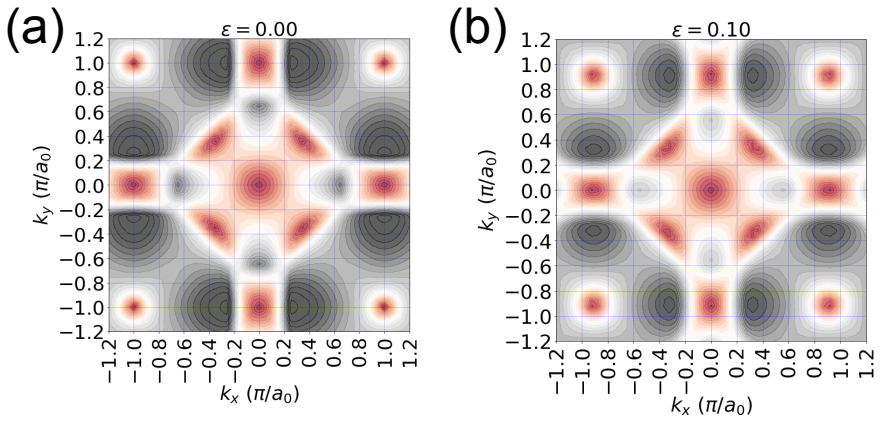

Figure 6.4: Energy spin-splitting of PbS for isotropic strains of (a) $\epsilon = 0.00$ and (b) $\epsilon = 0.10$. It can be seen that the M points are originally located at $|k_{x,y}| = \pi/a_0$ and shifted closer to the center under a strain of $\epsilon = 0.10$.

model, the M point is displaced due to the first term of the lattice deformation correction $\boldsymbol{A}_1$ (see Eq. 6.15). The momentum shifts due to lattice deformations are also found in graphene [147]. The changes in Rashba dispersion and its locations due to strains are illustrated in fig. 6.2.

To show the momentum shifts relative to the undeformed (reference) state, we plot the energy spin-splitting at the conduction band of PbS obtained from the DFT results as a function of k_x, k_y, shown in fig. 6.4(a) and (b). Note that momenta are in units of π/a_0. Originally the M points are located at $|k_{x,y}| = \pi/a_0$ and are shifted closer to Γ ($|k'_{x,y}| \approx 0.9\pi/a_0$) when an isotropic strain of $\epsilon = 0.10$ is applied. The momentum shift is linear with strains $\mathbf{k}\cdot\tilde{\boldsymbol{\epsilon}}$, consistent with several previous works [145, 147]. This Rashba-point shift due to strains is equivalent to applying in-plane-magnetic fields $\mathbf{B}_{\text{ex}}$ to the system,

$$H = \lambda_0 \left[\left(\mathbf{q} - \frac{e\mathbf{A}_{\text{ex}}}{c} \right) \times \boldsymbol{\sigma} \right] \cdot \hat{z} + m_\perp \sigma_z B_\perp + m_\parallel \mathbf{B}_\parallel \cdot \sigma_\parallel \tag{6.20}$$

where $m_\perp = -\mu_B(c_1^2 - 2c_2^2)$, $m_\parallel = -\mu_B c_1(\frac{c_0}{\sqrt{2}} + c_1 + c_0)$, and μ_B is the Bohr magneton. For completeness the derivation of Eq. 6.20 can be found in section 4.4. As an illustration, we can choose an external field of $\mathbf{A}_{\text{ex}} = (0, 0, B_x y - B_y x)$, upon which the in-plane magnetic

field is given by $\mathbf{B}_{\text{ex}} = \nabla \times \mathbf{A}_{\text{ex}} = (B_x, B_y, 0)$. Since the Bohr magneton is small, in order to get a similar effect of 2% strain using magnetic fields, one has to apply external magnetic fields with an approximate strength of $|B_{\text{ex}}| \sim \frac{\sqrt{2}\,0.02\,\pi\lambda_0}{a_0\,m_{\|}} \approx 600$ Tesla (by Eq. 6.15 and Eq 6.20).

6.6 Electric Polarization and Rashba Field

Proposals have been made to change the spin texture (i.e. sign of λ) by changing the electric polarization [121, 125, 126, 148]. Rinaldi *et al.* found that the spin-texture in FERSC GeTe films indeed depends on the locations of the atoms on the surface, which dictate the direction of the electric polarization [129]. In DFT simulations of SnTe thin films, which have a structure similar to PbX, it also has been shown that near the vacuum one of the atomic species buckles outward while the other species buckles inward [149]. While the proportionality between Rashba parameter and spontaneous electric polarization is well known, it will be useful to understand this mechanism in PbX from a microscopic view, where the changes in Rashba parameters can be understood in terms of interactions between atoms and the external applied strains. We will show that our strain-dependent TB model captures how the out-of-plane strain, which is proportional to the out-of-plane polarization, modifies the Rashba fields.

We used the modern theory of polarization [85] to calculate the electric polarization as described in the previous chapter. The spontaneous polarization is calculated by taking the difference between the polarization of the polar (buckled) state and the non-polar (reference) state, $\Delta\vec{\mathcal{P}} = \vec{\mathcal{P}}_{\text{polar}} - \vec{\mathcal{P}}_{\text{non-polar}}$.

To find the polarization at different heights, we change the out-of-plane distance between the Pb and X (X=S, Se) atom while keeping the in-plane lattice vectors fixed at the optimized buckled values. It is a common practice to use a value on the order of the bulk lattice constant (0.5–1 nm) to estimate the monolayer thickness in order to compare the polarizations of monolayers to the typical bulk ferroelectrics [32, 118, 119]. Accordingly,

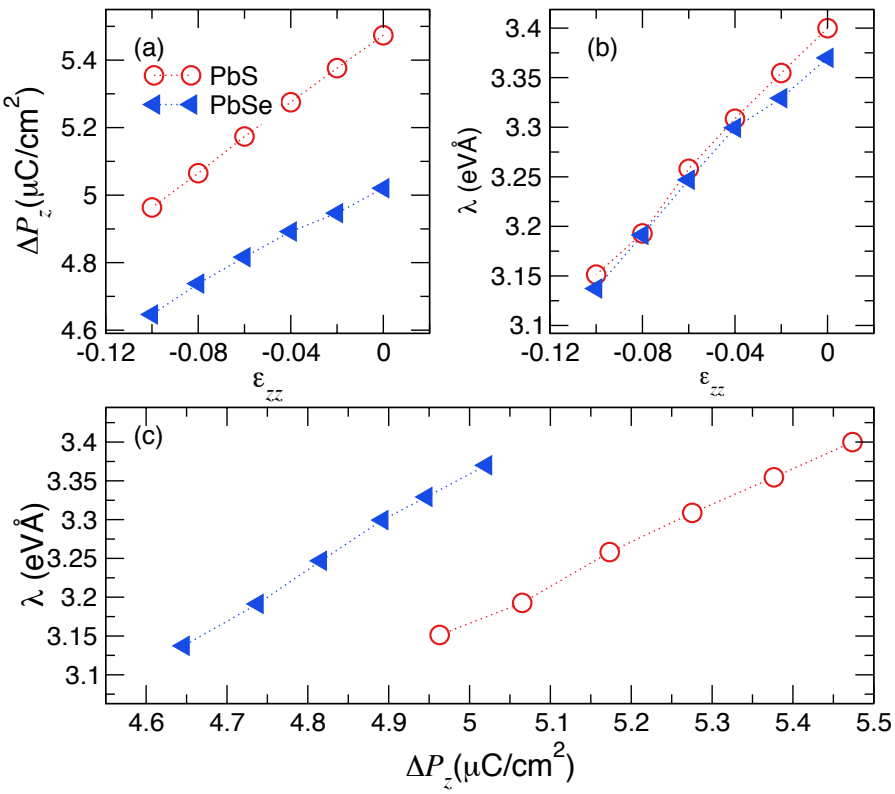

Figure 6.5: (a) Out-of-plane polarization $\Delta\vec{\mathcal{P}}_z$ as a function of out-of-plane strain ϵ_{zz}. (b) Linear relationship between λ and ϵ_{zz} which is consistent with TB predictions. (c) Rashba parameter λ as a function of $\Delta\vec{\mathcal{P}}_z$. All data points are obtained from the DFT calculations.

we approximate the thickness to be 0.5 nm in order to compare the polarizations to typical bulk ferroelectrics. In this current work we estimate the thickness to be 0.5 nm. In QUANTUM ESPRESSO, spontaneous polarization with spin-orbit included can be calculated using norm conserving pseudopotentials. A difference of 0.03 μC/cm^2 is found when spin-orbit interaction is included. Thus, to save computational time we only report spontaneous polarization without inclusion of the spin-orbit interaction. This small difference has also been reported previously [148, 150]. In figure. 6.6 we plot the polarization from the ionic plus core electron contribution, and the electronic contribution, from the Berry phase calculation, scaled by their values at zero strain as a function of distance between the Pb and S atom in the z direction. We report only the spontaneous polarizations of

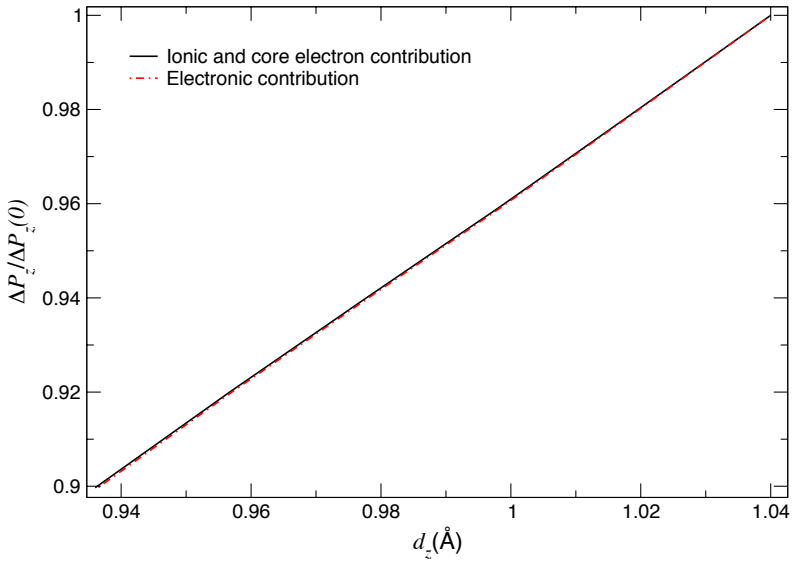

Figure 6.6: From the DFT results we found that the ionic plus core electronic and the electronic (by Berry phase calculation) contributions are proportional to the distance between Pb and X (X=S, Se) in the z direction.

PbS and PbSe, as PbTe is metallic [35]. A modified Berry phase calculation is needed to evaluate polarization of ferroelectric metals [151]; however this is beyond the scope of our present study.

From the DFT results we found that the core electronic plus ionic and the electronic contribution (BP) are proportional to the distance between Pb and X (X=S, Se) in the z direction (see fig. 6.6). This gives a proportionality between $\Delta\vec{\mathcal{P}}_z$ and ϵ_{zz}, as shown in fig. 6.5(a). Compressing the monolayer in the $\hat{z}$ with strain $\epsilon_{zz} < 0$ results in a decrease in λ, shown in fig. 6.5(b). This is *opposite* to the case of isotropic deformation (see fig. 8.1(e)). This result is consistent with TB predictions. In the previous discussion, we found that increasing bond distance ($\epsilon > 0$) generally weakens the hopping interaction and thus decreases λ. Using relaxed geometrical parameters (i.e buckling angle θ_0) and from Eq. 6.12, λ is expected to decrease with compressive strain in the $\hat{z}$ as f_2 is negative.

We also want to note that there is no gauge-field $\boldsymbol{A}_1$ since $\mathbf{k}$ is two-dimensional, and thus M is not shifted. The changes in Rashba dispersion and its locations due to out-of-plane strains are illustrated in fig. 6.2(b). Notice that not including the angular dependence in the hopping correction will not capture this effect. The inclusion of the angular dependence is particularly important for the PbX monolayer due to its buckled nature. Overall, this suggests that the out-of-plane internal electric polarization acts as an in-plane gauge field in the low-energy Hamiltonian. Assuming *small* strains, we found that $\lambda \propto |\vec{\mathcal{P}}_z|$. This result is important as it establishes a direct relationship between the Rashba field and the out-of-plane polarization which is also proportional to the out-of-plane strain ϵ_{zz}. Recently, several works have also studied strain-induced piezoelectricity in boron nitride [152] and TMDCs [153]. Several experimental works use out-of-plane magnetic fields (parallel to the polar axis of Rashba materials) to measure the Rashba parameter as the Landau level spectrum changes with the strength of the Rashba parameter [99, 131]. One could also use this experimental approach to detect variations in the Rashba parameter in PbX due to out-of-plane strains.

6.7 Summary

We have developed a TB model where the electronic changes in PbX can be described within continuum mechanics. We found the scaling exponent that modifies the hopping parameter to be $\beta \simeq 3$. In the low-energy Hamiltonian, the effect of strains can be described as gauge fields, which are equivalent to, by minimal coupling, application of an in-plane magnetic field. Our theory describes how the location of the Rashba point and the strength of the Rashba field can be engineered by applying strains. The out-of-plane strain in particular is directly related to the out-of-plane polarization. Within this framework we are able to understand the connection between the Rashba and ferroelectricity.

Our strain-dependent TB model should be applicable for calculating the effects of inhomogeneous strain on the spatially-resolved Rashba fields over a large region, whereas

this calculation would not be feasible within a reasonable time using a DFT approach. Employing classical atomistic simulations (e.g. molecular dynamics) together with strain-dependent TB will be an efficient tool for studying larger and more realistic systems with strain modulation due to substrates, indentors [10, 130, 154] or geometrical cuts [142, 155].This will open possibilities of using lead chalcogenides for strain and electric-controlled spintronic devices.

Chapter 7

Kirigami and actuators

In the last few chapters we have shown the importance of DFT methods to investigate fundamental properties of 2D materials. We then developed a continuum model to describe electronic changes due to local strains. Due the large surface ratio, properties of 2D materials can be altered substantially via defects. In the last two chapters we will focus on studies of changes in mechanical properties of 2D materials due to cuts.

In this chapter, we utilize molecular dynamics (MD) simulations to study defects in 2D materials. MD approach is needed because the studied novel devices usually have sizes ranging from nano- to micrometer. We report the results of classical molecular dynamics simulations focused on studying the mechanical properties of MoS_2 kirigami. Several different kirigami structures were studied based upon two simple non-dimensional parameters, which are related to the density of cuts, as well as the ratio of the overlapping cut length to the nanoribbon length. Our key finding is significant enhancements in tensile yield (by a factor of four) and fracture strains (by a factor of six) as compared to pristine MoS_2 nanoribbons. These results in conjunction with recent results on graphene suggest that the kirigami approach may be a generally useful one for enhancing the ductility of two-dimensional nanomaterials.

The work presented in this chapter (with minimal modifications) are parts of the following published papers:

- **P. Z. Hanakata**, Z. Qi, D. K. Campbell, H. S. Park,
  "Highly stretchable MoS 2 kirigami", *Nanoscale* 8 (1), 458-463 (2016).

7.1 Introduction

Molybdenum disulfide (MoS_2) has been intensely studied in recent years as an alternative two-dimensional (2D) material to graphene. This interest has arisen in large part because (i) MoS_2 exhibits a direct band gap of nearly 2 eV in monolayer form which is suitable for photovoltaics [156]; and (ii) it has recently been explored for many potential applications, ranging from energy storage to valleytonics [12, 63, 64, 65].

The mechanical properties of MoS_2 have also been explored recently, through both experimental [2, 157, 158] and theoretical methods [3, 4, 159, 160]. That MoS_2 has been reported experimentally to be more ductile than graphene [2] naturally raises the critical issue of developing new approaches to enhancing the ductility of 2D materials.

One approach that has recently been proposed towards this end is in utilizing concepts of kirigami, the Japanese technique of paper cutting, in which cutting is used to change the morphology of a structure. This approach has traditionally been applied to bulk materials and recently to micro-scale materials [161, 162, 163], though recent experimental [28] and theoretical [142] works have shown the benefits of kirigami for the stretchability of graphene.

Our objective in the present work is to build upon previous successes in applying kirigami concepts to graphene [142] to investigate their effectiveness in enhancing the ductility of a different 2D material, MoS_2, which is structurally more complex than monolayer graphene due to its three-layer structure involving multiple atom types. We accomplish this using classical molecular dynamics (MD) with a recently developed Stillinger-Weber potential [1]. We find that kirigami can substantially enhance the yield and fracture strains of monolayer MoS_2, with increases that exceed those previously seen in monolayer graphene [142].

7.2 Methods

We performed MD simulations using the Sandia-developed open source code LAMMPS [164, 165] using the Stillinger-Weber potential for MoS_2 of Jiang [1]. All simulations were per-

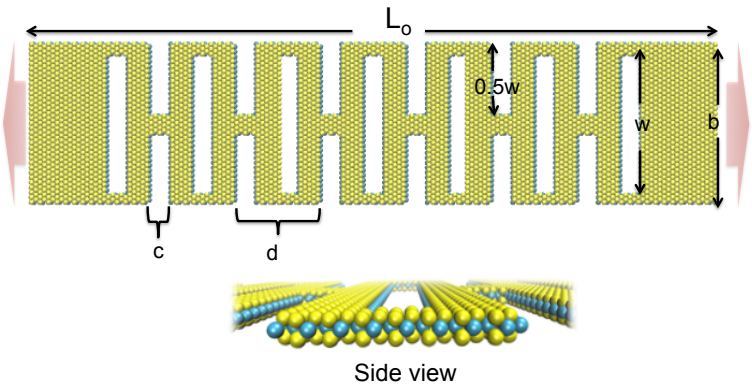

Figure 7.1: (Color online) Schematic of the MoS_2 kirigami, with key geometric parameters labeled. The kirigami is deformed via tensile displacement loading that is applied at the two ends in the direction indicated by the arrows. Top image represents a top view of the kirigami.

formed on single-layer MoS_2 sheets. Of relevance to the results in this work, we note that while the Stillinger-Weber potential does not have a term explicitly devoted to rotations, it does contain two and three-body terms including angular dependencies, which is important for out-of-plane deformations. Furthermore, the Stillinger-Weber potential of Jiang [1] was fit to the phonon spectrum of single-layer MoS_2, which includes both in and out-of-plane vibrational motions. As a result, the Stillinger-Weber potential should do a reasonable job of capturing out-of-plane deformations that involve angle changes, such as rotations.

The MoS_2 kirigami was made by cutting an MoS_2 nanoribbon, which had free edges without additional surface treatment or termination. A schematic view of the kirigami structure and the relevant geometric parameters is shown in Fig. 7.1. The key geometric parameters are the nanoribbon length L_0, the width b, the height of each interior cut w, the width of each interior cut c, and the distance between successive cuts d. We considered kirigami for both zig-zag (ZZ) and armchair (AC) edges. A representative AC MoS_2 kirigami consisting a number of $N \sim 12,000$ atoms with a nanoribbon length $L_0 \sim 450$ Å, width $b \sim 100$ Å, height of each interior cut $w \sim 70$ Å, width of each interior cut $c \sim 11$ Å, and distance between successive cuts $d \sim 55$ Å is shown in Fig. 7.1.

The MD simulations were performed as follows. The kirigami was first relaxed for

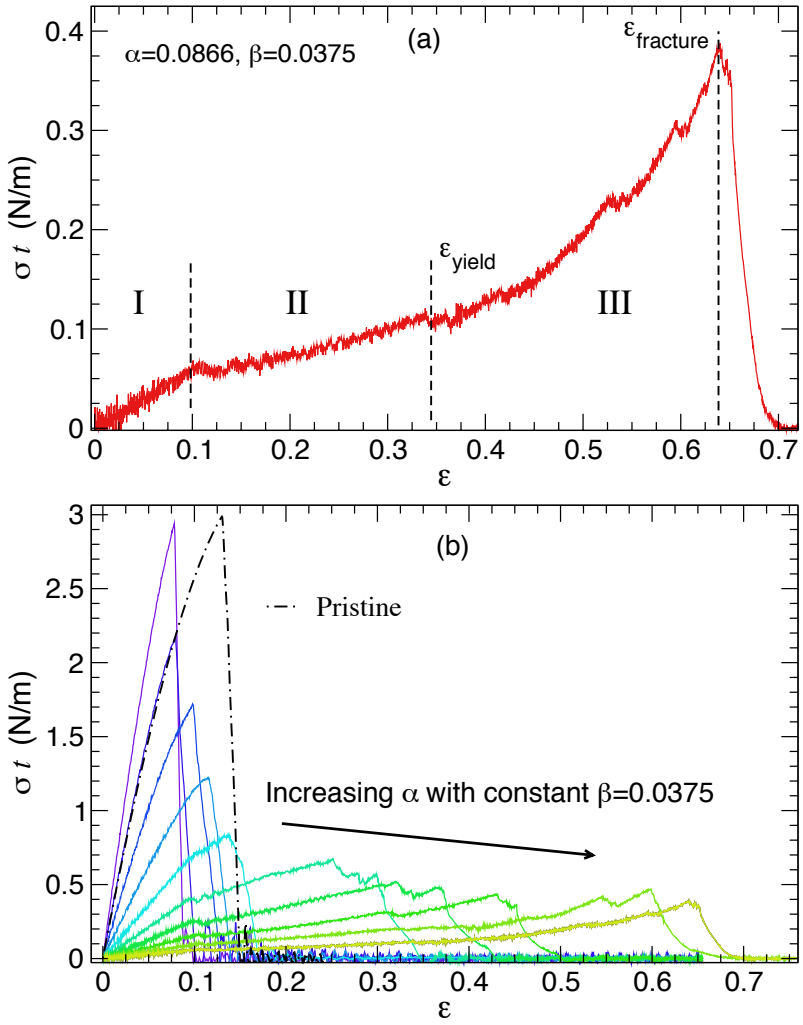

Figure 7.2: (Color online) Stress-strain curves of AC MoS_2 kirigami, where the 2D stress was calculated as the stress σ times thickness t. (a) Stress-strain curve for constant $\alpha = 0.0866$, $\beta = 0.0375$. (b) Stress-strain curve for AC kirigami keeping $\beta = 0.0375$ constant and varying α. Note the brittle fracture of the pristine MoS_2 nanoribbon. In general, the strain in region III increases substantially for $\alpha > 0$.

200 ps within the NVT (constant number of atoms N, volume V and temperature T) ensemble at low temperature (4.2 K), while non-periodic boundary conditions were used in all three directions. The kirigami was subsequently deformed in tension by applying uniform displacement loading on both ends, such that the kirigami was pulled apart until

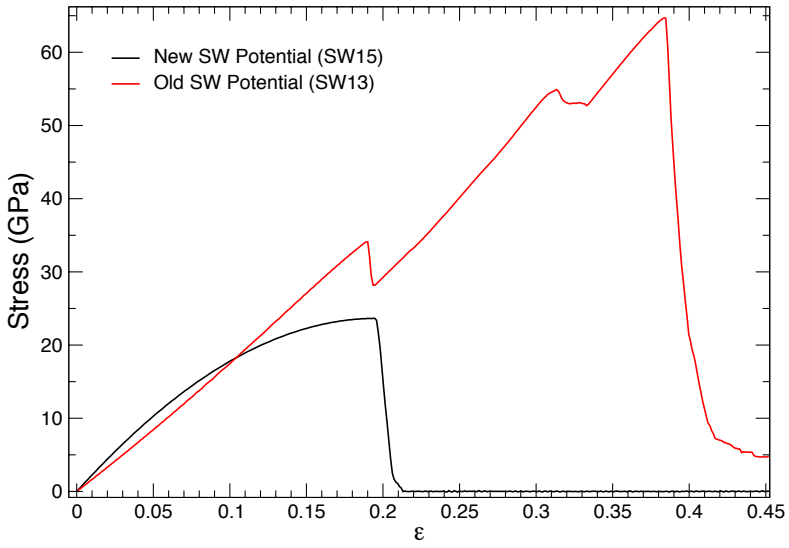

Figure 7.3: (Color online) Stress-strain curve of a monolayer MoS_2 sheet under tensile loading along the armchair direction using two different SW potentials. The newer SW potential [1] matches better with the trends observed in DFT calculations [2] than the first SW potential of Jiang et al. [3]. No phase transition is observed with the more recent SW potential of Jiang [1]. For SW13, breaking of bonds between the Mo and S layers occur at $\epsilon \sim 0.2$ and $\epsilon \sim 0.3$ as observed in Ref. [4]

fracture occurred. We note that in actual applications, the MoS_2 kirigami will likely lie on a substrate, and thus adhesive interactions with the substrate may impact the deformation characteristics. In the present work, we focus on the intrinsic stretchability of the MoS_2 kirigami while leaving the interactions with a substrate for future work.

We note that we have used the more recent Stillinger-Weber (SW15) potential of Jiang [1] rather than the earlier SW potential also developed by Jiang and co-workers [3] (SW13). This is because in comparing the tensile stress-strain curves, the SW15 potential more closely captured the trends observed in DFT calculations [2]. We have also performed simulations of many kirigamis, nanoribbons, and monolayer sheets using the old SW potential. We have found qualitatively similar results *with the very important differ-*

ence that the SW13 potential predicts a tensile phase transition in pristine nanoribbon and monolayer sheet [4] that is not observed in the SW15 potential [1]. A comparison of the tensile stress-strain curve for monolayer MoS_2 is shown in Fig. 7.3 for the potentials of Jiang (SW15) [1], and Jiang et al. (SW13) [3].

Table 7.1: Comparison of mechanical properties of MoS_2 sheets and pristine nanoribbons in the armchair (AC) and zigzag (ZZ) direction.

System	ϵ_f	σ_f^{3D}(GPa)	Y^{3D}(GPa)
Sheet (AC)	0.178	16.8	154.0
Sheet (ZZ)	0.175	15.6	150.7
NR (AC)	0.130	14.6	145.8
NR (ZZ)	0.129	13.6	130.0

In addition, we simulated MoS_2 sheets (defined as monolayer MoS_2 with periodic boundary conditions in the plane) and pristine nanoribbons with no cuts for comparative purposes. The calculated fracture strains ϵ_f, fracture stresses σ_f^{3D}, and Young's modulus Y^{3D} are tabulated in Table 7.1. The results are in reasonably good agreement with the experimental and first-principles studies of MoS_2 monolayer sheets [2, 157]. In the previous table, 3D stresses σ_f^{3D} are calculated as σ_f^{2D}/t_h, where t_h is the effective thickness with a value of ~ 6 Å.

7.3 Results

In Figure 7.2 (a), we plot a representative stress-strain curve of MoS_2 kirigami. For this, and the subsequent discussion, we introduce two non-dimensional geometric parameters $\alpha = (w - 0.5b)/L_0$ and $\beta = (0.5d - c)/L_0$, which were also previously used to describe graphene kirigami [142]. α represents the ratio of the overlapping cut length to the nanoribbon length, while β represents the ratio of overlapping width to the nanoribbon length. Put another way, α describes the geometry orthogonal to the loading direction, while β describes the geometry parallel to the loading direction. Figure 7.2(a) shows the stress-strain for the specific choices of $\alpha = 0.0866$, and $\beta = 0.0375$, which were obtained by choosing

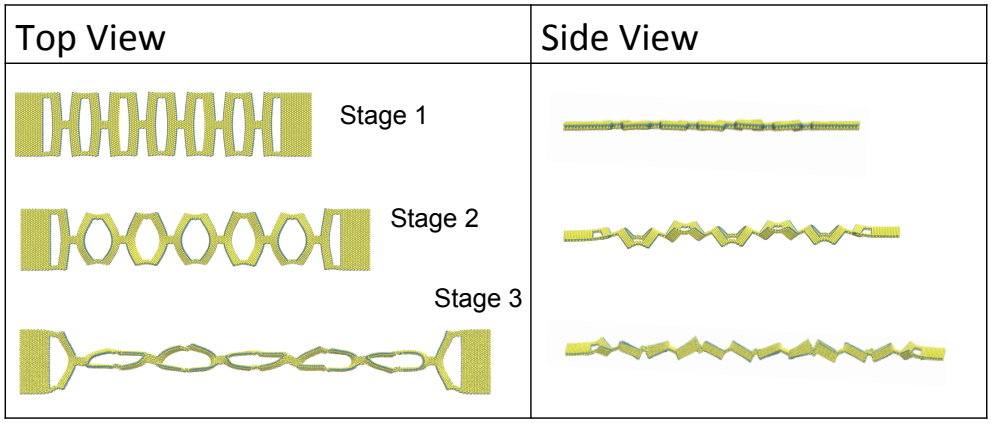

Figure 7.4: Side and top views of kirigami during deformation.

b=101.312 Å, L_0=438.693 Å, w=88.648 Å, c=10.967 Å, and d=54.837 Å. In contrast, Figure 7.2(b) shows the change in the stress-strain response if $\beta = 0.0375$ is kept constant while α changes. This is achieved by changing w while keeping other geometric parameters constant. We also note that the 2D stress was calculated as stress times simulation box size perpendicular to the plane $\sigma \times t$ to remove any issues in calculating the thickness [159], where the stress was obtained using the virial theorem, as is done in LAMMPS.

It can be seen that there are generally three major stages of deformation for the kirigami, as separated by the dashed lines in Fig. 7.2(a). In the first stage (region I), the deformation occurs via elastic bond stretching, and neither flipping nor rotation of the monolayer MoS_2 sheet is observed as shown in Fig. 7.4. In previous work, it was found that graphene kirigami rotates and flips in the first stage instead of bond stretching [142]. This does not occur for kirigami in MoS_2 in this first stage because the bending modulus of MoS_2 is nearly seven times higher than that of graphene [159].

In the second stage (region II), for tensile strains (ϵ) exceeding about 10%, further strain hardening occurs. Kirigami patterning allows the MoS_2 monolayer to exhibit out-of-plane deflections, as shown in Fig. 7.4, which allows the MoS_2 monolayer to undergo additional tensile deformation, which is in contrast to the brittle fracture observed for the pristine nanoribbon immediately following the initial yielding event as shown in Fig. 7.2(b). Furthermore, the out-of-plane deflections cause the slope of the stress-strain curve in region II

to be smaller than that in region I. This is because of the change in deformation mechanism

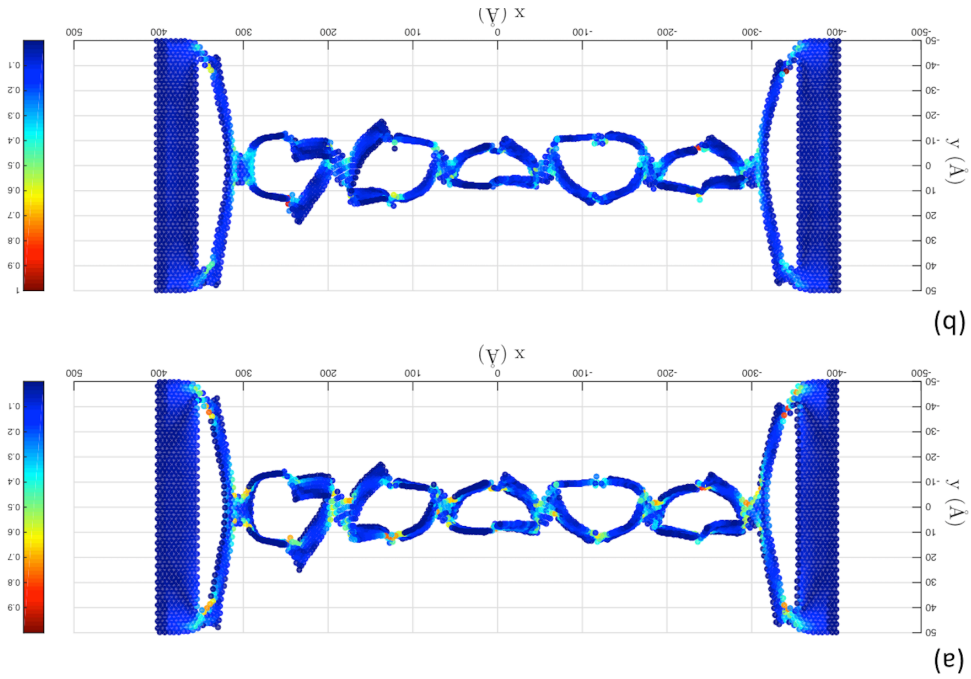

Figure 7.5: Von Mises stress prior to the fracture at a tensile strain of 62% in (a) Mo layer and (b) top S layer of kirigami in Fig. 7.4. We plot the stress distribution layer by layer to give a clear picture of the stress distribution. The von Mises stress were scaled between 0 and 1.

from purely elastic stretching of bonds in region I, to a combination of stretching and out of plane buckling in region II.

Local bond breaking near the edges starts to occur at the tensile strain of $\epsilon = 35\%$. The occurrence of bond breaking is usually defined as the yield point, and signifies the demarkation between regions II and III. This local bond breaking occurs due to the concentrated stress at the edges connecting each slab, as previously observed in graphene kirigami [142]. At this stage, each kirigami unit is held by a small connecting ribbon which allows the monolayer to be almost foldable. Fig. 7.4 (stages 1 to 3) shows how the inner cut surface area having initial area $w \times c$ and the height of the monolayer (largest out-of-plane distance between S atoms) can change significantly during the tensile elongation.

In the final stage, after more than 62.5% tensile strain, fracture and thus failure of the kirigami nanoribbon is observed. Unlike the pristine nanoribbon, the yield point can differ substantially from the fracture strain and the difference increases with increasing cut-overlap, which was described previously as shown in Fig. 7.2(b). Thus, it is important to quantify the yield point of the kirigami as it defines the beginning of the irreversible deformation regime. Note that these regions vary depending on the kirigami structure as shown in Fig. 7.2(b).

We also show, in Fig. 7.5, the von Mises stress distribution prior to fracture at a tensile strain of 62%. In Fig. 7.5, the stress values were scaled between 0 and 1, and the stress distributions in the top S layer and single Mo layer were plotted separately for ease of viewing as MoS_2 has a tri-layer structure. We found that the largest stresses are concentrated near the edges of the each kirigami unit cell similar to that previously observed in graphene kirigami [142].

Having established the general deformation characteristics for MoS_2 kirigami, we now discuss how the yield and failure characteristics are dependent on the specific kirigami geometry. We discuss the yield and fracture stresses and strains in terms of the two geometric parameters α and β that were previously defined.

The yield strain as a function of α is shown in Fig. 7.6(a), while the yield stress as a function of α is shown in Fig. 7.6(b). In these, and all subsequent figures, the stresses and strains are normalized by those for pristine MoS_2 nanoribbons of the same width such that the effect of the kirigami parameters can be directly quantified. As shown in Fig. 7.6, the MoS_2 kirigami becomes significantly more ductile for $\alpha > 0$, where the zigzag chirality reaches a yield strain that is about a factor of 6 larger than the pristine nanoribbon. In contrast, Fig. 7.6 (b) shows that the yield stress for kirigami correspondingly decreases dramatically for increasing α. We also note that the kirigami patterning appears to have a similar effect on the ductility of zigzag and armchair MoS_2 kirigami (shown in Fig. 7.6(a)) as the fracture strain and bending modulus of MoS_2 monolayer sheet in zigzag and armchair direction are similar [1, 159].

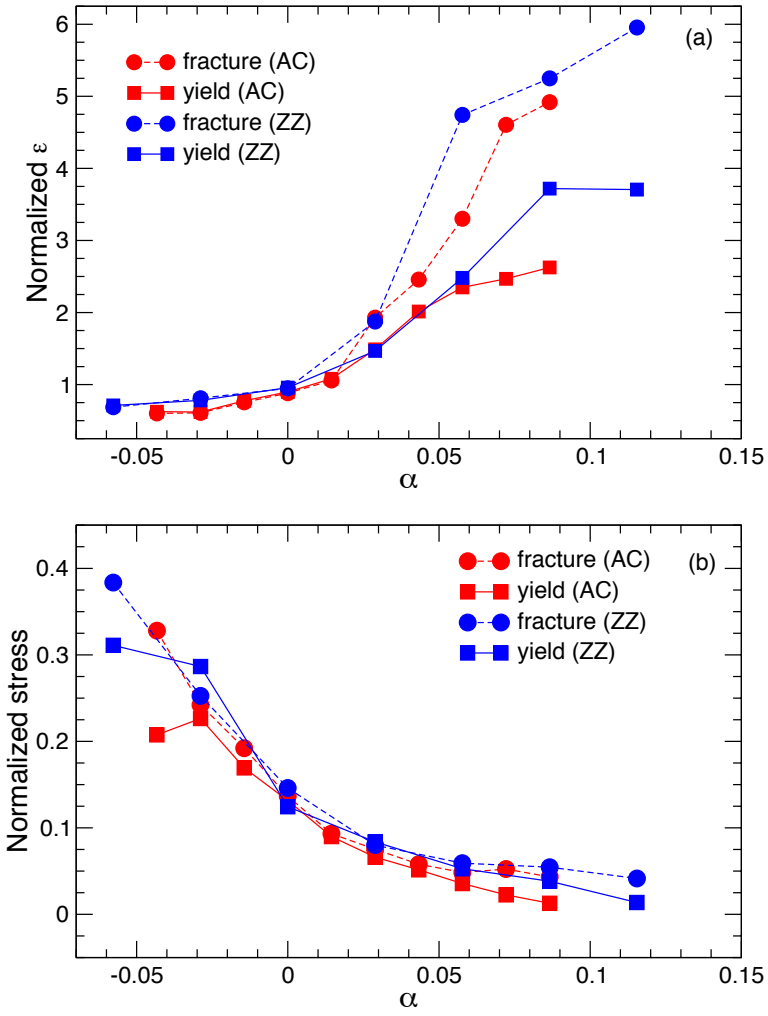

Figure 7.6: (Color online) (a) Influence of α on yield and fracture strain for zigzag (ZZ) and armchair (AC) MoS_2 kirigami, with constant $\beta = 0.0375$ for AC and constant $\beta = 0.0417$ for ZZ. (b) Influence of α on yield and fracture stress for zigzag (ZZ) and armchair (AC) MoS_2 kirigami. Data are normalized by MoS_2 nanoribbon results with the same width.

The increased ductility occurs because $\alpha = 0$ corresponds to the case when the edge and interior cuts begin to overlap. Increasing α above zero corresponds to when the edge and interior cuts do overlap, and thus it is clear that increasing the overlap increases the ductility of the MoS_2 kirigami. In contrast, the yield stress is higher for smaller α because for negative α, the edge and interior cuts do not overlap, and thus the deformation of the

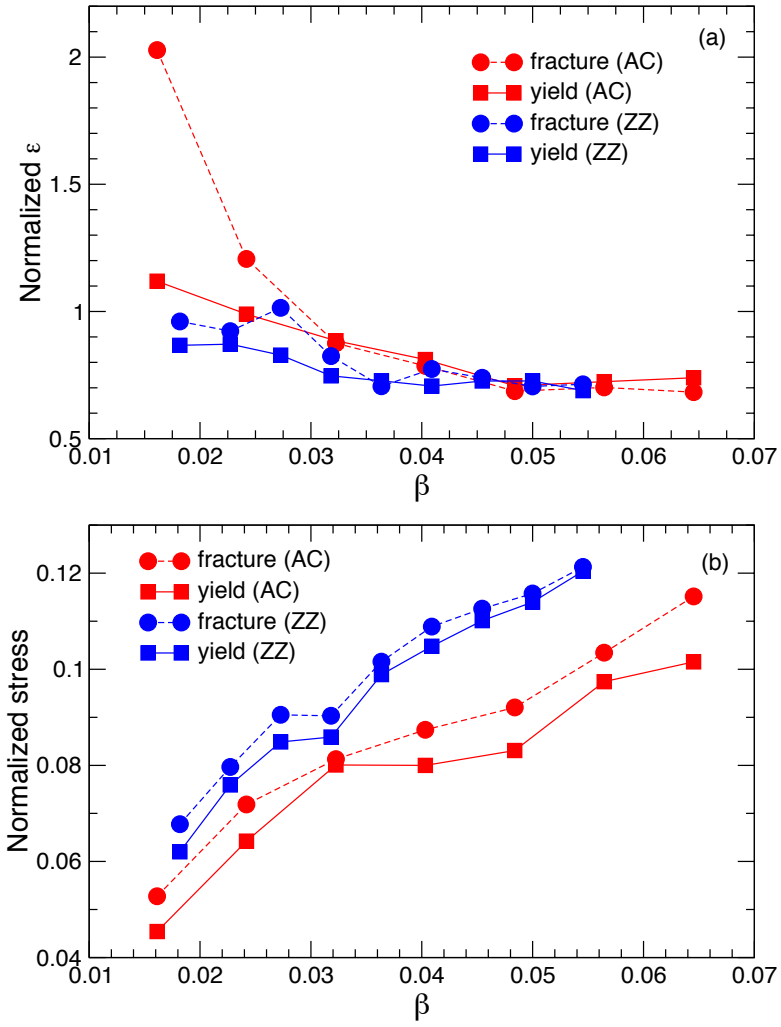

Figure 7.7: (Color online) Influence of β on the kirigami yield and fracture strain (a) and stress (b), with constant $\alpha = 0.0186$ for AC and constant $\alpha = 0.0157$ for ZZ. Data are normalized by MoS_2 nanoribbon results with the same width.

kirigami more closely resembles that of the cut-free nanoribbon.

In addition to the results of α, the effect of β on the kirigami ductility is shown in Figs. 7.7(a) and 7.7(b). Specifically, β is varied by changing d while keeping other geometric parameters constant. For both the yield stress and strain, β does impact the yield stress and strain. Increasing β corresponds to an increase in the overlapping region width, which thus results in a smaller yield strain, and increased yield stress as compared to a pristine

nanoribbon. For $\beta \geq 0.03$, we do not observe large differences between the AC and ZZ behavior in the case of varying β because increasing β (or decreasing the cut density) makes the kirigami more pristine, leading to similar values of fracture stress and strain in the AC or ZZ direction (see Table 7.1). Our results suggest that the failure strain can be maximized by increasing the overlapping cut (increasing α) and increasing density of the cuts (decreasing β).

Recently, Guo et al. showed stretchability of metal electrodes can be enhanced by creating geometries similar to the ones illustrated in Fig. 7.1 [163]. Adopting the geometric ratios determining fracture strain described in Ref. [163], we found similar trends: the fracture strain increases with decreasing $\frac{(b-w)}{c}$ and increases with increasing $\frac{b}{d}$. It is interesting to see that a similar trend is operant at a different length scale (an atomically-thin monolayer in this work as compared to a ≈40 nm thin film in the work of Guo et al.), and for a different material system (MoS_2 in this work, nanocrystalline gold in the work of Guo et al.), which suggests that the fracture strain in patterned membranes can be described entirely by geometric parameters.

It is also interesting to note that the yield and fracture strain enhancements shown in Fig. 7.6(a) exceed those previously reported for monolayer graphene kirigami [142]. The main reason for this is that the failure strain for the normalizing constant, that of a pristine nanoribbon of the same width, is smaller for MoS_2. As shown in Table 7.1, this value is about 13%, whereas the value for a pristine graphene nanoribbon was found to be closer to 30% [142]. However, the largest failure strain for the MoS_2 and graphene kirigami were found to be around 65%, so the overall failure strains for graphene and MoS_2 kirigami appear to reach similar values.

In addition to the yield and fracture behavior, we also discuss the elastic properties, or Young's modulus. For the kirigami system, we expect the Young's modulus to decrease with increasing width of the cut w due to edge effects [3]. Fig. 7.8 shows the dependence of Young's modulus with effective width $b_{\text{eff}} = b - w$. As can be seen for both armchair and zigzag orientations, the modulus decreases nonlinearly with decreasing effective width,

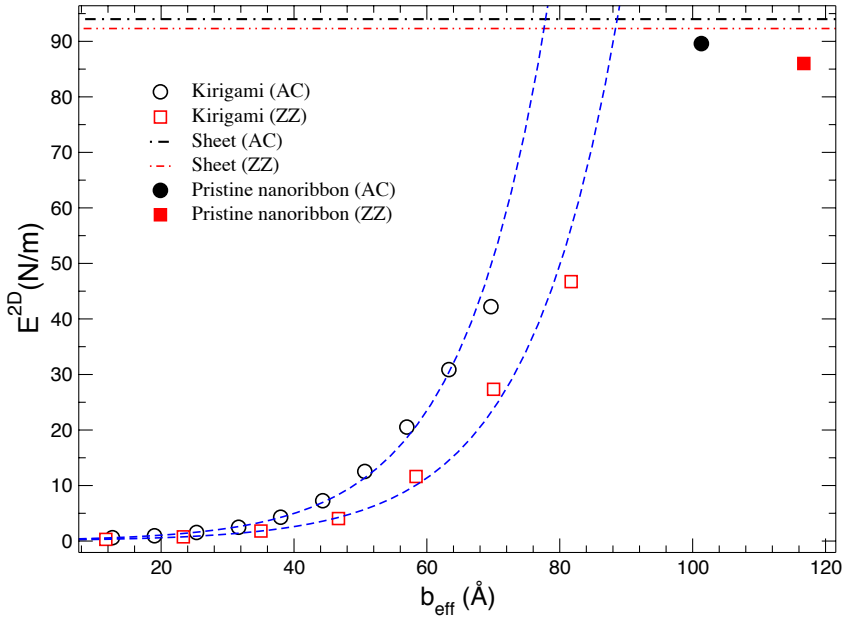

Figure 7.8: 2D Young's modulus E^{2D} of armchair (AC) and zigzag (ZZ) kirigami, pristine nanoribbons (PNR), and sheets. Inset shows E^{2D} of kirigami normalized by PNRs. The fitting dashed line (colored blue) is given as a guide to the eye.

reaching a value that is nearly 200 times smaller than the corresponding bulk value for the smallest effective width value we examined. Furthermore, the trend of the decrease differs from that previously seen in graphene nanoribbons based on first principles calculations [166] and MoS_2 nanoribbons based on atomistic simulations [3], where a significantly more gradual decrease in stiffness was observed. This is due to the fact that for a given nanoribbon width b, the kirigami has significantly more edge area than a nanoribbon, leading to significant decreases in elastic stiffness even for effective widths b_{eff} that are close to the corresponding nanoribbon width.

7.4 Summary

In summary, we have applied classical molecular dynamics simulations to demonstrate that the kirigami patterning approach can be used to significantly enhance the tensile

ductility of monolayer MoS_2, despite the much higher bending modulus and rather more complex tri-layer structure of MoS_2 compared to graphene. The resulting enhancements in tensile ductility are found to exceed those previously reported for graphene [142]. These results suggest that kirigami may be a broadly applicable technique for increasing the tensile ductility of two-dimensional materials generally, and for opening up the possibility of stretchable electronics and photovoltaics using monolayer MoS_2.

Chapter 8

Accelerated search and design of stretchable graphene kirigami using deep learning

In the previous chapter we have shown how kirigami-inspired cuts can be utilized to design stretchable materials with metamorphic properties where the 2D shape can transform into complex 3D shapes. However, finding the optimal solutions is not straightforward as the number of possible cutting patterns grows exponentially with system size. Using molecular dynamics (MD) to simulate *all* possible candidate designs would not be practical.

In this chapter, we introduce machine learning (ML) approach for topology optimization. ML can be used to approximate the target properties, such as yield stress and yield strain, as a function of cutting pattern. Our approach enables the rapid discovery of kirigami designs that yield extreme stretchability as verified by molecular dynamics (MD) simulations. We find that convolutional neural networks (CNN), commonly used for classification in vision tasks, can be applied for regression to achieve an accuracy close to the precision of the MD simulations. This approach can then be used to search for optimal designs that maximize elastic stretchability with only 1000 training samples in a large design space of $\sim 4 \times 10^6$ candidate designs. This example demonstrates the power and potential of ML in finding optimal kirigami designs at a fraction of iterations that would be required of a purely MD or experiment-based approach, where no prior knowledge of the governing physics is known or available.

The work presented in this chapter (with some modifications) has been published in:

- **P. Z. Hanakata**, E. D. Cubuk, D. K. Campbell, H. S. Park,
  "Accelerated search and design of stretchable graphene kirigami using machine learning", Physical review letters 121 (25), 255304 (2018)

8.1 Introduction

Recently, there has been significant interest in designing flat sheets with metamaterial-type properties, which rely upon the transformation of the original 2D sheet into a complex 3D shape. These complex designs are often achieved by folding the sheet, called the origami approach, or by patterning the sheet with cuts, called the kirigami approach. Owing to the metamorphic nature, designs based on origami and kirigami have been used for many applications across length scales, ranging from meter-size deployable space satellite structures [167] to soft actuator crawling robots [168] and micrometer-size stretchable electronics [28, 162].

Atomically thin two-dimensional (2D) materials such as graphene and MoS_2 have been studied extensively due to their exceptional physical properties (mechanical strength, electrical conductivity, etc). Based on experiments [28] and atomistic simulations [155, 169], it has been shown that introducing arrays of kirigami cuts allows graphene and MoS_2 to buckle in the direction perpendicular to the plane. These out-of-plane buckling and rotational deformations are key to enabling significant increases in stretchability.

By the principles of mechanics of springs, it is expected that adding cuts (removing atoms) generally will both soften and weaken the material. Griffith's criterion for fracture [170] has been successfully used to explain the decrease in fracture strength for a single cut [171, 172, 173, 174], but cannot explain how the delay of failure is connected to the out-of-plane deflection of kirigami cuts. Several analytical solutions have been developed to explain the buckling mechanism in single cut geometries [175, 176], a square array of mutually orthogonal cuts [177], and a square hole [178]. These analytical solutions are

applicable for regular repeating cuts, but may not be generally applicable for situations where non-uniform and non-symmetric cuts may enable superior performance.

An important, but unresolved question with regards to kirigami structures at all length scales is how to locate the cuts to achieve a specific performance metric. This problem is challenging to solve due to the large numbers of possible cut configurations that must be explored. For example, the typical size scale of current electronic devices is micrometers (10^{-6} meters) and the smallest cuts in current 2D experiments are about 10×10 Å [179]. Thus, exhaustively searching for good solutions in this design space would be impractical as the number of possible configurations grows exponentially with the system size. Alternatively, various optimization algorithms, i.e. genetic and greedy algorithms, and topology optimization approaches, have been used to find optimal designs of materials based on finite element methods [180, 181, 182, 183]. However, these approaches have difficulties as the number of degrees of freedom in the problem increases, and also if the property of interest lies within the regime of nonlinear material behavior.

Machine learning (ML) methods represent an alternative, and recently emerging approach to designing materials where the design space is extremely large. For example, ML has been used to design materials with low thermal conductivity [184], battery materials [185, 186], and composite materials with stiff and soft components [187]. ML methods have also recently been used to study condensed matter systems with quantum mechanical interactions [188, 189, 190], disordered atomic configurations [191, 192, 193] and phase transitions [46, 194]. While ML is now being widely used to predict properties of new materials, there have been relatively few demonstrations of using ML to design functional materials and structures [195].

In this letter, we use ML to systematically study how the cut density and the locations of the cuts govern the mechanical properties of graphene kirigami. We use fully-connected neural networks (NN) and also convolutional neural networks (CNN) to approximate the yield strain and stress. To formulate this problem systematically, we partition the graphene sheets into grids, where atoms in each grid region will either be present or cut, as shown

schematically in fig. 8.1. We then utilize the CNN for inverse design, where the objective is to maximize the elastic stretchability of the graphene kirigami subject to a constraint on the number of cuts. We use ML to search through a design space of approximately 4,000,000 possible configurations, where it is not feasible to simulate all possible configurations in a brute force fashion. Despite the size of the design space, our model is able to find the optimal solution with fewer than 1000 training data points (evaluations via MD). Our findings can be used as a general method to design a material without any prior knowledge of the fundamental physics, which is particularly important for designing materials when only experimental data are available and an accurate physical model is unknown.

8.2 Methods

8.2.1 Molecular Dynamics Methods

We used the Sandia-developed open source LAMMPS (Large-scale Atomic/Molecular Massively Parallel Simulator) molecular dynamics (MD) simulation code to model graphene [164]. The carbon-carbon interactions are described by the AIREBO potential [196], which has been used previously to study graphene kirigami [169]. The default values of AIREBO potentials are used. The cutoffs for the Lennard-Jones and the REBO term in AIREBO potential are chosen to be 6.8 Å and 2.0 Å (rcmax_CC in the CH.airebo potential file), respectively. The graphene sheet of size $\sim 100 \times 200$ Å consisting 2400 (9600 carbon atoms) rectangular graphene unit cells is shown in fig. 8.1. In the 15 grids (colored red), a cut of size 3×16 rectangular graphene unit cells (colored green) is allowed to be present or absent. The graphene kirigami were stretched by applying loads at the $+x$ and $-x$ edges of the sheet. The atomic configurations were first relaxed by conjugate gradient energy minimization with a tolerance of 10^{-7}. The graphene sheet was then relaxed at 4.2 K for 50 ps within the NVT (fixed number of atoms N, volume V, and temperature T) ensemble. Non-periodic conditions were applied in all three directions. After the NVT relaxation, the edge regions were moved at a strain rate of 0.01/ps, and the graphene sheet was stretched

until fracture. This particular strain rate was chosen to save computational time as it has

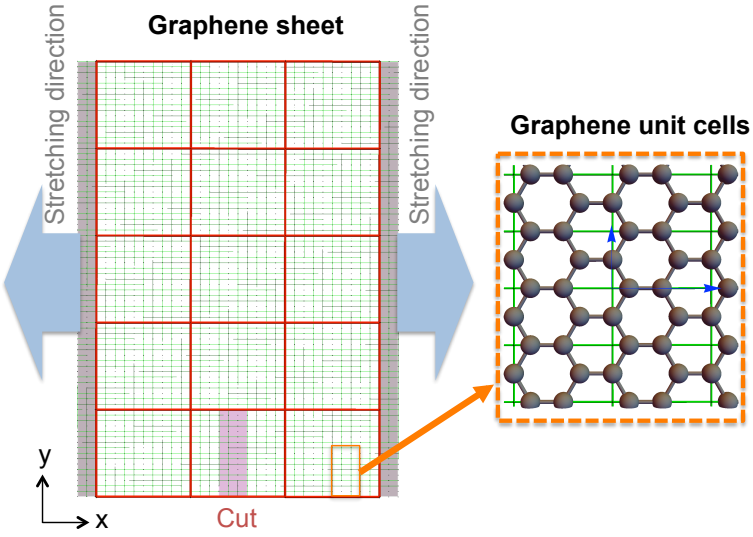

Figure 8.1: Schematic diagrams of graphene sheet and rectangular graphene unit cells. In this system, there are 3×5 grids (colored red) where a cut may present or absent. Each grid consist of 10×16 rectangular graphene unit cells (colored green) and each rectangular graphene unit cell consists of four carbon atoms

been shown that the fracture strain and fracture strength of graphene depend weakly on the strain rate, especially for low temperature [171]. The 3D stress was calculated as the stress parallel to the loading direction times the simulation box size perpendicular to the plane and divided by the graphene effective thickness of 3.7 Å. Similar procedures have been used for other MD, DFT simulations and experiments [32, 155, 172, 197, 198].

8.3 Machine Learning Methods and Molecular Dynamics Precision

We used open-source machine learning packages to build the machine learning models. Specifically, we used TensorFlow r1.8 [199] for both the neural networks (NN) and convolutional neural networks (CNN) model and scikit-learn [200] for the ordinary least square regression model. The TensorFlow r1.8 was run on four CPUs and one NVDIA Tesla K40m GPU card.

In convolutional neural netwrok model (CNN), we denote 'h' as the number of fully-connected-layers (FCL) and 'f' as the number of filters in a convolutional layer. So for a CNN model with 16 filters in first convolutional layer, 32 filters in second convolutional layer, 64 filters in third convolutional layer, and with a 64 FCL, we will denote is as CNN-f16-f32-f64-h64. For both NN and CNN, a learning rate of 0.0001 was used with a batch size of 200. The number of maximum epochs was set to 300. A larger learning rate, e.g 0.001, or smaller number total iteration number was found to have little effect on the performance. For the search algorithm CNN-f16-f32-f64-h64, a learning rate of 0.001 was used with a batch size of 100.

The root-mean-square error (RMSE) is given by,

$$\mathrm{RMSE} = \sqrt{\frac{\sum_{i=1}^{m_{\mathrm{test}}} (y_{\mathrm{test}}^{i} - y_{\mathrm{pred}}^{i})^2}{m_{\mathrm{test}}}} \tag{8.1}$$

where m_{test} is the number of test datasets, y_{test} are the true values (obtained from MD) from the test dataset, and y_{pred} are the predicted values from a model. Because of thermal fluctuations (non-zero temperature), the obtained yield strain or the yield stress of graphene from the MD simulations at 4.2 K will have some variation, which we will refer to as the MD precision. The MD precision (irreducible error) for the yield strain η^{ε} can be approximated as root-mean-square deviation (RMSD),

$$\eta^{\varepsilon} = \sqrt{\frac{\sum_{i=1}^{T} (\varepsilon_i^{\mathrm{y}} - \overline{\varepsilon^{\mathrm{y}}})^2}{T}}\,, \tag{8.2}$$

where T is the number of observations and $\overline{\varepsilon^{\mathrm{y}}}$ is the average of ε^{y} over T observations which in this case are the different initial velocities (different initial conditions). The same formula is used for the yield stress η^{σ}. η^{ε} is generally larger for systems with more cuts. To save computational time we randomly choose a configuration from systems having a cut density ranging from 0/15 to 12/15, calculate the RMSD from three different initial conditions, and then sum the RMSD of each cut. Note that cut densities of 13/15–15/15

are not considered because the structure is fully detached. For yield strain, the variability is more present at higher cut density and thus we sum the RMSD from cut densities ranging from 5/15 to 12/15.

8.4 Overview of mechanical properties

In this section, we give a brief overview of the changes in the mechanical properties of graphene with cuts. The 2D binary array of cut configurations $N_{\text{grid}} = N_x \times N_y$ is flattened into a one-dimensional array vector $\boldsymbol{x}$ of size $n = N_{\text{grid}}$. We use n for number of features, m for the number of samples, $\boldsymbol{x} = (x_1, x_2, ..., x_n)^T$ for the binary vector describing cut configurations, $\vec{x}, \vec{y}, \vec{z}$ for the real space vectors (atomic locations), and $\hat{x}, \hat{y}, \hat{z}$ for the unit vectors in real space.

We study one unit kirigami of size $\sim 100 \times 200$ Å, where cuts are allowed to be present on the 3×5 grid; this gives a design space of $2^{15} = 32768$ possible cut configurations (fig. 8.1), which we will refer to as the design space (or exploration space). Out of those, only 29791 configurations are not detached (no full cut along the $\hat{y}$ direction). Because the system is not periodic, translation symmetry is broken. The reflection symmetry is not broken and thus only about 1/4 of the possible configurations need to be simulated via MD. Each cell of the grid also consists of 10×16 rectangular graphene unit cells. There are 2400 rectangular graphene unit cells in this sheet; there are four carbon atoms in the rectangular graphene unit cell. This gives a total of 9600 carbon atoms in a kirigami sheet without cuts. In this system, the cut density can range from 0 cuts in the 15 grids to 15 cuts in the 15 grids, while keeping each cut size constant at 12×38 Å (3×16 rectangular graphene unit cells), which is relevant to current experimental capabilities [179].

We simulate graphene as the 2D constituent material of choice for the kirigami at a low temperature of 4.2 K to generate the ground truth data for our training model, Since we simulate MD at $T = 4.2$ K, the obtained yield strain (or stress) of a configuration varies due to stochasticity (i.e. distributions of the initial velocities). The MD precisions for strain

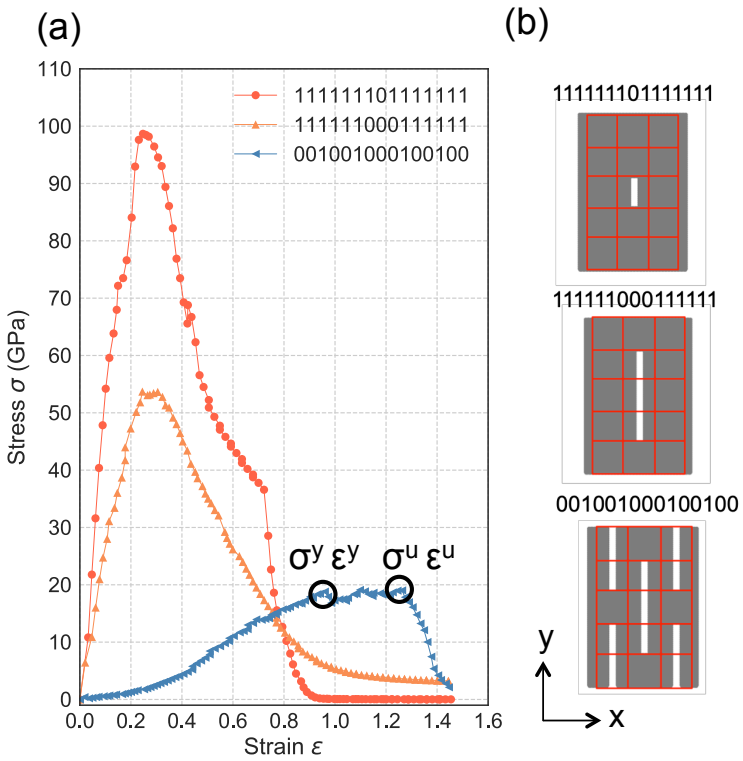

Figure 8.2: (a) Stress-strain plot of three representative"typical" kirigami cuts and the corresponding structures.

and stress are $\eta^{\varepsilon} = 0.046$ and $\eta^{\sigma} = 2.00$ GPa, respectively. In this work, we focus only on kirigami with armchair edges along the $\hat{x}$ direction as the stretchability is improved regardless of the chirality of graphene with armchair or zigzag edges [169]. The sheets are stretched in the $\hat{x}$ direction and engineering strain $\varepsilon = L/L_0 - 1$ is used to quantify stretchability, where L_0 and L are the length of sheet in the direction of the loading before and after the deformation, respectively.

Stress-strain curves of three representative cuts are shown in fig. 8.2(a). From the stress-strain curve we can identify the ultimate stress σ^{u} (and the corresponding strain ε^{u}), yield stress σ^{y}, and yield strain ε^{y}. Another point of interest is the failure point where the system is completely detached upon stretching. Here, we focus on the yield point where plastic deformation/bond breaking begins. Analyzing the amount of strain between yielding and the onset of failure would give insights into the post-yielding deformation mechanisms, and

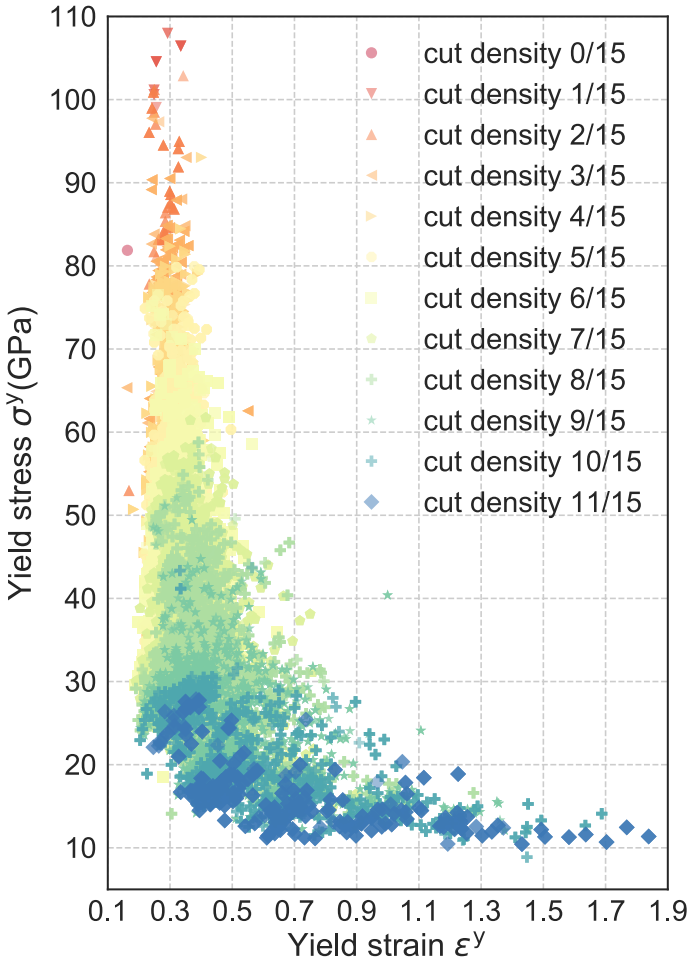

Figure 8.3: Yield stress as a function of yield strain for different configurations. Data are colored based on their cut density.

the role of kirigami structure in controlling the post-yield behavior, which could be done in a subsequent study. As shown in fig. 8.3, the σ^y consistently decreases with increasing number of cuts. ε^y has much more variability at higher cut density. At a cut density of 73% (11 cuts), ε^y varies over a wide range of values from $\sim$ 0.2 (20%) to $\sim$ 2.0 (200%). This shows that increasing number of cuts without intelligently locating the cuts may not always increase the stretchability.

8.5 Machine learning

8.6 Model, locality, and designs principles

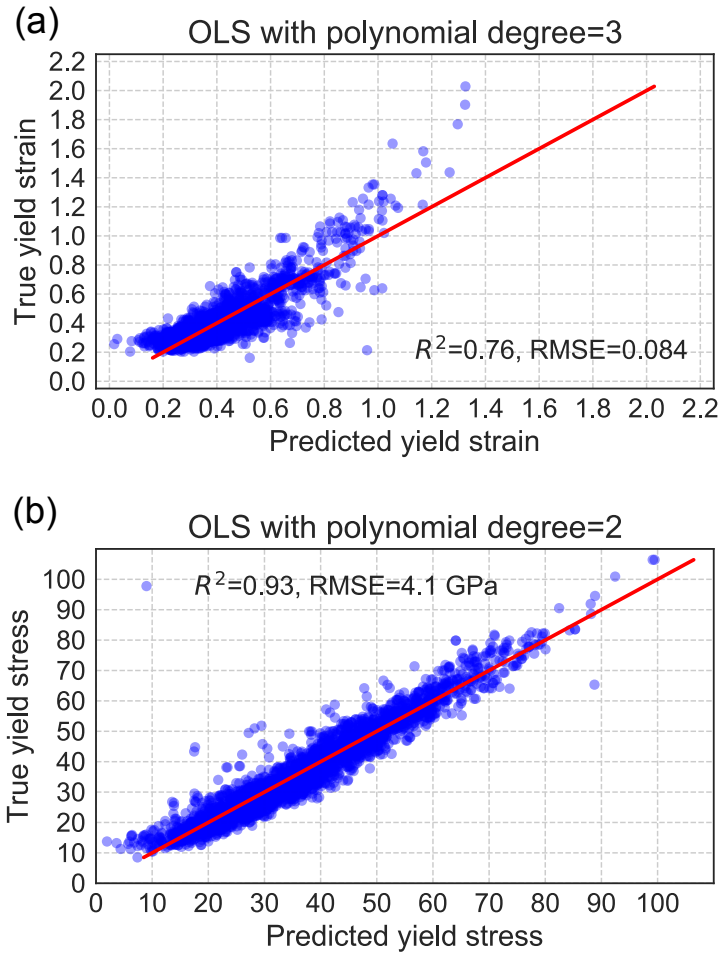

Figure 8.4: Linear plot of true values (test data) as a function of predicted value for (a) yield strain and (b) yield stress. The red line represents $y = x$ line.

We shall start our discussion of ML from a physics perspective. The Hamiltonian (or any physical quantity) of many physical systems in nature can be expanded as a power

series. We then formulate the objective functions, yield stress and strain, as

$$f(\boldsymbol{x}) = \beta_0 + \sum_i \beta_i x_i + \sum_{i \le j} \beta_{ij} x_i x_j + \sum_{i \le j \le k} \beta_{ijk} x_i x_j x_k + \dots . \tag{8.3}$$

For m samples, we can write Eq. 8.3 as a linear function $f(\boldsymbol{x}) = \mathbf{X^T} \cdot \boldsymbol{\beta}$, where

$$\mathbf{X}^T = \begin{pmatrix} 1 & x_1^{(1)} & \dots & x_n^{(1)} & x_1^{(1)} x_2^{(1)} & \dots \\ \vdots & \ddots & & & & \\ 1 & x_1^{(m)} & \dots & x_n^{(m)} & x_1^{(\mathrm{m})} x_2^{(m)} & \dots \end{pmatrix}, \tag{8.4}$$

and $\boldsymbol{\beta}^T = (\beta_0, \beta_1, \dots, \beta_n, \beta_{12}, \dots)$. In the machine learning language this is equivalent to applying features transformation to the input vectors. If the vector $\boldsymbol{x}$ is binary, the infinite series reduces into a finite series with 2^n terms. Symmetries and locality will further reduce number of β with nonzero values. For instance, in Ising and tight-binding models interactions are usually considered up to the first or second nearest neighbors. Moreover most physical systems, under certain conditions or constraints, can be described by a low order polynomial, usually less than a degree of four. We will start by approximating the objective function with a polynomial function.

Since there is no theory that tells us the degree of the complexity, we will increase the degree of polynomial until a reasonable performance accuracy is achieved. We use the ordinary least squares (OLS) regression to describe the yield stress as a function of $\boldsymbol{x}$. For this regression model we use the 15 long array that distinguishes between cut and no cut in each grid as the input vector $\boldsymbol{x}$ and set the value of each component to be '1' for no-cut and '-1' for cut.

Out of 2^{15} possible configurations, only the 29,791 non-detached configurations are considered. We find the non-detached configurations, where non-detached means that there is no cut that traverses the entire length (in the y-direction) of the kirigami. We randomly shuffle the 29,791 data samples, and use 80% for training, 10% for validation, and 10% for the test set. To quantify the performance of a model we use R^2 score on the

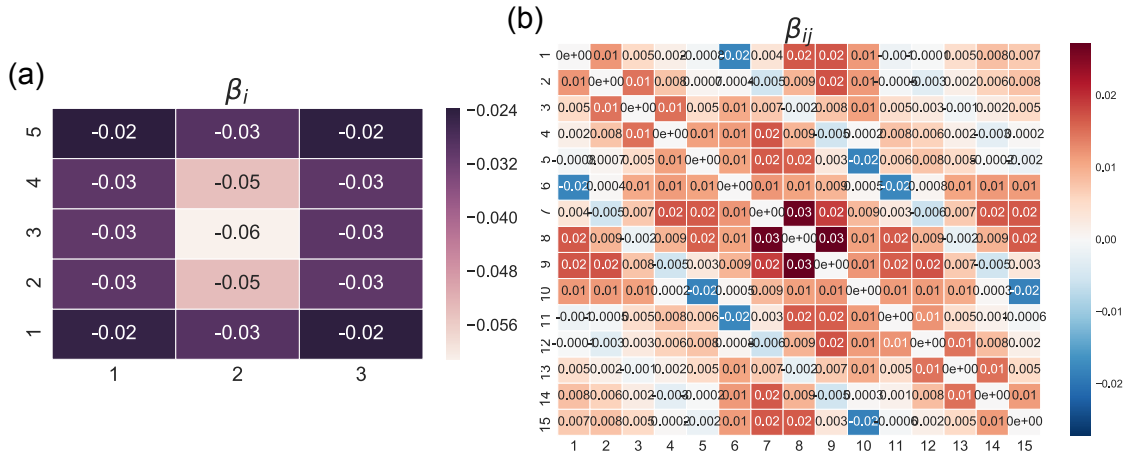

Figure 8.5: (a) Learned first order parameter β_i plotted in 2D arrays to match with the real space positions for yield strain. Here (1,1) is β_1, (1, 2) is β_2 and so on. (b) Learned matrix second order parameters (coupling interactions) β_{ij} for yield strain.

test set given by

$$R^2 = 1 - \frac{\sum_{i=1}^{m_{\text{test}}} |y^i_{\text{test}} - y^i_{\text{pred}}|^2}{\sum_{i=1}^{m_{\text{test}}} |y^i_{\text{test}} - \frac{1}{m_{\text{test}}} \sum_{i=1}^{m_{\text{test}}} y^i_{\text{pred}}|^2}\,, \tag{8.5}$$

where m_{test} is the number of test set, y_{test} are the true values (obtained from MD) from the test set, and y_{pred} are the predicted values from the model. Since we simulate MD at $T = 4.2$ K there will be stochasticity (non-deterministic) and thus the MD simulation results have irreducible error. The fundamental MD accuracy (irreducible error) $\eta^{\sigma(\varepsilon)}$ can be approximated as root mean squared deviations (RMSD) of σ^{y} (ε^{y}) obtained from different initial conditions, which in this case are the initial velocities. η is generally larger for systems with more cuts. For yield strain, a polynomial of degree 3 gives $R^2 = 0.76$ and RMSE = 0.084; for yield stress, a polynomial of degree 2 gives $R^2 = 0.93$ and root mean square error RMSE = 4.1 GPa. The plots are shown in fig. 8.4. We see that even with a simple ML model we can get RMSE that is close to the MD accuracy.

To gain a physical understanding of how the kirigami should be designed we plot the values of the parameters β. The first order parameters β_i are negative, suggesting that yield strains will be higher when the materials have more cuts, as shown in fig. 8.5(b). The second order parameters β_{ij} represent the pairwise 'interaction coupling', and these

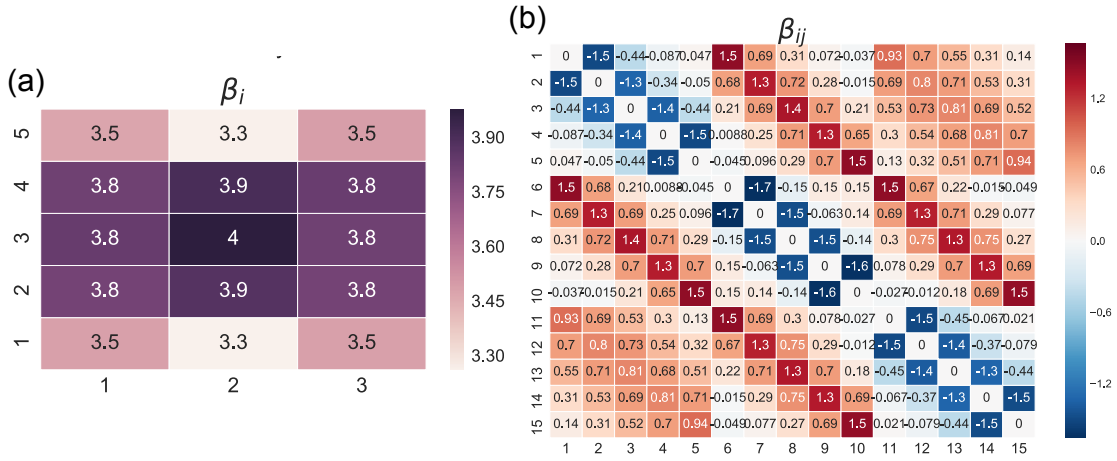

Figure 8.6: (a) Learned first order parameter β_i plotted in 2D arrays to match with the real space positions for yield stress. Here (1,1) is β_1, (1, 2) is β_2 and so on. (b) Learned matrix second order parameters (coupling interactions) β_{ij} for yield stress.

give better insights on how the kirigami should be designed in order to achieve high yield strains. From fig. 8.5(c), we see that the values β_{ij} are lowest (most negative) between two neighbors along the $\vec{x}$ direction. On the other hand the coupling is positive between two neighbors along $\vec{y}$. For instance $\beta_{12} = 0.01$ while $\beta_{16} = -0.02$. The regression results suggest that to achieve a high yield strain, cells (with a cut or no cut) of same type should be placed long the $\hat{y}$, while the opposite type should be placed right next to each other in the $\hat{x}$. This means the kirigami should have a line of cuts in $\hat{y}$ that alternate in the $\hat{x}$ direction. This resembles mechanical springs with two different constants that are connected in series. Overall, the first order parameters β_i tell us that increasing cut density will result in higher strains; the second order parameters β_{ij} gives further design principles on how the cuts should be arranged.

As shown in fig. 8.6(a), all first order parameters β_i for yield stress are positive, suggesting that introducing cuts will lower the yield stress. From fig. 8.6(b), we see that the values are lowest (most negative) between two neighbors along the $\vec{y}$ direction. On the other hand the coupling is positive between two neighbors along $\vec{x}$. For instance $\beta_{12} = -1.5$ while $\beta_{16} = +1.5$. The regression results suggest that kirigami should have arrays of cuts

(or no cuts) in $\hat{x}$ that alternate in the $\hat{y}$ direction. This resembles mechanical springs with two different constants that are connected in parallel. In contrast to *nearest neighbor* β_{ij} of the yield strain, the nearest neighbor for yield strain is positive $\beta_{ij} > 0$ along $\hat{x}$ while $\beta_{ij} < 0$ when the j element is not in the same $\hat{y}$.

8.7 Model complexity and larger systems

We want to note that using series expansion and OLS works reasonably well for this simplest system; however, for finer grids (or larger systems), the number of parameters will increase significantly as there will be $(n+d)!/(n!d!) \sim n^d/d$ of h terms, where d is the polynomial degree, n is number of grids (features). If we use one rectangular graphene unit cell as the size of one grid. Then, for a system size $\sim 100 \times 200$ $\mathring{A}$, there will be 30×80 grids (10×16 rectangular graphene cells in each coarse grid). At a polynomial degree of 3, we will need $\sim 10^9$ parameters to fit. This series expansion approach is computationally inefficient as we know from previous analysis that the close neighbors are the defining factors.

Gu et al. found that a very low training density $1^{-12}\%$ of total possible configurations is needed to train a linear ML model to find good materials candidates in composite materials with a pre crack based on FEM [187]. However, the work did not explain why such a low data density can train the ML. We argue that number of data needed to train *does not* grow exponentially with system size (possible configurations 2^n). Instead it scales with model complexity which is roughly proportional to number of parameters in the model. And because of locality, number complexity should scale $\mathcal{C} \times n$ instead of $(n+d)!/(n!d!) \sim n^d/d$, where $\mathcal{C}$ is some number. Of course one can do series expansion to nearest neighbors only, but in practice we often do not have prior knowledge regarding the locality of the interactions. We also want to note that the locality here does not necessarily mean a close distance in the *real* space. For example, there could a strong interaction between an element on one side of the membrane to the one on the opposite side, as exemplified by β_{ij} of yield strain.

In the series expansion approach, the 2D cut patterns are flattened into a 1D-array and thus some of the local spatial information are lost. Series expansion can be used to 'recover' the information of interactions between neighbors, but this approach becomes inefficient when the number of cells becomes large. This series expansion approach is computationally inefficient as we expect the interactions should be local. It has been known that neural networks (NN) can approximate any arbitrary functions [201, 202]. NN, however, still does not take advantage of *locality* as it builds connections for all elements. For these reasons, the convolutional neural network (CNN) is a more appropriate and scalable model as this deep learning is superior in recognizing edges in 2D motifs as well as performing down-sampling, which is very suitable for our problem. In the CNN, the 2D image (input) is convolved by a set of learnable filters and this allows the model to learn 2D motifs. An image passing through these filters then activates neurons which then classify (or rank) the cutting patterns to good or bad designs. This approach is more efficient than the series expansion approach as the CNN model is built based on learned 2D local motifs.

8.8 Convolutional Neural Networks

We train NNs and CNNs to predict the yield strain in the context of supervised learning. 2D images of size 30×80 are used as inputs for training the CNN. For the NN, the 2D images are flattened to 1D arrays of size 2400. The 2400 grids correspond to the number of rectangular graphene unit cells. In vision tasks CNN is usually used for classification. Here, we will use both NN and CNN for *regression*. Accordingly, we do not include the activation function at the end of the final layer, and we minimize the mean squared error loss to optimize the model parameters.

Since the yield strain and yield stress results are similar as they are roughly inversely proportional to each other (see fig. 6.2(b)), we will focus on the yield strain. Out of 2^{15} possible configurations, only the 29,791 non-detached configurations are considered. We find the non-detached configurations, where non-detached means that there is no cut that

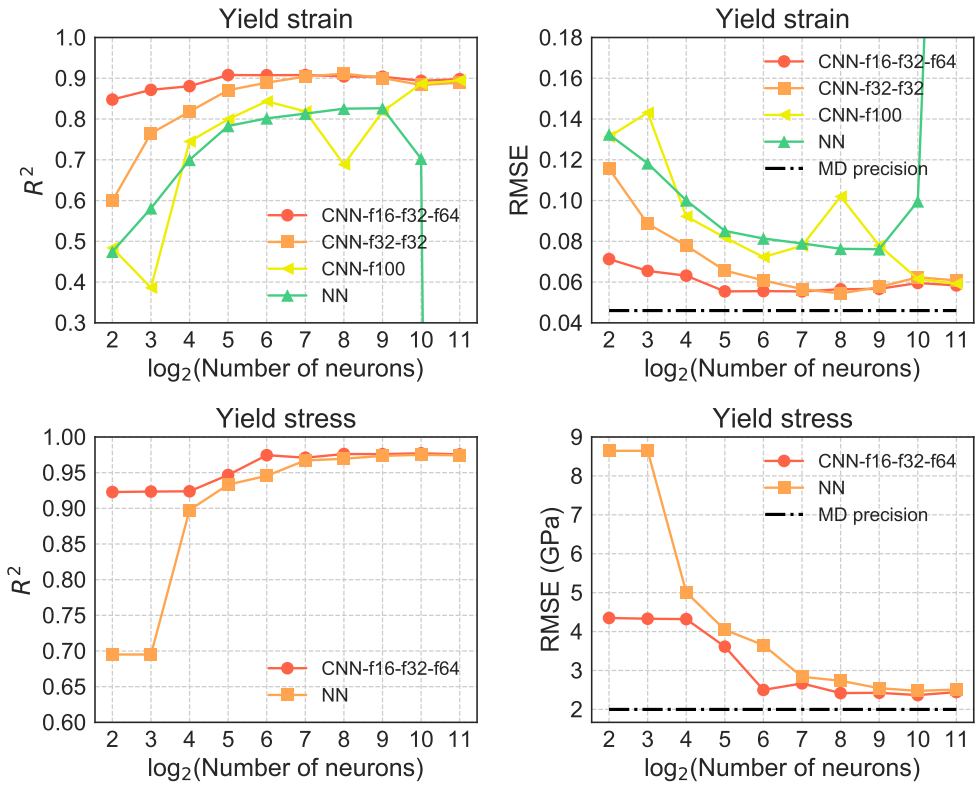

Figure 8.7: R^2 and RMSE for yield strain (a, b) and yield stress (c, d) as a function of number of neurons for NN or size of fully-connected layer for CNN for different number of grids. In general, an increasing number of neurons increases the model accuracy. It can be seen that the CNN models outperform the NN models.

traverses the entire length (in the y-direction) of the kirigami. We randomly shuffle the 29,791 data samples, and use 80% for training, 10% for validation, and 10% for the test set. We perform several shuffles and find that all performances are similar (with CNN-f16-f32-f64-h64 model). In addition, we perform 9-fold cross-validation and obtain an average accuracy on the test set of 0.918 with a standard deviation of 0.002. The validation dataset is used to find better architectures ("hyperparameter tuning", i.e. changing number of neurons or filters), and the test dataset is used to assess performance.

We use simple shallow NNs with one hidden layer of size ranging from 4 and 2024. For

CNN, we use architectures similar to VGGNet [203]. The kernel size is fixed at 3×3 with a stride of 1. Each convolutional layer is followed by a rectified linear unit (ReLU) function and a max-pooling layer of size 2×2 with stride of 2 [61]. The same padding was used after the first convolutional layer to preserve the image size. We included one fully-connected layer of size ranging from 4 to 2024. As we performed regression, we did not include the ReLU function at the end of the final layer. The Adam optimizer was used to minimized the mean squared error.

We use the root-mean-square error (RMSE) and R^2 on the test set to evaluate the goodness of a model. A CNN with number of filters of 16, 32, 64 in first, second, and third convolutional layer, respectively, and a fully-connected layer (FCL) of size 64 achieves $R^2 = 0.92$ and RMSE of 0.053 which is close to the MD precision of 0.046. We will denote this CNN model by CNN-f16-f32-f64-h64; here 'f' stands for filter and 'h' stands for number of neurons in the FCL. A NN with 64 neurons achieves $R^2 = 0.84$ and RMSE of 0.075. A NN with 246 neurons achieves a RMSE of 0.123 and CNN with 256 FCL achieves a RMSE of 0.054.

In each model, the R^2 of the training dataset is slightly larger than the validation or test dataset, indicating that there is no overfitting problem. For instance, for CNN-f16-f32-f64-h64 the R^2 are 0.94, 0.91, 0.92, on training, validation, and test dataset respectively. The RMSE are 0.045, 0.055, 0.053 on training, validation, and test dataset respectively. We found that the deep CNN architecture with increasing number of filters from 16 to 64, similar to VGGNet architecture [203], performed the best compared to the wide CNN architectures or wide NNs. The performance comparison on the validation dataset is shown in fig. 8.7. In addition, we also include performance comparison for yield stress shown in fig. 8.7(c) and (d). Fig. 8.8 shows the CNN-f16-f32-f64-h64 fitness in predicting yield strain and yield stress on the test datasets. Previously we found that for yield strain, OLS with a polynomial degree of 3 gives $R^2 = 0.76$ and RMSE = 0.084. Overall we found that the CNN performs better than NN and OLS as the CNN learns from the local 2D patterns.

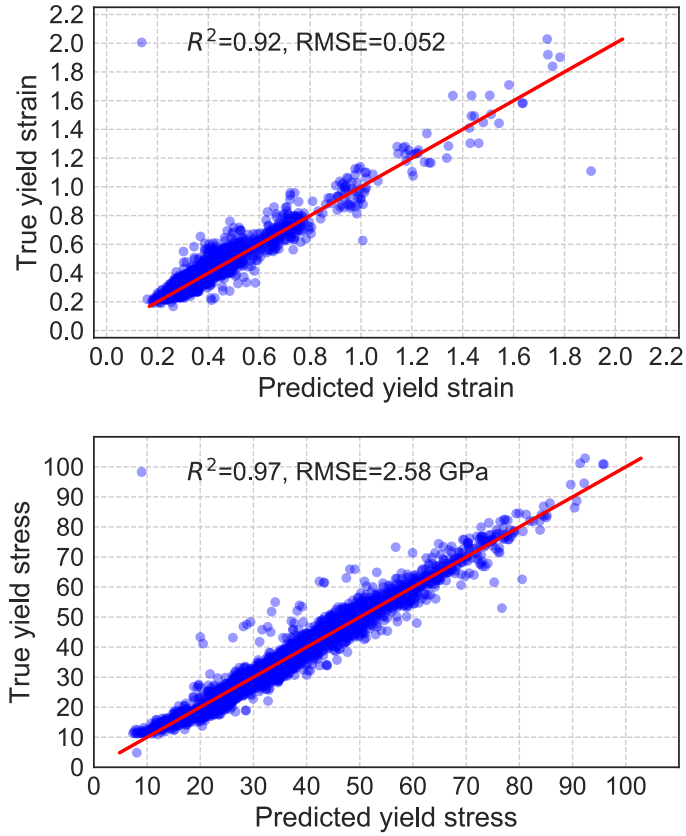

Figure 8.8: Plot of true values (test dataset) as a function of predicted value for (a) yield strain and (b) yield stress. Here, the CNN-f16-f32-f64-h64 model was used. The red line represents $y = x$ line.

8.9 Inverse Design of Highly Stretchable Kirigami

In the previous section, we used NN and CNN for the prediction of mechanical properties, in the context of supervised learning. Next, we investigate if the approximated function can be used to search for optimal designs. Here, we will use CNN, the best performing model, to search for the cut configuration with the largest yield strain. The procedure is as follows: first we randomly choose 100 configurations from the library of all possible configurations and use MD to obtain the yield strain. After training, the CNN then is used to screen the *unexplored* data set for the top performing 100 remaining candidates. Based

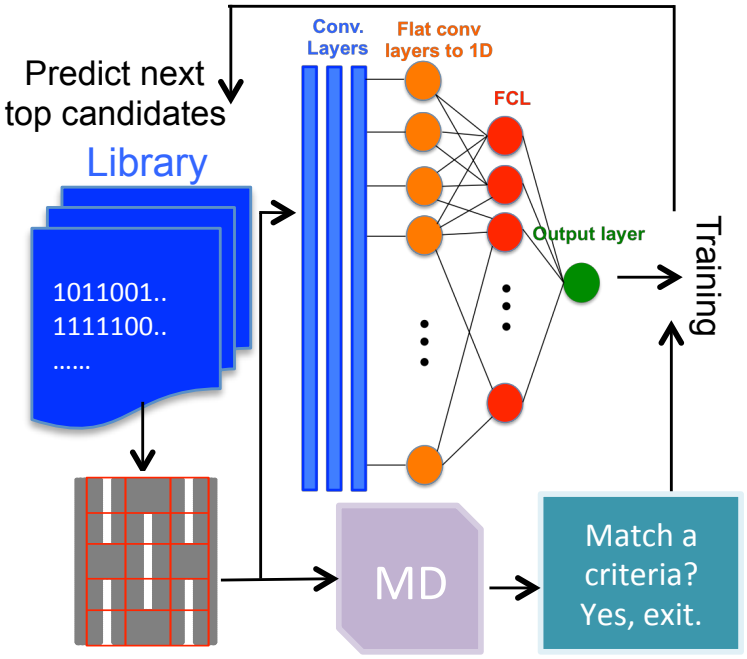

Figure 8.9: Schematic of the neural network search algorithm.

on this screening, 100 new MD simulations are performed and the results are added to the training set for the next generation. The ML search algorithm flow diagram is shown in fig. 6.5(a). The difference from the previous section is that here we train the model incrementally with the predicted top performers.

We first use the 3×5 allowed cuts where we already have simulated *all* of the possible configurations in MD to make sure that our model indeed finds the *true* (or close to) optimal designs. To evaluate the performance of the search algorithm we use the average of yield strain of the top 100 performers $\overline{\varepsilon^y}_{\text{top100}}$ for each generation. This number, which cannot be too small, is chosen arbitrarily so that we obtain more than a handful of good candidates. As a benchmark, we include the 'naive' random search. Specifically, we use CNN-f16-f32-f64-h64 architecture to find the optimal designs. As shown in fig. 8.10(a), the random search needs 30 generations (3000 MD simulations) to get $\overline{\varepsilon^y}_{\text{top100}} \geq 1.0$ (100%strain) and explore the entire design space in order to find the true best 100 performers. The CNN approach requires only *3 generations* (300 MD simulations data) to search for 100 candidates with

$\overline{\epsilon^y}_{\text{top100}} \sim 1.0$ and 10 generations to search the *true* top 100 performers. In each generation the standard deviation of $\overline{\epsilon^y}_{\text{top100}}$ is around 0.25. Using CNN to search for optimal designs is crucial because one MD simulation of graphene with a size of 100×200 Å requires around 1 hour computing time using 4 cores of CPU. In each generation, the required time to train the CNN and to predict the yield strain of one configuration is around 6 milliseconds on 4 CPU cores (same machines) or 3 milliseconds on 4 CPU cores plus one GPU. From fig. 6.2(b), we know that sheets with high strains are ones with high cut density. However, the variability is also large; for example at 11/15 cut density, the yield strain ranges from 0.2 to 1.7. Despite of this complexity, the ML quickly learns to find solutions at high cut density and also to find the right cutting patterns.

Next, we apply this simple algorithm to a much larger design space where the true optimal designs are *unknown* and also with a specified design constraint. Specifically, we study larger graphene sheets by extending the physical size in $\hat{x}$ from $\sim 100 \times 200$ to $\sim 200 \times 200$ Å (from 30×80 to 50×80 rectangular graphene unit cells). For this system, one MD simulation requires around 3 hours of computing time running on 4 cores. The allowed cuts are also expanded from 3×5 to 5×5 grids. For this problem, we fixed number of cuts at 11 cuts, which gives a design space of size $\frac{25!}{11!14!} \sim 4 \times 10^6$. For this system, we could not use brute force to simulate all configurations as we did previously for system with 15 allowed cuts. While the typical stretchable kirigamis usually have cuts and no-cuts along the loading direction ($\hat{x}$), it is not clear whether all the cuts should be located closely in a region or distributed equally.

As shown in fig. 8.10(b), the CNN is able to find designs with higher yield strains. With fewer than 10 generations (1000 training data), the CNN is able to find configurations with yield strains ≥ 1.0, which is roughly *five* times larger than a sheet without cuts. In each generation, the standard deviation of the top 100 performers is around 0.1. In fig. 8.11(a), we plot cut configurations of the top five performers in each generation. It can be seen that the cut configurations are random in the early stage of the search but evolve quickly to configurations with a long cut along the $\hat{y}$ direction alternating in $\hat{x}$ direction, as we

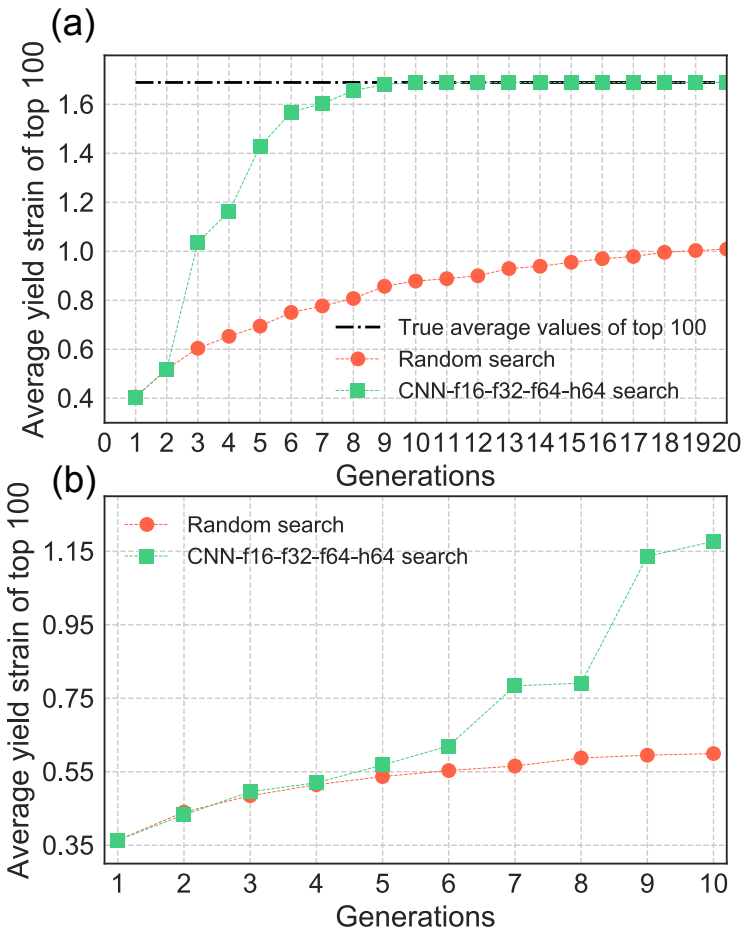

Figure 8.10: Average yield strains of the top 100 performers as a function of generations for kirigami with allowed cuts of (a) 3×5 and (b) 5×5.

expected from the smaller grid system. This suggests that our ML approach is scalable in a sense that the same CNN architecture used previously in the simpler system with 15 allowed cuts can search the optimal designs effectively despite a large design space.

We next take a closer look on the top performing configurations. Interestingly, the optimal solutions for maximum stretchability found by CNN have cuts at the edges which are different from the "typical" kirigami with centering cuts (fig. 8.11(b) configuration I). The found best performer has a yield strain *twice* as large as the kirigami with centering cuts. We found that to achieve high yield strains the long cuts should be located close to each other, rather than being sparsely or equally distributed across the sheet along

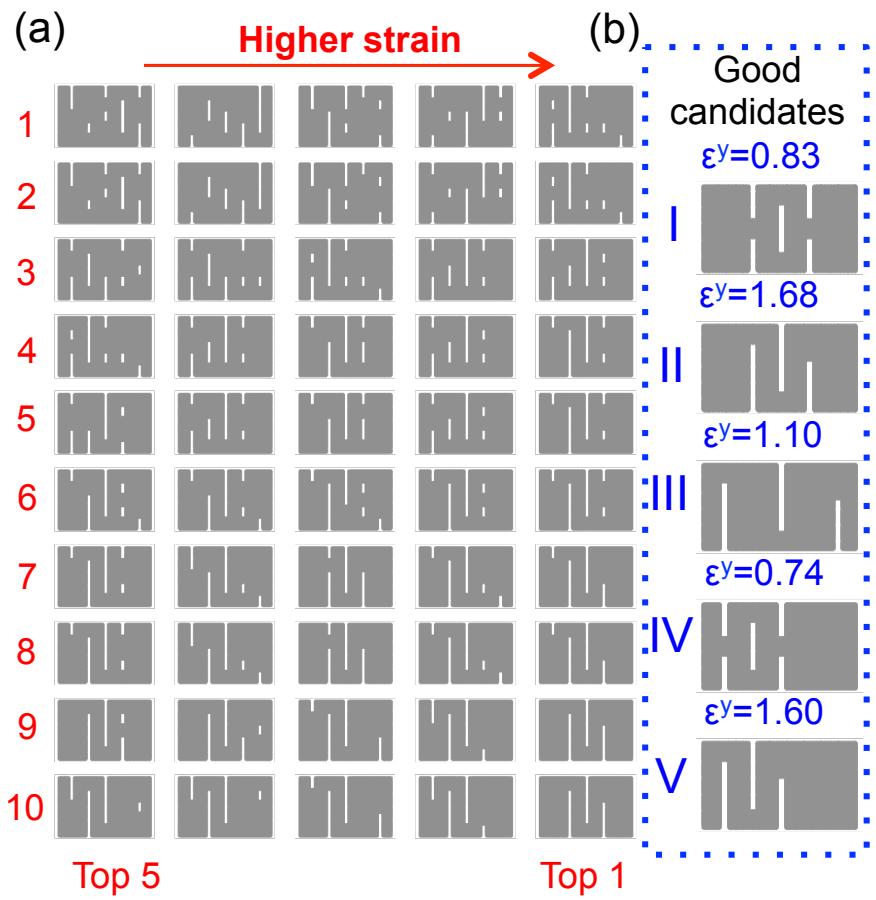

Figure 8.11: (a) Visualization of top five performers of kirigami with 5×5 allowed cuts in each generation. After the ninth generation, the top three performers remain constant. (b) A comparison between the top performing configurations found by the ML and the typical kirigami configurations with centering cuts. Note that the kirigami visualizations are not scaled to the real physical dimensions for clarity.

the $\hat{x}$ direction, as shown by comparing configurations II and III in fig. 8.11(b). These overlapping cut configurations allow larger rotations and out-of-plane deflection which give higher stretchability, i.e. the alternating edge cut pattern effectively transforms the 2D membrane to a quasi-1D membrane. Close packing of the alternating edge cuts allows increased stretchability because the thinner ribbons connecting different segments improve twisting. This result is similar to what we found previously in kirigami with centering cuts [155, 169].

8.10 Rotations in kirigami

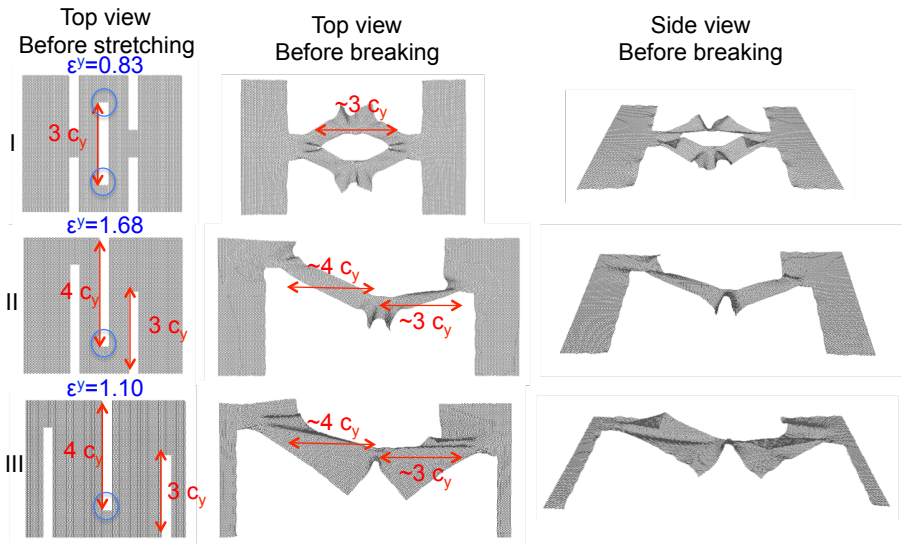

Figure 8.12: Top and side views of three representative kirigamis.

Here we investigate the mechanisms enabling high stretchability, and focus on rotation mechanisms in a few kirigami structures as shown in fig. 8.12. First we compare a kirigami with typical centering cuts (fig. 8.12 I) and a kirigami with alternating edge cuts (fig. 8.12 II).

Let the dimension of one cut be $c_x \times c_y$. We denote the "meeting point" in the middle segment where two ribbons are connected as a node, which are denoted by circles in fig. 8.12. Assuming there is no bond breaking, configuration I will have a maximum extension of $\approx 3c_x$ where the ribbons are connected by two nodes, whereas configuration II will have a maximum extension $\approx 7c_x$ as the ribbon is connected by one node. This additional degree of freedom (one fewer connecting node) enables configuration II to experience significantly more elastic stretching as compared to configuration I. As mentioned in the main text, the ML indeed found that the yield strain of configuration II is almost *twice* as large that of configuration I, as the alternating edge cut pattern effectively transforms the 2D membrane to quasi-1D membrane. We want to note that the kirigamis indeed buckle in the out-of-plane direction (see fig. 8.13), which is they key to prevent breaking.

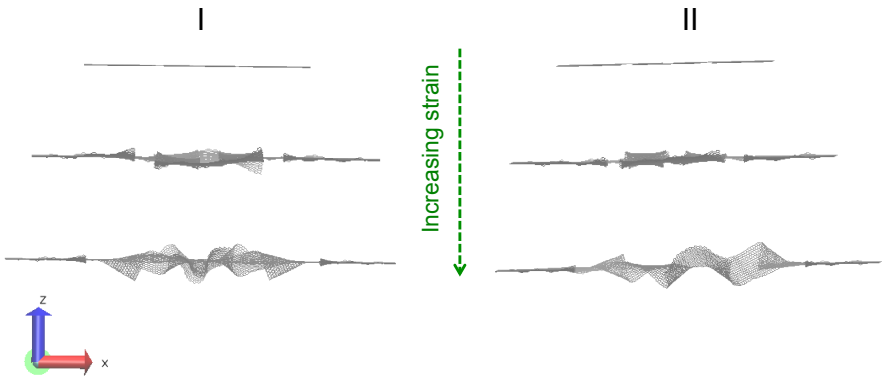

Figure 8.13: Side view of graphene kirigami structure I and II during stretching. It can be seen that the kirigamis buckled in the out-of-plane direction.

An additional consideration is how the closeness of the alternating edge cuts impacts the elastic stretchability. As can be seen by comparing configurations II and III in fig. 8.12, close packing of the alternating edge cuts allows increased stretchability. This is because, as seen from the side view, the ribbons need to rotate (twist) due to the applied tensile loading. Because the cuts are sparse in configuration III, the ribbons around the nodes are thick. In configuration II, the ribbons are thinner, which improves twisting and increases stretchability from 1.10 to 1.68.

This design principle is particularly useful as recently a combination of dense and sparse cut spacing were used to design stretchable thin electronic membranes [204]. It is remarkable not only that ML can quickly find the optimal designs using few training data ($< 1\%$ of the design space) under certain constraints, but also that ML can capture uncommon physical insights needed to produce the optimal designs, in this case related to the cut density and locations of the cuts.

8.11 Summary

We have shown how machine learning (ML) methods can be used to design graphene kirigami, where yield strain and stress are used as the target properties. We found that

CNN with three convolutional layers followed by one fully-connected layer is sufficient to find the optimal designs with relatively few training data. Our work shows not only how to use ML to effectively search for optimal designs but also to give new understanding on how kirigami cuts change the mechanical properties of graphene sheets. Furthermore, the ML method is parameter-free, in a sense that it can be used to design any material without any prior physical knowledge of the system. As the ML method only needs data, it can be applied to experimental work where the physical model is not known and cannot be simulated by MD or other simulation methods. Based on previous work indicating the scale-invariance of kirigami deformation [175], the kirigami structures found here using ML should also be applicable for designing larger macroscale kirigami structures.

Chapter 9

Concluding Remarks

In this thesis, we have used different computational techniques, developed tight-binding and continuum models, and introduced machine learning approaches to study and design 2D materials beyond graphene.

In the first half of this thesis, we focused on studies of 2D materials beyond graphene via density functional theory (DFT). We discovered novel effects such as valley and polarization switching in monochalcogenide monolayers and orbital-spin switching in lead chalcogenide monolayers. Tunable properties (e.g. spin and valley polarization) can be controlled by breaking the inversion symmetry via buckling or puckering. As the spin and valley states are dictated by the crystal symmetry, we proposed to utilize these new materials for developing non-volatile memories [32]. Very recently, accessing valley polarization with linearly polarized in SnS has been realized experimentally [62]. A further experimental realization of incorporating strain or electric control to change the symmetry for switching the valley polarization would be important for developing strain based valleytronic devices.

Recently, the Rashba effect has been observed in thin layers (6–20 nm) of lead sulfide (PbS) [128], where an external electric field is used to break the inversion symmetry. Our theoretical studies suggest that the buckled structure is the stable phase of PbS monolayer [35]. Applications of in-plane or out-of-plane strains should change the strength of Rashba coupling as well as to invert the direction of polarization. The switchable electric polarization and spin-texture is crucial to develop next-generation non-volatile spintronics.

We discussed some limitations of DFT for studying 2D materials with inhomogeneities

due to local strains or defects. Molecular dynamics (MD) are far more time efficient for calculating the structural changes; this method, however, does not calculate electronic properties as MD are *classical* simulations. We further developed a tight-binding (TB) approach to describe the electronic changes in heavy atoms in a square lattice. Even with a simple TB model, we were able to capture many novel properties, such as spin-polarization, which were consistent with the DFT results.

A further development of the TB model was carried out to incorporate strain effects. We found a direct relationship between spontaneous polarizations and the Rasha fields, which is not well understood for ferroelectric Rashba materials [205]. We find that the strains induce gauge fields in the low-order energy Hamiltonian near the symmetry points. The fields shifts the Rashba point and modify the Rashba parameter, which is equivalent to applications of in-plane magnetic fields by minimal coupling substitution. We found that applying 2% in-plane strains is equivalent to application of a 600 Tesla magnetic field. This opens the possibility to study chiral electrons in an extremely large *pseudo* magnetic field, which cannot be achieved in a laboratory setting. The out-of-plane strain, which is roughly proportional to the electric polarization, is also shown to modify the Rashba parameter. In particular the strain and electrical control of the Rashba effect is of practical interest because it allows the manipulation of spin states using electric fields (or strains) rather than magnetic fields. The buckling atoms can be used to write memory as each domain will have different spin-texture. Several experimental works use out-of-plane magnetic fields (parallel to the polar axis of Rashba materials) to measure the Rashba parameter as the Landau level spectrum changes with the strength of the Rashba parameter [99, 131]. One could also use this experimental approach to detect variations in the Rashba parameter in PbX due to out-of-plane strains. Overall our theory provides a new understanding on the connection between ferroelectricity and Rashba fields in ferroelectric Rashba materials and an alternative approach (i.e. the usage of TB with atomistic simulations) to study the variations of Rashba parameters due to inhomogeneous strains that will occur in practical applications. Our results are important to a broad range of research communities that

study spin, ferroelectricity, or band engineering in 2D systems.

In the second part of the thesis, we focused on changing mechanical properties of 2D materials using geometrical cuts, known as kirigami. We found that the tensile yield can be improved by a factor of four compared to pristine MoS_2 nanoribbons. In other studies [175], we showed that there is a universal relationship between the maximum buckling height and fracture strain in thin sheets from macro to nanoscales. These results in conjunction with recent results on other systems suggest that the kirigami approach may be a generally useful one for enhancing the ductility of two-dimensional materials.

Lastly, we introduced a machine learning (ML) approach for structural topology optimization in 2D materials. We showed that convolutional neural networks (CNN) are able to predict material properties close to the ground truth accuracy level, which is obtained from MD simulations [206]. Our work is the first demonstration of the applicability of ML to predict stretchability in graphene kirigami. We then showed how the CNN can be used for search algorithm. The algorithm is able to search for the optimal solutions with only 1000 training data in a large design space of 4,000,000. The solutions have non-symmetric cuts, which are different from the typical kirigami cuts. Importantly, the ML methods we used can learn from a small amount of data to generate superior designs that outperform their predecessors (similar to an evolutionary process). Designing micron-size kirigami (actuators) that are flexible and can actuate is important for developing micron-size biosensors and surgical robots [207, 208, 209].

The ML approaches should also be applicable for optimizing other properties (e.g. electronic and thermal properties). One of the great advantages of ML is that the it can learn from data only without knowing any physical principles.This means that ML can be applied to "raw" experimental data, such as images of atoms, spatial local density of states, and so on. We do believe however that, when available, any known physical intuitions and knowledge should be incorporated to the model. We also want to note that while deep neural networks (e.g. CNN) have shown to be a powerful tool, one of the limitations is that deep neural networks are often not easy to interpret compared to simpler ones (e.g. linear

models). Interpretability and transparency are central when deploying deep learning for any kind of systems. Moreover, to study physical systems, while attaining good prediction is important, understanding remains the ultimate goal.

Lastly, while applications of ML to materials are currently the most vibrant ongoing research, from predicting properties and rapid discoveries [210, 211, 212] to developing neural network potentials [188, 189, 213, 214], there are still very few efforts on comparing the time performance and accuracy of ML and to that of more traditional optimization techniques, such as genetic algorithms and topology optimization algorithms. This comparison is less straight forward because most of modern ML algorithms (in particular deep learning) exploit parallel and GPU computing while the conventional optimization techniques may not always have such tools in hand.

Despite these challenges, we are fortunate that both current computational and experimental techniques are complimenting each other, by providing theoretical frameworks and physical realizations of new 2D materials. This together will provide us a better understanding of yet to be explored many intriguing physical phenomena in 2D playground, as Feyman nicely put it "What I cannot create, I do not understand."

Appendix A

Input Files for Simulations

Here we provide some examples of input Quantum Espresso (QE) files. Most of the pseudopotentials can be found in https://www.quantum-espresso.org/pseudopotentials. We recomend to perform lattice relaxations before calculating the band structure. We want to note that the input files provided here are served as examples. All actual values used in simulations can be found in our papers.

A.0.1 QE Input Files for SnS

A.0.1.1 Self Consistent Calculation

```
&CONTROL
     calculation  = 'scf',
     restart_mode = 'from_scratch',
     wf_collect   = .true.
     verbosity = 'high'
     pseudo_dir='/project/frgeeeph/twodmaterial/pseudo'
/
&SYSTEM
     ibrav=8,
     celldm(1)=7.948807836,
     celldm(2)=0.9728322218,
     celldm(3)=5.923255237,
     nat=4,
     ntyp=2,
     ecutwfc=70.0,
     occupations='smearing',
     smearing='gaussian',
     degauss=0.020000,
     nbnd=30
     /
&ELECTRONS
  electron_maxstep = 100,
  conv_thr =  1.0e-8,
```

```
  mixing_beta = 0.5,
  /
&IONS
/
&cell
 cell_dynamics='bfgs'
 cell_factor=3
 press_conv_thr=0.1
/
ATOMIC_SPECIES
Sn    1.0   Sn.pbe-mt_fhi.UPF
S    1.0   S.pbe-mt_fhi.UPF
ATOMIC_POSITIONS crystal
Sn      -0.25   -0.25   0.055
S       0.19    0.25    0.065
Sn      0.25    0.25    0.168
S       -0.31   -0.25   0.158
K_POINTS automatic
10 10 1  0 0 0
```

To perform lattice relaxation change 'scf' to 'vc-relax'.

A.0.1.2 Band Structure Calculation

```
&CONTROL
     calculation  = 'bands',
     wf_collect   = .true.
     verbosity = 'high'
     pseudo_dir='/project/frgeeeph/twodmaterial/pseudo'
/
&SYSTEM
     ibrav=8,
     celldm(1)=7.948807836,
     celldm(2)=0.9728322218,
     celldm(3)=5.923255237,
     nat=4,
     ntyp=2,
     ecutwfc=70.0,
     occupations='smearing',
     smearing='gaussian',
     degauss=0.020000,
     nbnd=30
     /
&ELECTRONS
  electron_maxstep = 100,
  conv_thr =  1.0e-8,
  mixing_beta = 0.5,
  /
&IONS
/
&cell
 cell_dynamics='bfgs'
```

```
cell_factor=3
 /
ATOMIC_SPECIES
Sn    1.0   Sn.pbe-mt_fhi.UPF
S    1.0   S.pbe-mt_fhi.UPF
ATOMIC_POSITIONS crystal
Sn      -0.25   -0.25   0.055
S       0.19    0.25    0.065
Sn      0.25    0.25    0.168
S       -0.31   -0.25   0.158
K_POINTS crystal_b
5
0.5 0.0 0.0     20
0.0 0.0 0.0     20
0.0 0.5 0.0     20
0.5 0.5 0.0     20
0.5 0.0 0.0     20
```

We use k-points with a path along the symmetry points.

A.0.2 QE Input Files for GeSe

A.0.2.1 Self Consistent Calculation

```
&CONTROL
     calculation  = 'scf',
     restart_mode = 'from_scratch',
     wf_collect   = .true.
     verbosity = 'high'
     pseudo_dir='/project/frgeeeph/twodmaterial/pseudo'
     /
&SYSTEM
     ibrav=8,
     celldm(1)=8.032405556,
     celldm(2)=0.937622153,
     celldm(3)=5.839251938,
     nat=4,
     ntyp=2,
     ecutwfc=70.0,
     occupations='smearing',
     smearing='gaussian',
     degauss=0.020000,
     nbnd=30
     /
&ELECTRONS
  electron_maxstep = 100,
  conv_thr =  1.0e-8,
  mixing_beta = 0.5,
  /
&IONS
/
```

```
&cell
 cell_dynamics='bfgs'
 cell_factor=3
 press_conv_thr=0.1
 /
ATOMIC_SPECIES
Ge    1.0   Ge.pbe-mt_fhi.UPF
Se    1.0   Se.pbe-mt_fhi.UPF
ATOMIC_POSITIONS crystal
Ge      -0.25   0.25    0.06
Se      0.17    -0.25   0.055
Ge      0.25    -0.25   0.155
Se      -0.33   0.25    0.16
K_POINTS automatic
10 10 1  0 0 0
```

A.0.2.2 Band Structure Calculation

```
&CONTROL
     calculation  = 'bands',
     wf_collect   = .true.
     verbosity = 'high'
     pseudo_dir='/project/frgeeeph/twodmaterial/pseudo'
     /
&SYSTEM
     ibrav=8,
     celldm(1)=8.032405556,
     celldm(2)=0.937622153,
     celldm(3)=5.839251938,
     nat=4,
     ntyp=2,
     ecutwfc=70.0,
     occupations='smearing',
     smearing='gaussian',
     degauss=0.020000,
     nbnd=30
     /
&ELECTRONS
  electron_maxstep = 100,
  conv_thr =  1.0e-8,
  mixing_beta = 0.5,
  /
&IONS
/
&cell
 cell_dynamics='bfgs'
cell_factor=3
 /
ATOMIC_SPECIES
Ge    1.0   Ge.pbe-mt_fhi.UPF
Se    1.0   Se.pbe-mt_fhi.UPF
ATOMIC_POSITIONS crystal
```

```
Ge      -0.25   0.25    0.06
Se      0.17    -0.25   0.055
Ge      0.25    -0.25   0.155
Se      -0.33   0.25    0.16
K_POINTS crystal_b
5
0.5 0.0 0.0     20
0.0 0.0 0.0     20
0.0 0.5 0.0     20
0.5 0.5 0.0     20
0.5 0.0 0.0     20
```

A.0.3 QE Input Files for PbS

A.0.3.1 Self Consistent Calculation with Spin Orbit Interaction

```
&CONTROL
     calculation  = 'scf',
     restart_mode = 'from_scratch',
     wf_collect   = .true.
     tprnfor = .true.,
     pseudo_dir='/project/frgeeeph/twodmaterial/pseudo/rel-pbe.0.3.1/PSEUDOPOTENTIALS'
/
&SYSTEM
     ibrav=8,
     celldm(1)=7.060076352,
     celldm(2)=1,
     celldm(3)=5.546759341,
     nat=2,
     ntyp=2,
     ecutwfc=100.0,
     ecutrho=200,
     nosym=.false.,
     nbnd = 80,
     occupations = 'smearing' ,
     degauss = 0.01 ,
     smearing = 'gaussian' ,
     starting_magnetization(1) = 0.5,
     starting_magnetization(2) = 0.2,
     noncolin = .true. ,
     angle1(1) = 30,
     angle1(2) = 45,
     angle2(1) = 30,
     angle2(2) = 45,
     lspinorb = .true. ,
     london = .false. ,
     /
&ELECTRONS
  electron_maxstep = 100,
  conv_thr =  1.0e-8,
  mixing_beta = 0.5,
/
```

```
&IONS
/
&cell
 cell_dynamics='bfgs'
cell_factor=3
 /
ATOMIC_SPECIES
Pb      1.0     Pb.rel-pbe-dn-kjpaw_psl.0.2.2.UPF
S       1.0      S.rel-pbe-n-kjpaw_psl.0.1.UPF
ATOMIC_POSITIONS crystal
Pb       0.5   0.5   0.193
S        0.0   0.0   0.143
K_POINTS automatic
16 16 1  0 0 0
```

A.0.3.2 Band Structure Calculation with Spin Orbit Interaction

Similarly to other band structure calculations, simply replace 'scf' to 'bands' and change the k-points to

```
5
0.5 0.0 0.0     50
0.0 0.0 0.0     50
0.0 0.5 0.0     50
0.5 0.5 0.0     50
0.5 0.0 0.0     50
```

A.0.4 LAMMPS Input File and Machine Learning Model for Graphene Kirigami

Codes to generate atomic configurations and machine learning models (scikit-learn and TensorFlow) can be found in https://github.com/phanakata/ML_for_kirigami_design.

Bibliography

[1] Jin-Wu Jiang. Parametrization of stillinger–weber potential based on valence force field model: application to single-layer mos 2 and black phosphorus. *Nanotechnology*, 26(31):315706, 2015.

[2] Ryan C Cooper, Changgu Lee, Chris A Marianetti, Xiaoding Wei, James Hone, and Jeffrey W Kysar. Nonlinear elastic behavior of two-dimensional molybdenum disulfide. *Physical Review B*, 87(3):035423, 2013.

[3] Jin-Wu Jiang, Harold S Park, and Timon Rabczuk. Molecular dynamics simulations of single-layer molybdenum disulphide (mos2): Stillinger-weber parametrization, mechanical properties, and thermal conductivity. *Journal of Applied Physics*, 114(6):064307, 2013.

[4] J Zhao, L Kou, J-W Jiang, and T Rabczuk. Tension-induced phase transition of single-layer molybdenum disulfide (mos_2) at low temperatures. *Nanotechnology*, 25:295701, 2014.

[5] Richard P Feynman. There's plenty of room at the bottom. *Engineering and Science*, 23(5):22–36, 1960.

[6] Kostya S Novoselov, Andre K Geim, Sergei V Morozov, D Jiang, Y_ Zhang, Sergey V Dubonos, Irina V Grigorieva, and Alexandr A Firsov. Electric field effect in atomically thin carbon films. *Science*, 306(5696):666–669, 2004.

[7] Yuanbo Zhang, Yan-Wen Tan, Horst L Stormer, and Philip Kim. Experimental observation of the quantum hall effect and berry's phase in graphene. *Nature*, 438(7065):201, 2005.

[8] Kostya S Novoselov, Andre K Geim, SVb Morozov, Da Jiang, MIc Katsnelson, IVa Grigorieva, SVb Dubonos, and AA Firsov. Two-dimensional gas of massless dirac fermions in graphene. *Nature*, 438(7065):197, 2005.

[9] Andrea F Young and Philip Kim. Quantum interference and klein tunnelling in graphene heterojunctions. *Nature Physics*, 5(3):222, 2009.

[10] N Levy, SA Burke, KL Meaker, M Panlasigui, A Zettl, F Guinea, AH Castro Neto, and MF Crommie. Strain-induced pseudo–magnetic fields greater than 300 tesla in graphene nanobubbles. *Science*, 329(5991):544–547, 2010.

[11] KS Novoselov, D Jiang, F Schedin, TJ Booth, VV Khotkevich, SV Morozov, and AK Geim. Two-dimensional atomic crystals. *Proceedings of the National Academy of Sciences*, 102(30):10451–10453, 2005.

[12] Hualing Zeng, Junfeng Dai, Wang Yao, Di Xiao, and Xiaodong Cui. Valley polarization in mos2 monolayers by optical pumping. *Nature Nanotechnology*, 7(8):490–493, 2012.

[13] Kin Fai Mak, Keliang He, Jie Shan, and Tony F Heinz. Control of valley polarization in monolayer mos 2 by optical helicity. *Nature Nanotechnology*, 7(8):494, 2012.

[14] Slaven Garaj, W Hubbard, A Reina, J Kong, D Branton, and JA Golovchenko. Graphene as a subnanometre trans-electrode membrane. *Nature*, 467(7312):190, 2010.

[15] A Rycerz, J Tworzydło, and CWJ Beenakker. Valley filter and valley valve in graphene. *Nature Physics*, 3(3):172, 2007.

[16] Zhengyang Cai, Bilu Liu, Xiaolong Zou, and Hui-Ming Cheng. Chemical vapor deposition growth and applications of two-dimensional materials and their heterostructures. *Chemical Reviews*, 118(13):6091–6133, 2018. PMID: 29384374.

[17] Pere Miro, Martha Audiffred, and Thomas Heine. An atlas of two-dimensional materials. *Chem. Soc. Rev.*, 43:6537–6554, 2014.

[18] Valeria Nicolosi, Manish Chhowalla, Mercouri G. Kanatzidis, Michael S. Strano, and Jonathan N. Coleman. Liquid exfoliation of layered materials. *Science*, 340(6139), 2013.

[19] KS Novoselov, A Mishchenko, A Carvalho, and AH Castro Neto. 2d materials and van der waals heterostructures. *Science*, 353(6298):aac9439, 2016.

[20] R Suzuki, M Sakano, YJ Zhang, R Akashi, D Morikawa, A Harasawa, K Yaji, K Kuroda, K Miyamoto, T Okuda, et al. Valley-dependent spin polarization in bulk mos 2 with broken inversion symmetry. *Nature Nanotechnology*, 9(8):611, 2014.

[21] Jiaxu Yan, Juan Xia, Xingli Wang, Lei Liu, Jer-Lai Kuo, Beng Kang Tay, Shoushun Chen, Wu Zhou, Zheng Liu, and Ze Xiang Shen. Stacking-dependent interlayer coupling in trilayer mos2 with broken inversion symmetry. *Nano Letters*, 15(12):8155–8161, 2015.

[22] Yuan Cao, Valla Fatemi, Shiang Fang, Kenji Watanabe, Takashi Taniguchi, Efthimios Kaxiras, and Pablo Jarillo-Herrero. Unconventional superconductivity in magic-angle graphene superlattices. *Nature*, 556(7699):43, 2018.

[23] Young-Woo Son, Marvin L Cohen, and Steven G Louie. Half-metallic graphene nanoribbons. *Nature*, 444(7117):347, 2006.

[24] Levente Tapasztó, Gergely Dobrik, Philippe Lambin, and László P Biró. Tailoring the atomic structure of graphene nanoribbons by scanning tunnelling microscope lithography. *Nature Nanotechnology*, 3(7):397, 2008.

[25] Thomas G Pedersen, Christian Flindt, Jesper Pedersen, Niels Asger Mortensen, Antti-Pekka Jauho, and Kjeld Pedersen. Graphene antidot lattices: designed defects and spin qubits. *Physical Review Letters*, 100(13):136804, 2008.

[26] Victor W Brar, Régis Decker, Hans-Michael Solowan, Yang Wang, Lorenzo Maserati, Kevin T Chan, Hoonkyung Lee, Çağlar O Girit, Alex Zettl, Steven G Louie, et al. Gate-controlled ionization and screening of cobalt adatoms on a graphene surface. *Nature Physics*, 7(1):43, 2011.

[27] Young-Woo Son, Marvin L Cohen, and Steven G Louie. Energy gaps in graphene nanoribbons. *Physical Review Letters*, 97(21):216803, 2006.

[28] Melina K Blees, Arthur W Barnard, Peter A Rose, Samantha P Roberts, Kathryn L McGill, Pinshane Y Huang, Alexander R Ruyack, Joshua W Kevek, Bryce Kobrin, David A Muller, et al. Graphene kirigami. *Nature*, 524(7564):204, 2015.

[29] Han Liu, Adam T. Neal, Zhen Zhu, Zhe Luo, Xianfan Xu, David Tománek, and Peide D. Ye. Phosphorene: An unexplored 2d semiconductor with a high hole mobility. *ACS Nano*, 8(4):4033–4041, 2014.

[30] Xiaomu Wang, Aaron M Jones, Kyle L Seyler, Vy Tran, Yichen Jia, Huan Zhao, Han Wang, Li Yang, Xiaodong Xu, and Fengnian Xia. Highly anisotropic and robust excitons in monolayer black phosphorus. *Nature Nanotechnology*, 2015.

[31] Jin-Wu Jiang and Harold S. Park. Negative poisson's ratio in single-layer black phosphorus. *Nature Communications*, 5, 08 2014.

[32] Paul Z Hanakata, Alexandra Carvalho, David K Campbell, and Harold S Park. Polarization and valley switching in monolayer group-iv monochalcogenides. *Physical Review B*, 94(3):035304, 2016.

[33] Jay D. Sau, Roman M. Lutchyn, Sumanta Tewari, and S. Das Sarma. Generic new platform for topological quantum computation using semiconductor heterostructures. *Physical Review Letters*, 104:040502, Jan 2010.

[34] Liang Fu and C. L. Kane. Superconducting proximity effect and majorana fermions at the surface of a topological insulator. *Physical Review Letters*, 100:096407, Mar 2008.

[35] Paul Z. Hanakata, A. S. Rodin, Alexandra Carvalho, Harold S. Park, David K. Campbell, and A. H. Castro Neto. Two-dimensional square buckled rashba lead chalcogenides. *Physical Review B*, 96:161401, Oct 2017.

[36] A. S. Rodin, P. Z. Hanakata, A. Carvalho, H. S. Park, D. K. Campbell, and A. H. Castro Neto. Rashba-like dispersion in buckled square lattices. *Physical Review B*, 96:115450, Sep 2017.

[37] Alessandro Molle, Joshua Goldberger, Michel Houssa, Yong Xu, Shou-Cheng Zhang, and Deji Akinwande. Buckled two-dimensional xene sheets. *Nature Materials*, 16(2):163, 2017.

[38] Bevin Huang, Genevieve Clark, Dahlia R Klein, David MacNeill, Efren Navarro-Moratalla, Kyle L Seyler, Nathan Wilson, Michael A McGuire, David H Cobden, Di Xiao, et al. Electrical control of 2d magnetism in bilayer cri 3. *Nature Nanotechnology*, 13(7):544, 2018.

[39] Efthimios Kaxiras et al. *Atomic and electronic structure of solids*. Cambridge University Press, 2003.

[40] Richard M Martin. *Electronic structure: basic theory and practical methods*. Cambridge University Press, 2004.

[41] Frank Jensen. *Introduction to computational chemistry*. John wiley & sons, 2017.

[42] Daan Frenkel and Berend Smit. *Understanding molecular simulation: from algorithms to applications*, volume 1. Elsevier, 2001.

[43] Abdulnour Y Toukmaji and John A Board Jr. Ewald summation techniques in perspective: a survey. *Computer Physics Communications*, 95(2-3):73–92, 1996.

[44] Tim Mueller, Aaron Gilad Kusne, and Rampi Ramprasad. Machine learning in materials science: Recent progress and emerging applications. *Reviews in Computational Chemistry*, 29:186–273, 2016.

[45] Keith T Butler, Daniel W Davies, Hugh Cartwright, Olexandr Isayev, and Aron Walsh. Machine learning for molecular and materials science. *Nature*, 559(7715):547, 2018.

[46] Juan Carrasquilla and Roger G Melko. Machine learning phases of matter. *Nature Physics*, 13(5):431, 2017.

[47] Anubhav Jain, Shyue Ping Ong, Geoffroy Hautier, Wei Chen, William Davidson Richards, Stephen Dacek, Shreyas Cholia, Dan Gunter, David Skinner, Gerbrand Ceder, and Kristin a. Persson. The Materials Project: A materials genome approach to accelerating materials innovation. *APL Materials*, 1(1):011002, 2013.

[48] Joanne Hill, Arun Mannodi-Kanakkithodi, Ramamurthy Ramprasad, and Bryce Meredig. Materials data infrastructure and materials informatics. In *Computational Materials System Design*, pages 193–225. Springer, 2018.

[49] Gowoon Cheon, Ekin D Cubuk, Evan R Antoniuk, Lavi Blumberg, Joshua E Goldberger, and Evan J Reed. Revealing the spectrum of unknown layered materials with superhuman predictive abilities. *The Journal of Physical Chemistry Letters*, 9(24):6967–6972, 2018.

[50] Sten Haastrup, Mikkel Strange, Mohnish Pandey, Thorsten Deilmann, Per S Schmidt, Nicki F Hinsche, Morten N Gjerding, Daniele Torelli, Peter M Larsen, Anders C Riis-Jensen, et al. The computational 2d materials database: high-throughput modeling and discovery of atomically thin crystals. *2D Materials*, 5(4):042002, 2018.

[51] Trevor David Rhone, Wei Chen, Shaan Desai, Amir Yacoby, and Efthimios Kaxiras. Data-driven studies of magnetic two-dimensional materials. *arXiv preprint arXiv:1806.07989*, 2018.

[52] Llewellyn H Thomas. The calculation of atomic fields. In *Mathematical Proceedings of the Cambridge Philosophical Society*, volume 23, pages 542–548. Cambridge University Press, 1927.

[53] Enrico Fermi. Un metodo statistico per la determinazione di alcune prioprietà dell'atomo. In *Accademia Nazionale dei Lincei*, volume 6, pages 602–607, 1927.

[54] Paul AM Dirac. Note on exchange phenomena in the thomas atom. In *Mathematical Proceedings of the Cambridge Philosophical Society*, volume 26, pages 376–385. Cambridge University Press, 1930.

[55] Pierre Hohenberg and Walter Kohn. Inhomogeneous electron gas. *Physical Review*, 136(3B):B864, 1964.

[56] Walter Kohn and Lu Jeu Sham. Self-consistent equations including exchange and correlation effects. *Physical Review*, 140(4A):A1133, 1965.

[57] Michael P Allen and Dominic J Tildesley. *Computer simulation of liquids*. Oxford university press, 2017.

[58] Ian Goodfellow, Yoshua Bengio, and Aaron Courville. *Deep Learning*. MIT Press, 2016. http://www.deeplearningbook.org.

[59] Trevor Hastie, Robert Tibshirani, and Jerome H. Friedman. *The elements of statistical learning: data mining, inference, and prediction, 2nd Edition*. Springer series in statistics. Springer, 2009.

[60] Pankaj Mehta, Marin Bukov, Ching-Hao Wang, Alexandre GR Day, Clint Richardson, Charles K Fisher, and David J Schwab. A high-bias, low-variance introduction to machine learning for physicists. *Physics Reports*, 2019.

[61] Yann LeCun, Léon Bottou, Yoshua Bengio, and Patrick Haffner. Gradient-based learning applied to document recognition. *Proceedings of the IEEE*, 86(11):2278–2324, 1998.

[62] Shuren Lin, Alexandra Carvalho, Shancheng Yan, Roger Li, Sujung Kim, Aleksandr Rodin, Lídia Carvalho, Emory M Chan, Xi Wang, Antonio H Castro Neto, et al. Accessing valley degree of freedom in bulk tin (ii) sulfide at room temperature. *Nature Communications*, 9(1):1455, 2018.

[63] Q H Wang, K Kalantar-Zadeh, A Kis, J N Coleman, and M S Strano. Electronics and optoelectronics of two-dimensional transition metal dichalcogenides. *Nature Nanotechnology*, 7:699–712, 2012.

[64] P Johari and V B Shenoy. Tuning the electronic properties of semiconducting transition metal dichalcogenides by applying mechanical strains. *ACS Nano*, 6(6):5449–5456, 2012.

[65] M Chhowalla, H S Shin, G Eda, L-J Li, K P Loh, and H Zhang. The chemistry of two-dimensional layered transition metal dichalcogenide nanosheets. *Nature Chemistry*, 5:263–275, 2013.

[66] Di Xiao, Gui-Bin Liu, Wanxiang Feng, Xiaodong Xu, and Wang Yao. Coupled spin and valley physics in monolayers of mos_2 and other group-vi dichalcogenides. *Physical Review Letters*, 108:196802, May 2012.

[67] Edbert J Sie, James W McIver, Yi-Hsien Lee, Liang Fu, Jing Kong, and Nuh Gedik. Valley-selective optical stark effect in monolayer ws2. *Nature Materials*, 14(3):290–294, 2014.

[68] Jonghwan Kim, Xiaoping Hong, Chenhao Jin, Su-Fei Shi, Chih-Yuan S. Chang, Ming-Hui Chiu, Lain-Jong Li, and Feng Wang. Ultrafast generation of pseudo-magnetic field for valley excitons in wse2 monolayers. *Science*, 346(6214):1205–1208, 2014.

[69] M. Sepioni, R. R. Nair, S. Rablen, J. Narayanan, F. Tuna, R. Winpenny, A. K. Geim, and I. V. Grigorieva. Limits on intrinsic magnetism in graphene. *Physical Review Letters*, 105:207205, Nov 2010.

[70] Emil B Song, Bob Lian, Sung Min Kim, Sejoon Lee, Tien-Kan Chung, Minsheng Wang, Caifu Zeng, Guangyu Xu, Kin Wong, Yi Zhou, et al. Robust bi-stable memory operation in single-layer graphene ferroelectric memory. *Applied Physics Letters*, 99(4):042109, 2011.

[71] Yi Zheng, Guang-Xin Ni, Chee-Tat Toh, Chin-Yaw Tan, Kui Yao, and Barbaros Özyilmaz. Graphene field-effect transistors with ferroelectric gating. *Physical Review Letters*, 105:166602, Oct 2010.

[72] RE Simpson, P Fons, AV Kolobov, T Fukaya, M Krbal, T Yagi, and J Tominaga. Interfacial phase-change memory. *Nature Nanotechnology*, 6(8):501–505, 2011.

[73] Sebahaddin Alptekin. Structural phase transition of snse under uniaxial stress and hydrostatic pressure: an ab initio study. *Journal of Molecular Modeling*, 17(11):2989–2994, 2011.

[74] T Chattopadhyay, A Werner, HG Von Schnering, and J Pannetier. Temperature and pressure induced phase transition in iv-vi compounds. *Revue de Physique Appliquée*, 19(9):807–813, 1984.

[75] Volker L. Deringer, Ralf P. Stoffel, and Richard Dronskowski. Vibrational and thermodynamic properties of gese in the quasiharmonic approximation. *Physical Review B*, 89:094303, Mar 2014.

[76] A. S. Rodin, A. Carvalho, and A. H. Castro Neto. Strain-induced gap modification in black phosphorus. *Physical Review Letters*, 112:176801, May 2014.

[77] Jack R. Brent, David J. Lewis, Tommy Lorenz, Edward A. Lewis, Nicky Savjani, Sarah J. Haigh, Gotthard Seifert, Brian Derby, and Paul O'Brien. Tin(ii) sulfide (sns) nanosheets by liquid-phase exfoliation of herzenbergite: Iv–vi main group two-dimensional atomic crystals. *Journal of the American Chemical Society*, 137(39):12689–12696, 2015.

[78] Bablu Mukherjee, Yongqing Cai, Hui Ru Tan, Yuan Ping Feng, Eng Soon Tok, and Chorng Haur Sow. Nir schottky photodetectors based on individual single-crystalline gese nanosheet. *ACS Applied Materials & Interfaces*, 5(19):9594–9604, 2013.

[79] Lídia C. Gomes and A. Carvalho. Phosphorene analogues: Isoelectronic two-dimensional group-iv monochalcogenides with orthorhombic structure. *Physical Review B*, 92:085406, Aug 2015.

[80] Ruixiang Fei, Wenbin Li, Ju Li, and Li Yang. Giant piezoelectricity of monolayer group iv monochalcogenides: Snse, sns, gese, and ges. *Applied Physics Letters*, 107(17):–, 2015.

[81] Lídia C. Gomes, A. Carvalho, and A. H. Castro Neto. Enhanced piezoelectricity and modified dielectric screening of two-dimensional group-iv monochalcogenides. *Physical Review B*, 92:214103, Dec 2015.

[82] Paolo Giannozzi, Stefano Baroni, Nicola Bonini, Matteo Calandra, Roberto Car, Carlo Cavazzoni, Davide Ceresoli, Guido L Chiarotti, Matteo Cococcioni, Ismaila Dabo, Andrea Dal Corso, Stefano de Gironcoli, Stefano Fabris, Guido Fratesi, Ralph Gebauer, Uwe Gerstmann, Christos Gougoussis, Anton Kokalj, Michele Lazzeri, Layla Martin-Samos, Nicola Marzari, Francesco Mauri, Riccardo Mazzarello, Stefano Paolini, Alfredo Pasquarello, Lorenzo Paulatto, Carlo Sbraccia, Sandro Scandolo, Gabriele Sclauzero, Ari P Seitsonen, Alexander Smogunov, Paolo Umari, and Renata M Wentzcovitch. Quantum espresso: a modular and open-source software project for quantum simulations of materials. *Journal of Physics: Condensed Matter*, 21(39):395502 (19pp), 2009.

[83] N. Troullier and José Luís Martins. Efficient pseudopotentials for plane-wave calculations. *Physical Review B*, 43:1993–2006, Jan 1991.

[84] Hendrik J. Monkhorst and James D. Pack. Special points for brillouin-zone integrations. *Physical Review B*, 13:5188–5192, Jun 1976.

[85] R. D. King-Smith and David Vanderbilt. Theory of polarization of crystalline solids. *Physical Review B*, 47:1651–1654, Jan 1993.

[86] Ivo Souza, Jorge Íñiguez, and David Vanderbilt. First-principles approach to insulators in finite electric fields. *Physical Review Letters*, 89:117602, Aug 2002.

[87] P. Umari and Alfredo Pasquarello. *Ab initio* molecular dynamics in a finite homogeneous electric field. *Physical Review Letters*, 89:157602, Sep 2002.

[88] Mehrshad Mehboudi, Alex M. Dorio, Wenjuan Zhu, Arend van der Zande, Hugh O. H. Churchill, Alejandro A. Pacheco-Sanjuan, Edmund O. Harriss, Pradeep Kumar, and Salvador Barraza-Lopez. Two-dimensional disorder in black phosphorus and monochalcogenide monolayers. *Nano Letters*, 16(3):1704–1712, 2016.

[89] S. Sanna, C. Thierfelder, S. Wippermann, T. P. Sinha, and W. G. Schmidt. Barium titanate ground- and excited-state properties from first-principles calculations. *Physical Review B*, 83:054112, Feb 2011.

[90] Mehrshad Mehboudi, Kainen Utt, Humberto Terrones, Edmund O. Harriss, Alejandro A. Pacheco SanJuan, and Salvador Barraza-Lopez. Strain and the optoelectronic properties of nonplanar phosphorene monolayers. *Proceedings of the National Academy of Sciences*, 112(19):5888–5892, 2015.

[91] W Zhong, RD King-Smith, and David Vanderbilt. Giant lo-to splittings in perovskite ferroelectrics. *Physical Review Letters*, 72(22):3618, 1994.

[92] Hua Wang and Xiaofeng Qian. Parametrization of stillinger-weber potential based on valence force field model: Application to single-layer mos2 and black phosphorus. *arXiv preprint arXiv:1606.04522*, 2015.

[93] Branimir Radisavljevic, Aleksandra Radenovic, Jacopo Brivio, V Giacometti, and A Kis. Single-layer mos2 transistors. *Nature Nanotechnology*, 6(3):147–150, 2011.

[94] A. S. Rodin, Lidia C. Gomes, A. Carvalho, and A. H. Castro Neto. Valley physics in tin (ii) sulfide. *Physical Review B*, 93:045431, Jan 2016.

[95] D. Gunlycke and C. T. White. Graphene valley filter using a line defect. *Physical Review Letters*, 106:136806, Mar 2011.

[96] John C Slater and George F Koster. Simplified lcao method for the periodic potential problem. *Physical Review*, 94(6):1498, 1954.

[97] Aurelien Manchon, Hyun Cheol Koo, Junsaku Nitta, SM Frolov, and RA Duine. New perspectives for rashba spin-orbit coupling. *Nature Materials*, 14(9):871–882, 2015.

[98] N Levy, SA Burke, KL Meaker, M Panlasigui, A Zettl, F Guinea, AH Castro Neto, and MF Crommie. Strain-induced pseudo–magnetic fields greater than 300 tesla in graphene nanobubbles. *Science*, 329(5991):544–547, 2010.

[99] Sándor Bordács, Joseph G. Checkelsky, Hiroshi Murakawa, Harold Y. Hwang, and Yoshinori Tokura. Landau level spectroscopy of dirac electrons in a polar semiconductor with giant rashba spin splitting. *Physical Review Letters*, 111:166403, Oct 2013.

[100] K. Ishizaka, M. S. Bahramy, H. Murakawa, M. Sakano, T. Shimojima, T. Sonobe, K. Koizumi, S. Shin, H. Miyahara, A. Kimura, K. Miyamoto, T. Okuda, H. Namatame, M. Taniguchi, R. Arita, N. Nagaosa, K. Kobayashi, Y. Murakami, R. Kumai, Y. Kaneko, Y. Onose, and Y. Tokura. Giant rashba-type spin splitting in bulk bitei. *Nature Materials*, 10(7):521–526, 2011.

[101] M. Sakano, M. S. Bahramy, A. Katayama, T. Shimojima, H. Murakawa, Y. Kaneko, W. Malaeb, S. Shin, K. Ono, H. Kumigashira, R. Arita, N. Nagaosa, H. Y. Hwang, Y. Tokura, and K. Ishizaka. Strongly spin-orbit coupled two-dimensional electron gas emerging near the surface of polar semiconductors. *Physical Review Letters*, 110:107204, Mar 2013.

[102] Youngkuk Kim, C. L. Kane, E. J. Mele, and Andrew M. Rappe. Layered topological crystalline insulators. *Physical Review Letters*, 115:086802, Aug 2015.

[103] Junwei Liu, Xiaofeng Qian, and Liang Fu. Crystal field effect induced topological crystalline insulators in monolayer iv–vi semiconductors. *Nano Letters*, 15(4):2657–2661, 2015.

[104] Xiuwen Zhang, Qihang Liu, Jun-Wei Luo, Arthur J Freeman, and Alex Zunger. Hidden spin polarization in inversion-symmetric bulk crystals. *Nature Physics*, 10(5):387–393, 2014.

[105] Hongki Min, J. E. Hill, N. A. Sinitsyn, B. R. Sahu, Leonard Kleinman, and A. H. MacDonald. Intrinsic and rashba spin-orbit interactions in graphene sheets. *Physical Review B*, 74:165310, Oct 2006.

[106] Hongtao Yuan, Mohammad Saeed Bahramy, Kazuhiro Morimoto, Sanfeng Wu, Kentaro Nomura, Bohm-Jung Yang, Hidekazu Shimotani, Ryuji Suzuki, Minglin Toh, Christian Kloc, Xiaodong Xu, Ryotaro Arita, Naoto Nagaosa, and Yoshihiro Iwasa. Zeeman-type spin splitting controlled by an electric field. *Nature Physics*, 9(9):563–569, 2013.

[107] A. Avsar, J. Y. Tan, T. Taychatanapat, J. Balakrishnan, G. K. W. Koon, Y. Yeo, J. Lahiri, A. Carvalho, A. S. Rodin, E. C. T. O'Farrell, G. Eda, A. H. Castro Neto,

and B. Özyilmaz. Spin-orbit proximity effect in graphene. *Nature Communications*, 5:4875–4875, 2013.

[108] Domenico Di Sante, Alessandro Stroppa, Paolo Barone, Myung-Hwan Whangbo, and Silvia Picozzi. Emergence of ferroelectricity and spin-valley properties in two-dimensional honeycomb binary compounds. *Physical Review B*, 91(16):161401, 2015.

[109] Qun-Fang Yao, Jia Cai, Wen-Yi Tong, Shi-Jing Gong, Ji-Qing Wang, Xiangang Wan, Chun-Gang Duan, and J. H. Chu. Manipulation of the large rashba spin splitting in polar two-dimensional transition-metal dichalcogenides. *Physical Review B*, 95:165401, Apr 2017.

[110] Yi Zhang, Ke He, Cui-Zu Chang, Can-Li Song, Li-Li Wang, Xi Chen, Jin-Feng Jia, Zhong Fang, Xi Dai, Wen-Yu Shan, Shun-Qing Shen, Qian Niu, Xiao-Liang Qi, Shou-Cheng Zhang, Xu-Cun Ma, and Qi-Kun Xue. Crossover of the three-dimensional topological insulator bi2se3 to the two-dimensional limit. *Nature Physics*, 6(8):584–588, 2010.

[111] Yue Cao, J. A. Waugh, X-W. Zhang, J-W. Luo, Q. Wang, T. J. Reber, S. K. Mo, Z. Xu, A. Yang, J. Schneeloch, G. D. Gu, M. Brahlek, N. Bansal, S. Oh, A. Zunger, and D. S. Dessau. Mapping the orbital wavefunction of the surface states in three-dimensional topological insulators. *Nature Physics*, 9(8):499–504, 2013.

[112] Haijun Zhang, Chao-Xing Liu, and Shou-Cheng Zhang. Spin-orbital texture in topological insulators. *Physical Review Letters*, 111(6):066801, 2013.

[113] Qihang Liu, Xiuwen Zhang, J. A. Waugh, D. S. Dessau, and Alex Zunger. Orbital mapping of energy bands and the truncated spin polarization in three-dimensional rashba semiconductors. *Physical Review B*, 94:125207, Sep 2016.

[114] Lewis Bawden, Jonathan M. Riley, Choong H. Kim, Raman Sankar, Eric J. Monkman, Daniel E. Shai, Haofei I. Wei, Edward B. Lochocki, Justin W. Wells, Worawat Meevasana, Timur K. Kim, Moritz Hoesch, Yoshiyuki Ohtsubo, Patrick Le Fèvre, Craig J. Fennie, Kyle M. Shen, Fangcheng Chou, and Phil D. C. King. Hierarchical spin-orbital polarization of a giant rashba system. *Science Advances*, 1(8):e1500495, 2015.

[115] Wenhui Wan, Yugui Yao, Liangfeng Sun, Cheng-Cheng Liu, and Fan Zhang. Topological, valleytronic, and optical properties of monolayer pbs. *Advanced Materials*, 29(10):1604788–n/a, 2017. 1604788.

[116] Kai Chang, Junwei Liu, Haicheng Lin, Na Wang, Kun Zhao, Anmin Zhang, Feng Jin, Yong Zhong, Xiaopeng Hu, Wenhui Duan, Qingming Zhang, Liang Fu, Qi-Kun Xue, Xi Chen, and Shuai-Hua Ji. Discovery of robust in-plane ferroelectricity in atomic-thick snte. *Science*, 353(6296):274–278, 2016.

[117] John P. Perdew, Kieron Burke, and Matthias Ernzerhof. Generalized gradient approximation made simple. *Physical Review Letters*, 77:3865–3868, Oct 1996.

[118] Ruixiang Fei, Wei Kang, and Li Yang. Ferroelectricity and phase transitions in monolayer group-iv monochalcogenides. *Physical Review Letters*, 117:097601, Aug 2016.

[119] Hua Wang and Xiaofeng Qian. Two-dimensional multiferroics in monolayer group iv monochalcogenides. *2D Materials*, 4(1):015042, 2017.

[120] S. P. Beckman, Xinjie Wang, Karin M. Rabe, and David Vanderbilt. Ideal barriers to polarization reversal and domain-wall motion in strained ferroelectric thin films. *Physical Review B*, 79:144124, Apr 2009.

[121] Marcus Liebmann, Christian Rinaldi, Domenico Di Sante, Jens Kellner, Christian Pauly, Rui Ning Wang, Jos Emiel Boschker, Alessandro Giussani, Stefano Bertoli, Matteo Cantoni, Lorenzo Baldrati, Marco Asa, Ivana Vobornik, Giancarlo Panaccione, Dmitry Marchenko, Jaime Sánchez-Barriga, Oliver Rader, Raffaella Calarco, Silvia Picozzi, Riccardo Bertacco, and Markus Morgenstern. Giant rashba-type spin splitting in ferroelectric gete (111). *Advanced Materials*, 28(3):560–565, 2016.

[122] Ang-Yu Lu, Hanyu Zhu, Jun Xiao, Chih-Piao Chuu, Yimo Han, Ming-Hui Chiu, Chia-Chin Cheng, Chih-Wen Yang, Kung-Hwa Wei, Yiming Yang, Yuan Wang, Dimosthenis Sokaras, Dennis Nordlund, Peidong Yang, David A. Muller, Mei-Yin Chou, Xiang Zhang, and Lain-Jong Li. Janus monolayers of transition metal dichalcogenides. *Nature Nanotechnology*, 2017.

[123] David Lloyd, Xinghui Liu, Jason W Christopher, Lauren Cantley, Anubhav Wadehra, Brian L Kim, Bennett B Goldberg, Anna K Swan, and J Scott Bunch. Band gap engineering with ultralarge biaxial strains in suspended monolayer mos2. *Nano Letters*, 16(9):5836–5841, 2016.

[124] H Hugo Pérez Garza, Eric W Kievit, Grégory F Schneider, and Urs Staufer. Controlled, reversible, and nondestructive generation of uniaxial extreme strains (¿ 10%) in graphene. *Nano Letters*, 14(7):4107–4113, 2014.

[125] Qihang Liu, Yuzheng Guo, and Arthur J. Freeman. Tunable rashba effect in two-dimensional laobis2 films: Ultrathin candidates for spin field effect transistors. *Nano Letters*, 13(11):5264–5270, 2013.

[126] Domenico Di Sante, Paolo Barone, Riccardo Bertacco, and Silvia Picozzi. Electric control of the giant rashba effect in bulk gete. *Advanced Materials*, 25(4):509–513, 2013.

[127] Andre K Geim and Irina V Grigorieva. Van der waals heterostructures. *Nature*, 499(7459):419, 2013.

[128] Mohammad Mehdi Ramin Moayed, Thomas Bielewicz, Martin Sebastian Zöllner, Carmen Herrmann, and Christian Klinke. Towards colloidal spintronics through rashba spin-orbit interaction in lead sulphide nanosheets. *Nature Communications*, 8:15721, 2017.

[129] Christian Rinaldi, Sara Varotto, Marco Asa, Jagoda Sławińska, Jun Fujii, Giovanni Vinai, Stefano Cecchi, Domenico Di Sante, Raffaella Calarco, Ivana Vobornik, Giancarlo Panaccione, Silvia Picozzi, and Riccardo Bertacco. Ferroelectric control of the spin texture in gete. *Nano Letters*, 18(5):2751–2758, 2018. PMID: 29380606.

[130] Andres Castellanos-Gomez, Rafael Roldán, Emmanuele Cappelluti, Michele Buscema, Francisco Guinea, Herre SJ van der Zant, and Gary A Steele. Local strain engineering in atomically thin mos2. *Nano Letters*, 13(11):5361–5366, 2013.

[131] Jan Raphael Bindel, Mike Pezzotta, Jascha Ulrich, Marcus Liebmann, Eugene Ya Sherman, and Markus Morgenstern. Probing variations of the rashba spin–orbit coupling at the nanometre scale. *Nature Physics*, 12(10):920, 2016.

[132] Evelyn Tang and Liang Fu. Strain-induced partially flat band, helical snake states and interface superconductivity in topological crystalline insulators. *Nature Physics*, 10(12):964, 2014.

[133] Paolo Barone, Domenico Di Sante, and Silvia Picozzi. Strain engineering of topological properties in lead-salt semiconductors. *Physica status solidi Rapid Research Letters*, 7(12):1102–1106, 2013.

[134] Katsuyoshi Kobayashi. Electronic states of snte and pbte (001) monolayers with supports. *Surface Science*, 639:54–65, 2015.

[135] Walter A Harrison. *Elementary Electronic Structure: Revised*. World Scientific Publishing Company, 2004.

[136] M. A. Cazalilla, H. Ochoa, and F. Guinea. Quantum spin hall effect in two-dimensional crystals of transition-metal dichalcogenides. *Physical Review Letters*, 113:077201, Aug 2014.

[137] Habib Rostami, Rafael Roldán, Emmanuele Cappelluti, Reza Asgari, and Francisco Guinea. Theory of strain in single-layer transition metal dichalcogenides. *Physical Review B*, 92(19):195402, 2015.

[138] Shiang Fang, Stephen Carr, Jiayu Shen, Miguel A Cazalilla, and Efthimios Kaxiras. Electronic structure theory of strained two-dimensional materials. *arXiv preprint arXiv:1709.07510*, 2017.

[139] Jin-Wu Jiang and Harold S. Park. Analytic study of strain engineering of the electronic bandgap in single-layer black phosphorus. *Physical Review B*, 91:235118, Jun 2015.

[140] E. Taghizadeh Sisakht, F. Fazileh, M. H. Zare, M. Zarenia, and F. M. Peeters. Strain-induced topological phase transition in phosphorene and in phosphorene nanoribbons. *Physical Review B*, 94:085417, Aug 2016.

[141] Zenan Qi, Alexander L. Kitt, Harold S. Park, Vitor M. Pereira, David K. Campbell, and A. H. Castro Neto. Pseudomagnetic fields in graphene nanobubbles of constrained geometry: A molecular dynamics study. *Physical Review B*, 90:125419, Sep 2014.

[142] Zenan Qi, David K. Campbell, and Harold S. Park. Atomistic simulations of tension-induced large deformation and stretchability in graphene kirigami. *Physical Review B*, 90:245437, Dec 2014.

[143] Francisco Guinea, MI Katsnelson, and AK Geim. Energy gaps and a zero-field quantum hall effect in graphene by strain engineering. *Nature Physics*, 6(1):30, 2010.

[144] Juan L. Mañes, Fernando de Juan, Mauricio Sturla, and María A. H. Vozmediano. Generalized effective hamiltonian for graphene under nonuniform strain. *Physical Review B*, 88:155405, Oct 2013.

[145] M Ramezani Masir, D Moldovan, and FM Peeters. Pseudo magnetic field in strained graphene: Revisited. *Solid State Communications*, 175:76–82, 2013.

[146] Fernando de Juan, Mauricio Sturla, and María A. H. Vozmediano. Space dependent fermi velocity in strained graphene. *Physical Review Letters*, 108:227205, May 2012.

[147] Alexander L. Kitt, Vitor M. Pereira, Anna K. Swan, and Bennett B. Goldberg. Lattice-corrected strain-induced vector potentials in graphene. *Physical Review B*, 85:115432, Mar 2012.

[148] Linn Leppert, Sebastian E Reyes-Lillo, and Jeffrey B Neaton. Electric field-and strain-induced rashba effect in hybrid halide perovskites. *The Journal of Physical Chemistry Letters*, 7(18):3683–3689, 2016.

[149] Xiaofeng Qian, Liang Fu, and Ju Li. Topological crystalline insulator nanomembrane with strain-tunable band gap. *Nano Research*, 8(3):967–979, 2015.

[150] Alessandro Stroppa, Claudio Quarti, Filippo De Angelis, and Silvia Picozzi. Ferroelectric polarization of ch3nh3pbi3: a detailed study based on density functional theory and symmetry mode analysis. *The Journal of Physical Chemistry Letters*, 6(12):2223–2231, 2015.

[151] Alessio Filippetti, Vincenzo Fiorentini, Francesco Ricci, Pietro Delugas, and Jorge Íñiguez. Prediction of a native ferroelectric metal. *Nature Communications*, 7:11211, 2016.

[152] Matthias Droth, Guido Burkard, and Vitor M. Pereira. Piezoelectricity in planar boron nitride via a geometric phase. *Physical Review B*, 94:075404, Aug 2016.

[153] Habib Rostami, Francisco Guinea, Marco Polini, and Rafael Roldán. Piezoelectricity and valley chern number in inhomogeneous hexagonal 2d crystals. *npj 2D Materials and Applications*, 2(1):15, 2018.

[154] Alexander Georgi, Peter Nemes-Incze, Ramon Carrillo-Bastos, Daiara Faria, Silvia Viola Kusminskiy, Dawei Zhai, Martin Schneider, Dinesh Subramaniam, Torge Mashoff, Nils M. Freitag, Marcus Liebmann, Marco Pratzer, Ludger Wirtz, Colin R. Woods, Roman V. Gorbachev, Yang Cao, Kostya S. Novoselov, Nancy Sandler, and Markus Morgenstern. Tuning the pseudospin polarization of graphene by a pseudomagnetic field. *Nano Letters*, 17(4):2240–2245, 2017. PMID: 28211276.

[155] Paul Z Hanakata, Zenan Qi, David K Campbell, and Harold S Park. Highly stretchable mos 2 kirigami. *Nanoscale*, 8(1):458–463, 2016.

[156] Kin Fai Mak, Changgu Lee, James Hone, Jie Shan, and Tony F Heinz. Atomically thin mos 2: a new direct-gap semiconductor. *Physical Review Letters*, 105(13):136805, 2010.

[157] S Bertolazzi, J Brivio, and A Kis. Stretching and breaking of ultrathin mos_2. *ACS Nano*, 5(12):9703–9709, 2011.

[158] Andres Castellanos-Gomez, Menno Poot, Gary A Steele, Herre SJ van der Zant, Nicolás Agraït, and Gabino Rubio-Bollinger. Elastic properties of freely suspended mos2 nanosheets. *Advanced Materials*, 24(6):772–775, 2012.

[159] J-W Jiang, Z Qi, H S Park, and T Rabczuk. Elastic bending modulus of single-layer molybdenum disulfide (mos_2): finite thickness effect. *Nanotechnology*, 24:435705, 2013.

[160] K Q Dang, J P Simpson, and D E Spearot. Phase transformation in monolayer molybdenum disulfide (mos_2) under tension predicted by molecular dynamics simulations. *Scripta Materialia*, 76:41–44, 2014.

[161] Chuan Fei Guo, Tianyi Sun, Qihan Liu, Zhigang Suo, and Zhifeng Ren. Highly stretchable and transparent nanomesh electrodes made by grain boundary lithography. *Nature Communications*, 5:3121, 2014.

[162] Terry C Shyu, Pablo F Damasceno, Paul M Dodd, Aaron Lamoureux, Lizhi Xu, Matthew Shlian, Max Shtein, Sharon C Glotzer, and Nicholas A Kotov. A kirigami approach to engineering elasticity in nanocomposites through patterned defects. *Nature Materials*, 14(8):785, 2015.

[163] Chuan Fei Guo, Qihan Liu, Guohui Wang, Yecheng Wang, Zhengzheng Shi, Zhigang Suo, Ching-Wu Chu, and Zhifeng Ren. Fatigue-free, superstretchable, transparent, and biocompatible metal electrodes. *Proceedings of the National Academy of Sciences*, 112(40):12332–12337, 2015.

[164] Lammps. *http://lammps.sandia.gov*, 2012.

[165] Steve Plimpton. Fast parallel algorithms for short-range molecular dynamics. *Journal of Computational Physics*, 117(1):1–19, 1995.

[166] Philipp Wagner, Christopher P. Ewels, Viktoria V. Ivanovskaya, Patrick R. Briddon, Amand Pateau, and Bernard Humbert. Ripple edge engineering of graphene nanoribbons. *Physics Review B*, 84:134110, Oct 2011.

[167] Shannon A Zirbel, Robert J Lang, Mark W Thomson, Deborah A Sigel, Phillip E Walkemeyer, Brian P Trease, Spencer P Magleby, and Larry L Howell. Accommodating thickness in origami-based deployable arrays. *Journal of Mechanical Design*, 135(11):111005, 2013.

[168] Ahmad Rafsanjani, Yuerou Zhang, Bangyuan Liu, Shmuel M Rubinstein, and Katia Bertoldi. Kirigami skins make a simple soft actuator crawl. *Science Robotics*, 3(15):eaar7555, 2018.

[169] Zenan Qi, David K. Campbell, and Harold S. Park. Atomistic simulations of tension-induced large deformation and stretchability in graphene kirigami. *Physical Review B*, 90:245437, Dec 2014.

[170] Alan A Griffith and M Eng. Vi. the phenomena of rupture and flow in solids. *Philosophical Transactions of the Royal Society A*, 221(582-593):163–198, 1921.

[171] H Zhao and NR Aluru. Temperature and strain-rate dependent fracture strength of graphene. *Journal of Applied Physics*, 108(6):064321, 2010.

[172] Peng Zhang, Lulu Ma, Feifei Fan, Zhi Zeng, Cheng Peng, Phillip E Loya, Zheng Liu, Yongji Gong, Jiangnan Zhang, Xingxiang Zhang, et al. Fracture toughness of graphene. *Nature Communications*, 5:3782, 2014.

[173] GangSeob Jung, Zhao Qin, and Markus J Buehler. Molecular mechanics of polycrystalline graphene with enhanced fracture toughness. *Extreme Mechanics Letters*, 2:52–59, 2015.

[174] Tawfiqur Rakib, Satyajit Mojumder, Sourav Das, Sourav Saha, and Mohammad Motalab. Graphene and its elemental analogue: A molecular dynamics view of fracture phenomenon. *Physica B: Condensed Matter*, 515:67–74, 2017.

[175] Marcelo A Dias, Michael P McCarron, Daniel Rayneau-Kirkhope, Paul Z Hanakata, David K Campbell, Harold S Park, and Douglas P Holmes. Kirigami actuators. *Soft Matter*, 13(48):9087–9092, 2017.

[176] Midori Isobe and Ko Okumura. Initial rigid response and softening transition of highly stretchable kirigami sheet materials. *Scientific Reports*, 6:24758, 2016.

[177] Ahmad Rafsanjani and Katia Bertoldi. Buckling-induced kirigami. *Physical Review Letters*, 118:084301, Feb 2017.

[178] Michael Moshe, Suraj Shankar, Mark J Bowick, and David R Nelson. Nonlinear mechanics of thin frames. *arXiv preprint arXiv:1801.08263*, 2018.

[179] Paul Masih Das, Gopinath Danda, Andrew Cupo, William M Parkin, Liangbo Liang, Neerav Kharche, Xi Ling, Shengxi Huang, Mildred S Dresselhaus, Vincent Meunier, et al. Controlled sculpture of black phosphorus nanoribbons. *ACS Nano*, 10(6):5687–5695, 2016.

[180] Ole Sigmund and Joakim Petersson. Numerical instabilities in topology optimization: a survey on procedures dealing with checkerboards, mesh-dependencies and local minima. *Structural Optimization*, 16(1):68–75, 1998.

[181] Mark J Jakiela, Colin Chapman, James Duda, Adenike Adewuya, and Kazuhiro Saitou. Continuum structural topology design with genetic algorithms. *Computer Methods in Applied Mechanics and Engineering*, 186(2-4):339–356, 2000.

[182] X Huang and YM Xie. Convergent and mesh-independent solutions for the bi-directional evolutionary structural optimization method. *Finite Elements in Analysis and Design*, 43(14):1039–1049, 2007.

[183] Grace X Gu, Leon Dimas, Zhao Qin, and Markus J Buehler. Optimization of composite fracture properties: Method, validation, and applications. *Journal of Applied Mechanics*, 83(7):071006, 2016.

[184] Atsuto Seko, Atsushi Togo, Hiroyuki Hayashi, Koji Tsuda, Laurent Chaput, and Isao Tanaka. Prediction of low-thermal-conductivity compounds with first-principles anharmonic lattice-dynamics calculations and bayesian optimization. *Physical Review Letters*, 115(20):205901, 2015.

[185] Austin D Sendek, Qian Yang, Ekin D Cubuk, Karel-Alexander N Duerloo, Yi Cui, and Evan J Reed. Holistic computational structure screening of more than 12000 candidates for solid lithium-ion conductor materials. *Energy & Environmental Science*, 10(1):306–320, 2017.

[186] Berk Onat, Ekin D Cubuk, Brad D Malone, and Efthimios Kaxiras. Implanted neural network potentials: Application to li-si alloys. *Physical Review B*, 97(9):094106, 2018.

[187] Grace X Gu, Chun-Teh Chen, and Markus J Buehler. De novo composite design based on machine learning algorithm. *Extreme Mechanics Letters*, 18:19–28, 2018.

[188] Jörg Behler and Michele Parrinello. Generalized neural-network representation of high-dimensional potential-energy surfaces. *Physical Review Letters*, 98(14):146401, 2007.

[189] Jörg Behler. Atom-centered symmetry functions for constructing high-dimensional neural network potentials. *The Journal of Chemical Physics*, 134(7):074106, 2011.

[190] Ekin D Cubuk, Brad D Malone, Berk Onat, Amos Waterland, and Efthimios Kaxiras. Representations in neural network based empirical potentials. *The Journal of Chemical Physics*, 147(2):024104, 2017.

[191] Ekin D Cubuk, Samuel S Schoenholz, Efthimios Kaxiras, and Andrea J Liu. Structural properties of defects in glassy liquids. *The Journal of Physical Chemistry B*, 120(26):6139–6146, 2016.

[192] Samuel S Schoenholz, Ekin D Cubuk, Efthimios Kaxiras, and Andrea J Liu. Relationship between local structure and relaxation in out-of-equilibrium glassy systems. *Proceedings of the National Academy of Sciences*, 114(2):263–267, 2017.

[193] ED Cubuk, RJS Ivancic, SS Schoenholz, DJ Strickland, A Basu, ZS Davidson, J Fontaine, JL Hor, Y-R Huang, Y Jiang, et al. Structure-property relationships from universal signatures of plasticity in disordered solids. *Science*, 358(6366):1033–1037, 2017.

[194] Peter Broecker, Juan Carrasquilla, Roger G Melko, and Simon Trebst. Machine learning quantum phases of matter beyond the fermion sign problem. *Scientific Reports*, 7(1):8823, 2017.

[195] Grace X. Gu, Chun-Teh Chen, Deon J. Richmond, and Markus J. Buehler. Bioinspired hierarchical composite design using machine learning: simulation, additive manufacturing, and experiment. *Materials Horizons*, 5:939–945, 2018.

[196] Steven J Stuart, Alan B Tutein, and Judith A Harrison. A reactive potential for hydrocarbons with intermolecular interactions. *The Journal of Chemical Physics*, 112(14):6472–6486, 2000.

[197] Fang Liu, Pingbing Ming, and Ju Li. Ab initio calculation of ideal strength and phonon instability of graphene under tension. *Physical Review B*, 76:064120, Aug 2007.

[198] Changgu Lee, Xiaoding Wei, Jeffrey W Kysar, and James Hone. Measurement of the elastic properties and intrinsic strength of monolayer graphene. *Science*, 321(5887):385–388, 2008.

[199] Martín Abadi, Ashish Agarwal, Paul Barham, Eugene Brevdo, Zhifeng Chen, Craig Citro, Greg S. Corrado, Andy Davis, Jeffrey Dean, Matthieu Devin, Sanjay Ghemawat, Ian Goodfellow, Andrew Harp, Geoffrey Irving, Michael Isard, Yangqing Jia, Rafal Jozefowicz, Lukasz Kaiser, Manjunath Kudlur, Josh Levenberg, Dandelion Mané, Rajat Monga, Sherry Moore, Derek Murray, Chris Olah, Mike Schuster, Jonathon Shlens, Benoit Steiner, Ilya Sutskever, Kunal Talwar, Paul Tucker, Vincent Vanhoucke, Vijay Vasudevan, Fernanda Viégas, Oriol Vinyals, Pete Warden, Martin Wattenberg, Martin Wicke, Yuan Yu, and Xiaoqiang Zheng. TensorFlow: Large-scale machine learning on heterogeneous systems, 2015. Software available from tensorflow.org.

[200] F. Pedregosa, G. Varoquaux, A. Gramfort, V. Michel, B. Thirion, O. Grisel, M. Blondel, P. Prettenhofer, R. Weiss, V. Dubourg, J. Vanderplas, A. Passos, D. Cournapeau, M. Brucher, M. Perrot, and E. Duchesnay. Scikit-learn: Machine learning in Python. *Journal of Machine Learning Research*, 12:2825–2830, 2011.

[201] Kurt Hornik, Maxwell Stinchcombe, and Halbert White. Multilayer feedforward networks are universal approximators. *Neural Networks*, 2(5):359–366, 1989.

[202] George Cybenko. Approximation by superpositions of a sigmoidal function. *Mathematics of Control, Signals and Systems*, 2(4):303–314, 1989.

[203] K. Simonyan and A. Zisserman. Very deep convolutional networks for large-scale image recognition. *CoRR*, abs/1409.1556, 2014.

[204] Nan Hu, Dajing Chen, Dong Wang, Shicheng Huang, Ian Trase, Hannah M. Grover, Xiaojiao Yu, John X. J. Zhang, and Zi Chen. Stretchable kirigami polyvinylidene difluoride thin films for energy harvesting: Design, analysis, and performance. *Physical Review Applied*, 9:021002, Feb 2018.

[205] Paul Z Hanakata, AS Rodin, Harold S Park, David K Campbell, and AH Castro Neto. Strain-induced gauge and rashba fields in ferroelectric rashba lead chalcogenide pb x monolayers (x= s, se, te). *Physical Review B*, 97(23):235312, 2018.

[206] Paul Z. Hanakata, Ekin D. Cubuk, David K. Campbell, and Harold S. Park. Accelerated search and design of stretchable graphene kirigami using machine learning. *Physical Review Letters*, 121:255304, Dec 2018.

[207] Yusuke Morikawa, Shota Yamagiwa, Hirohito Sawahata, Rika Numano, Kowa Koida, Makoto Ishida, and Takeshi Kawano. Ultrastretchable kirigami bioprobes. *Advanced Healthcare Materials*, 7(3):1701100, 2018.

[208] Yuki Yamamoto, Shingo Harada, Daisuke Yamamoto, Wataru Honda, Takayuki Arie, Seiji Akita, and Kuniharu Takei. Printed multifunctional flexible device with an integrated motion sensor for health care monitoring. *Science Advances*, 2(11):e1601473, 2016.

[209] Xin Ning, Xueju Wang, Yi Zhang, Xinge Yu, Dongwhi Choi, Ning Zheng, Dong Sung Kim, Yonggang Huang, Yihui Zhang, and John A Rogers. Assembly of advanced materials into 3d functional structures by methods inspired by origami and kirigami: A review. *Advanced Materials Interfaces*, 5(13):1800284, 2018.

[210] Luca M. Ghiringhelli, Jan Vybiral, Sergey V. Levchenko, Claudia Draxl, and Matthias Scheffler. Big data of materials science: Critical role of the descriptor. *Physical Review Letters*, 114:105503, Mar 2015.

[211] Ghanshyam Pilania, Chenchen Wang, Xun Jiang, Sanguthevar Rajasekaran, and Ramamurthy Ramprasad. Accelerating materials property predictions using machine learning. *Scientific Reports*, 3:2810, 2013.

[212] Rafael Gómez-Bombarelli, Jorge Aguilera-Iparraguirre, Timothy D Hirzel, David Duvenaud, Dougal Maclaurin, Martin A Blood-Forsythe, Hyun Sik Chae, Markus Einzinger, Dong-Gwang Ha, Tony Wu, et al. Design of efficient molecular organic

light-emitting diodes by a high-throughput virtual screening and experimental approach. *Nature Materials*, 15(10):1120, 2016.

[213] Matti Hellström and Jörg Behler. Neural network potentials in materials modeling. *Handbook of Materials Modeling: Methods: Theory and Modeling*, pages 1–20, 2018.

[214] Jörg Behler. Perspective: Machine learning potentials for atomistic simulations. *The Journal of Chemical Physics*, 145(17):170901, 2016.

Curriculum Vitae

Contact Paul Hanakata

Department of Physics, Boston University, 590 Commonwealth Avenue, Boston, MA 02215

Education **Boston University** PhD in Physics, September 2014 – May 2019. Thesis advisor: David K. Campbell.

Wesleyan University, B.A., Physics and Mathematics (With High Honor – Summa Cum Laude), September 2010 – May 2014. Thesis advisor: Francis W. Starr.

Publications

1. **Paul Z. Hanakata**, Ekin D. Cubuk, David K. Campbell, and Harold S. Park, *Accelerated search and design of stretchable graphene kirigami using machine learning.* Physical Review Letters. **121**, 255304 (2018)
2. **Paul Z. Hanakata**, A. S. Rodin, Harold S. Park, David K. Campbell, and A. H. Castro Neto, *Strain-induced gauge and Rashba fields in ferroelectric Rashba lead chalcogenide PbX monolayers (X=S, Se, Te).* Physical Review B. **97**, 235312 (2018)
3. **Paul Z. Hanakata**, A. S. Rodin, Alexandra Carvalho, Harold S. Park, David K. Campbell, and A. H. Castro Neto, *Two-dimensional square buckled Rashba lead chalcogenides.* Physical Review B Rapid Communications. **96** 161401 (2017)
4. A. S Rodin, **Paul Z. Hanakata**, Alexandra Carvalho, Harold S. Park, David K. Campbell, and A. H. Castro Neto, *Rashba-like dispersion in buckled square lattices.* Physical Review B. **96** 115450 (2017)
5. Marcelo A Dias, Michael P McCarron, Daniel Rayneau-Kirkhope, **Paul Z. Hanakata**, David Campbell, Harold Park, Douglas P Holmes, *Kirigami Actuators.* Soft Matter.**13** 9087 (2017)
6. **Paul Z. Hanakata**, Alexandra Carvalho, David K. Campbell, and Harold S. Park, *Polarization and valley switching in monolayer group-IV monochalcogenides.* Physical Review B. **94** 035304 (2016)
7. **Paul Z. Hanakata**, Zenan Qi, David K. Campbell, and Harold S. Park, *Highly Stretchable MoS_2 Kirigami.* Nanoscale. **8** 458 (2016)
8. Beatriz A. Betancourt, **Paul Z. Hanakata**, Francis W. Starr, Jack F. Douglas, *Quantitative relations between cooperative motion, emergent elasticity, and free volume in model glass-forming polymer materials.* Proceedings of the National Academy of Sciences. **112** 2966 (2015)

9. **Paul Z. Hanakata**, Beatriz A. Betancourt, Jack F. Douglas, Francis W Starr, *A unifying framework to quantify the effects of substrate interactions, stiffness, and roughness on the dynamics of thin supported polymer films.* The Journal of Chemical Physics. **142** 234907 (2015)

10. **Paul Z. Hanakata**, Jack F. Douglas, Francis W Starr, *Interfacial mobility scale determines the scale of collective motion and relaxation rate in polymer films.* Nature communications. **5** 4163 (2014)

11. **Paul Z. Hanakata**, Jack F. Douglas, Francis W Starr, *Local variation of fragility and glass transition temperature of ultra-thin supported polymer films.* The Journal of Chemical Physics. **137** 244901 (2012)